



## Mesoscale and microscale downscaling for the Wind Atlas of Mexico (WAM) project

Olsen, Bjarke Tobias; Hahmann, Andrea N.; Floors, Rogier R.; Cavar, Dalibor; Peña, Alfredo; Villanueva, Héctor; Davis, Neil N.; Hansen, Jens C.

*Publication date:*  
2021

*Document Version*  
Publisher's PDF, also known as Version of record

[Link back to DTU Orbit](#)

*Citation (APA):*  
Olsen, B. T., Hahmann, A. N., Floors, R. R., Cavar, D., Peña, A., Villanueva, H., Davis, N. N., & Hansen, J. C. (2021). *Mesoscale and microscale downscaling for the Wind Atlas of Mexico (WAM) project*. DTU Wind Energy. DTU Wind Energy E No. E-0223

---

### General rights

Copyright and moral rights for the publications made accessible in the public portal are retained by the authors and/or other copyright owners and it is a condition of accessing publications that users recognise and abide by the legal requirements associated with these rights.

- Users may download and print one copy of any publication from the public portal for the purpose of private study or research.
- You may not further distribute the material or use it for any profit-making activity or commercial gain
- You may freely distribute the URL identifying the publication in the public portal

If you believe that this document breaches copyright please contact us providing details, and we will remove access to the work immediately and investigate your claim.

# Mesoscale and microscale downscaling for the Wind Atlas of Mexico (WAM) project



## Department of Wind Energy E Report 2021

Bjarke T. Olsen, Andrea N. Hahmann, Rogier R.  
Floors, Dalibor Cavar, Alfredo Peña, Héctor Villanueva,  
Neil N. Davis and Jens C. Hansen

DTU Wind Energy E-0223

August 2021

**DTU Wind Energy**  
Department of Wind Energy

---



**Authors:** Bjarke T. Olsen, Andrea N. Hahmann, Rogier R. Floors, Dalibor Cavar, Alfredo Peña, Héctor Villanueva, Neil N. Davis and Jens C. Hansen  
**Title:** Mesoscale and microscale downscaling for the Wind Atlas of Mexico (WAM) project

**Summary (max 2000 characters):**

This document reports on the production of the Wind Atlas of Mexico (WAM), including the methods used to create the mesoscale component based on the Weather Research and Forecasting (WRF) model, and the microscale component based on downscaling of WRF using the Wind Atlas Analysis and Applications Program (WAsP). The report is divided into four main parts. In the first part, we document the method used to run the mesoscale simulations and to select the best suited WRF model configuration. The best model configuration is found by evaluation against the measurements from the WAM masts using various metrics. In the second part, we describe the method used to generalize and downscale the WRF model wind climate using PyWAsP, a python interface to run WAsP. We compare the results from the downscaled numerical wind atlas against the observed wind statistics from seven WAM masts in the third part to find the optimal configuration. In the last part we present the new wind resource maps for all of Mexico and their long-term climatology. In WAM, there have been many updates to the configuration DTU normally uses to perform wind atlases and that has been documented in Hahmann et al. (2018). Among the most important:

1. We ran simulations for an equivalent of ten years covering the period most observed in all the WAM sites to find the WRF model configuration most suited to the simulation of the wind climatology over Mexico.
2. We used a new method of generalization and downscaling of the WRF-derived wind climate that uses the PyWAsP engine and was demonstrated more accurate than the previous approaches.
3. We produced a high resolution (up to date) wind climatology for Mexico using the latest WRF Version 4.2.1, covering 10 years (2011{2020) of simulation for all Mexico at 3 km x 3 km spatial resolution and one hour time output.

The final error statistics of the WAM wind atlas show that the WRF+PyWAsP method has a MAPE of 11.7% and 5.6% for the long-term power density and wind speed, respectively. When ignoring the mast in more complex terrain, M7, the WRF and WRF+PyWAsP downscaling significantly narrows the error distributions for both long-term wind speed and power density

*Wind Atlas for Mexico (WAM) Mesoscale and microscale downscaling*

Copyright © 2021 All rights reserved. No part of this publication may be reproduced, stored in a retrieval system, or transmitted in any form or by any means, without the express written permission of the copyright owners.

This report was prepared as part of the Wind Atlas for Mexico project. The accuracy of the data and information included in this publication is not guaranteed and responsibility whatsoever and liability for any consequence or loss in connection with of application and use is not accepted. The boundaries, colors, denominations, and other information shown on any map in this report do not imply on the part of the project any judgment on the legal status of any territory or the endorsement of acceptance of such boundaries.

The text of this publication may be reproduced in whole or in part and in any form for educational or non-profit uses without special permission, provided acknowledgement of the source is made.

**DTU Wind Energy E-0223**  
**August August 2021**

**ISBN no.:**  
978-87-93549-91-3

**Project no.:**  
44071-4606 Wind Atlas Mexico

**Sponsorship:**  
Bilateral agreement on Climate  
Change Mitigation and Energy

**Pages:** 77  
**Tables:** 7  
**References:** 40

**Technical University of Denmark**  
Department of Wind Energy  
Frederiksborgvej 399  
Building 118  
4000 Roskilde  
Denmark  
Telephone

[www.vindenergi.dtu.dk](http://www.vindenergi.dtu.dk)



---

## Mesoscale and Microscale Downscaling for the Wind Atlas of Mexico (WAM) Project

Bjarke T. Olsen<sup>1</sup>, Andrea N. Hahmann<sup>1</sup>, Rogier R. Floors<sup>1</sup>,  
Dalibor Cavar<sup>1</sup>, Alfredo Peña<sup>1</sup>, Héctor Villanueva<sup>1</sup>,  
Neil N. Davis<sup>1</sup> and Jens C. Hansen<sup>1</sup>

<sup>1</sup>Department of Wind Energy, Technical University of Denmark (DTU),  
Roskilde, Denmark

*Mesoscale and Microscale Downscaling for the Wind Atlas of Mexico (WAM) Project.* Copyright © 2021

All rights reserved. No part of this publication may be reproduced, stored in a retrieval system, or transmitted in any form or by any means, without the express written permission of the copyright owners.

This report was prepared as part of the Wind Atlas for Mexico project. The accuracy of the data and information included in this publication is not guaranteed and responsibility whatsoever and liability for any consequence or loss in connection with of application and use is not accepted. The boundaries, colors, denominations, and other information shown on any map in this report do not imply on the part of the project any judgment on the legal status of any territory or the endorsement of acceptance of such boundaries. The text of this publication may be reproduced in whole or in part and in any form for educational or non-profit uses without special permission, provided acknowledgment of the source is made.

August 16, 2021

---

## Abstract

This document reports on the production of the Wind Atlas of Mexico (WAM), including the methods used to create the mesoscale component based on the Weather Research and Forecasting (WRF) model, and the microscale component based on downscaling of WRF using the Wind Atlas Analysis and Applications Program (WAsP).

The report is divided into four main parts. In the first part, we document the method used to run the mesoscale simulations and to select the best suited WRF model configuration. The best model configuration is found by evaluation against the measurements from the WAM masts using various metrics. In the second part, we describe the method used to generalize and downscale the WRF model wind climate using PyWAsP, a python interface to run WAsP. We compare the results from the downscaled numerical wind atlas against the observed wind statistics from seven WAM masts in the third part to find the optimal configuration. In the last part we present the new wind resource maps for all of Mexico and their long-term climatology.

In WAM, there have been many updates to the configuration DTU normally uses to perform wind atlases and that has been documented in [Hahmann et al. \(2018\)](#). Among the most important:

1. We ran simulations for an equivalent of ten years covering the period most observed in all the WAM sites to find the WRF model configuration most suited to the simulation of the wind climatology over Mexico.
2. We used a new method of generalization and downscaling of the WRF-derived wind climate that uses the PyWAsP engine and was demonstrated more accurate than the previous approaches.
3. We produced a high resolution (up to date) wind climatology for Mexico using the latest WRF Version 4.2.1, covering 10 years (2011–2020) of simulation for all Mexico at 3 km  $\times$  3 km spatial resolution and one hour time output.

The final error statistics of the WAM wind atlas show that the WRF+PyWAsP method has a MAPE of 11.7% and 5.6% for the long-term power density and wind speed, respectively. When ignoring the mast in more complex terrain, M7, the WRF and WRF+PyWAsP downscaling significantly narrows the error distributions for both long-term wind speed and power density.

# Contents

<b>List of Figures</b>	<b>2</b>
<b>List of Tables</b>	<b>4</b>
<b>1 Introduction</b>	<b>6</b>
1.1 Definitions and outline . . . . .	6
1.2 Glossary . . . . .	6
<b>2 Methods</b>	<b>8</b>
2.1 Model validation metrics . . . . .	8
2.2 WRF model simulations . . . . .	10
2.3 Data processing . . . . .	10
<b>3 Mesoscale modeling</b>	<b>11</b>
3.1 Sensitivity experiments . . . . .	11
3.2 WRF ensemble evaluation . . . . .	14
3.3 The production run . . . . .	19
<b>4 Microscale modeling</b>	<b>22</b>
4.1 Generalisation . . . . .	22
4.2 Downscaling . . . . .	23
4.3 Procedure for microscale validation steps . . . . .	23
4.4 Production of the microscale wind atlas . . . . .	24
<b>5 Wind atlas validation</b>	<b>25</b>
5.1 Evaluation with downscaling . . . . .	25
5.2 Validation at all sites . . . . .	26
5.3 Validation at each site . . . . .	29
5.3.1 La Rumorosa (M1) . . . . .	30
5.3.2 Mérida (M2) . . . . .	34
5.3.3 Ciudad Cuauhtémoc (M3) . . . . .	38
5.3.4 Certe (M4) . . . . .	42
5.3.5 Ojuelos (M5) . . . . .	46
5.3.6 San Fernando (M6) . . . . .	50
5.3.7 Tepexi (M7) . . . . .	54

---

<b>6</b>	<b>Wind resource maps</b>	<b>58</b>
6.1	WAM resource maps . . . . .	58
6.2	Wind resources maps around M1 . . . . .	60
<b>7</b>	<b>Summary and conclusions</b>	<b>62</b>
<b>8</b>	<b>Acknowledgments</b>	<b>64</b>
	<b>Bibliography</b>	<b>65</b>
<b>A</b>	<b>WRF namelists</b>	<b>69</b>
A.1	WPS namelist . . . . .	69
A.2	WRF namelist . . . . .	70
<b>B</b>	<b>Google Earth images at each site</b>	<b>74</b>
<b>C</b>	<b>Lookup tables for roughness length</b>	<b>76</b>

# List of Figures

3.1	Summary statistics first set of sensitivity simulations . . . . .	12
3.2	WRF model projections . . . . .	13
3.3	Description of the sensitivity simulations. . . . .	14
3.4	Evaluation metrics: BIAS . . . . .	15
3.5	Evaluation metrics: EMD . . . . .	16
3.6	Evaluation metrics: CORR . . . . .	16
3.7	Evaluation metrics: RMSE . . . . .	17
3.8	Evaluation metrics: CEMD . . . . .	17
3.9	Model statistics for the one-year simulations. . . . .	18
3.10	WRF model grid configuration . . . . .	19
3.11	Terrain elevation of the WRF D2 (3 km × 3 km) domain. . . . .	20
3.12	Dominant land use classification of the WRF D2 (3 km × 3 km) domain. . . . .	20
5.1	MAPE in the long-term wind speed at 80 m AGL for all sites. . . . .	27
5.2	Distribution of the bias in wind speed and power density . . . . .	28
5.3	Distribution of the bias in wind speed and power density at low complexity sites . . . . .	28
5.4	Location of all the validation sites. . . . .	29
5.5	Surface elevation maps at M1 . . . . .	30
5.6	ESA-CCI land use at M1 . . . . .	30
5.7	LCC land use at M1 . . . . .	31
5.8	Surface roughness length maps at M1 . . . . .	32
5.9	Observed and simulated wind climatologies at M1. . . . .	33
5.10	Observed and simulated frequency distribution at M1 . . . . .	33
5.11	Observed and WRF-simulated seasonal and diurnal cycle of wind speed at M1 . . . . .	33
5.12	Surface elevation maps at M2 . . . . .	34
5.13	ESA-CCI land use at M2 . . . . .	34
5.14	LCC land use M2 . . . . .	35
5.15	Roughness maps around mast M2 . . . . .	36
5.16	Observed and simulated wind climatologies at M2. . . . .	37
5.17	Observed and WRF-simulated frequency distribution at M2 . . . . .	37
5.18	Observed and WRF-simulated seasonal and diurnal cycle of wind speed at M2 . . . . .	37
5.19	Surface elevation maps at M3 . . . . .	38
5.20	ESA-CCI land use M3 . . . . .	38
5.21	LCC land use M3 . . . . .	39
5.22	Roughness maps around mast M3 . . . . .	40
5.23	Observed and simulated wind climatologies at M3. . . . .	41



5.24	Observed and WRF-simulated frequency distribution at M3 . . . . .	41
5.25	Observed and WRF-simulated seasonal and diurnal cycle of wind speed at M3 . . . . .	41
5.26	Surface elevation maps at M4 . . . . .	42
5.27	ESA-CCI land use M4 . . . . .	42
5.28	LCC land use M4 . . . . .	43
5.29	Roughness maps around mast M4 . . . . .	44
5.30	Observed and simulated wind climatologies at M4. . . . .	45
5.31	Observed and WRF-simulated frequency distribution at M4 . . . . .	45
5.32	Observed and WRF-simulated seasonal and diurnal cycle of wind speed at M4 . . . . .	45
5.33	Surface elevation maps at M5 . . . . .	46
5.34	ESA-CCI land use M5 . . . . .	46
5.35	LCC land use M5 . . . . .	47
5.36	Roughness maps around mast M5 . . . . .	48
5.37	Observed and simulated wind climatologies at M5. . . . .	49
5.38	Observed and WRF-simulated frequency distribution at M5 . . . . .	49
5.39	Observed and WRF-simulated seasonal and diurnal cycle of wind speed at M5 . . . . .	49
5.40	Surface elevation maps at M6 . . . . .	50
5.41	ESA-CCI land use M6 . . . . .	50
5.42	LCC land use M6 . . . . .	51
5.43	Roughness maps around mast M6 . . . . .	52
5.44	Observed and simulated wind climatologies at M6. . . . .	53
5.45	Observed and WRF-simulated frequency distribution at M6 . . . . .	53
5.46	Observed and WRF-simulated seasonal and diurnal cycle of wind speed at M6 . . . . .	53
5.47	Surface elevation maps at M7 . . . . .	54
5.48	ESA-CCI land use M7 . . . . .	54
5.49	LCC land use M7 . . . . .	55
5.50	Roughness maps around mast M7 . . . . .	56
5.51	Observed and simulated wind climatologies at M7 . . . . .	57
5.52	Observed and WRF-simulated frequency distribution at M7 . . . . .	57
5.53	Observed and WRF-simulated seasonal and diurnal cycle of wind speed at M7 . . . . .	57
6.1	Long-term mean wind speed at 100 m AGL derived from ERA5, WRF, and PyWAsP. . . . .	59
6.2	Long-term mean wind speed at 100 m AGL derived from (a) ERA5, (b) WRF model production run, and (c) PyWAsP. . . . .	59
6.3	ERA5, WRF, and WAsP-estimated emergent wind speed at 100 m AGL around M1 . . . . .	60
6.4	ERA5, WRF, and WAsP-estimated emergent wind power density at 100 m AGL around M1 . . . . .	61
B.1	GE maps for M1–M4 . . . . .	74
B.2	GE maps for M5–M7 . . . . .	75

# List of Tables

3.1	Overview of the first set of ensemble simulations . . . . .	12
3.2	WRF model setup . . . . .	21
4.1	Overview of the different microscale configurations that were evaluated. . . . .	23
5.1	The MAPE in power density ( $P$ ) and wind speed ( $U$ ) at all masts. . . . .	26
5.2	Comparison of the mean wind speed at 80 m AGL for all WAM masts for the observations ( $U_o$ ) . . . . .	27
C.1	Surface roughness length as a function of land use class for the standard WRF (minimum and maximum) and the modified for the WAM WRF model simulations. . . . .	76
C.2	The roughness length that was assigned to each land cover class from the Globcover/ESA-CCI land cover database. . . . .	77

# Chapter 1

## Introduction

### 1.1 Definitions and outline

The regional wind climate, i.e. the long-term spatial and temporal distribution of the wind speed and direction over an area of the earth surface, is vital information for locating optimal areas for the siting of wind power plants and for developing regional action plans for reduction of the use of fossil fuels for the generation of electricity. The output from long-term simulations using a mesoscale model is now widely used to generate the wind climatology necessary for calculating the wind energy resources of a given geographical area (Tammelin et al., 2012; Nawri et al., 2014; Hahmann et al., 2015; Dörenkämper et al., 2020; Hahmann et al., 2021). These wind climatologies are the most useful when validated against measurements and serve as input to microscale models for further downscaling (Badger et al., 2014; Dörenkämper et al., 2020). With this in mind, the main objectives of this report are, first, to document the methods used to derive the wind climatologies, second, to document the methods used to derive the wind resources, and, third, to validate the model results against observations.

Mesoscale model simulations using the Weather Research and Forecasting (WRF; Skamarock et al., 2008) model are verified against measurements from the seven masts in WAM. The verification is carried out for the raw WRF wind climatology (Chapter 3) and the down-scaled WRF winds (Chapter 5) using the method described in Chapter 2.

In Chapter 6 we present the maps of mesoscale simulated winds and power densities, and the final full (mesoscale and microscale) downscaled mean wind and power density maps. Finally, in Chapter 7, we summarize the results and offer factors that contribute to the uncertainty of the results.

### 1.2 Glossary

AGL Above ground level

CEMD Circular EMD (validation metric)

CFD Computational fluid dynamics

DEM Digital elevation model

DTU Technical University of Denmark

ECMWF European Centre for Medium Range Forecasting

- ERA5 Fifth generation ECMWF atmospheric reanalysis
- EMD Earth's movers distance (validation metric)
- ESA-CCI European Space Agency Climate Change Initiative
- LINCOM linearised and spectral wind flow model for use over hilly terrain
  - LSM Land surface model (WRF parameterization)
- MAE Mean absolute error (validation metric)
- MAPE Mean absolute percentage error (validation metric)
- MYNN Mellor-Yamada-Nakanishi-Niino PBL scheme (WRF parameterization)
  - M-O Monin-Obukhov SL scheme (WRF parameterization)
- NASA National Aeronautics and Space Administration (USA)
- NEWA New European Wind Atlas
- OSTIA Operational Sea Surface Temperature and Sea Ice Analysis
  - PBL Planetary boundary layer
- PyWAsP Python version of the WAsP software
  - RMSE Root mean square error (validation metric)
  - RIX Ruggedness index
    - SL Surface Layer model (WRF parameterization)
- SRTM Shuttle Radar Topography Mission
- USGS United States Geological Survey (vegetation classification)
- WASA Wind Atlas for South Africa
- WAsP Wind Atlas Analysis and Application Program
- WGS84 World Geodetic System 1984
  - WRF Weather Research and Forecasting model
  - YSU Yonsei University (YSU) PBL scheme (WRF parameterization)

# Chapter 2

## Methods

### 2.1 Model validation metrics

We used several metrics to evaluate the accuracy of the model simulations when compared to tall mast observations. These metrics were used to find the best suited model configuration used for the production simulation and the generalisation of the WRF model results.

We calculate the temporal mean (indicated by the overbar) of each modelled distribution,  $\bar{x}_m$ , and the observed distribution,  $\bar{x}_o$ , for identical time periods. The bias herein is defined as difference between the two means,  $\bar{x}_m - \bar{x}_o$ . In the case of a wind atlas,  $x$  can represent wind speed,  $u$  (temporally averaged normally over 10-min periods), or wind power density,  $P$ , defined as

$$P = \frac{1}{2} \rho \overline{u^3}, \quad (2.1)$$

where  $\rho$  is the air density. If the bias of a variable is positive, the model overestimates its value compared to observations.

The bias is a popular error statistic for comparing the wind speed distributions between observations and model-simulated fields. However, since the power density is a function of the cube of the wind speed (see Eq. 2.1) the shape of the wind speed distribution is even more important. Small changes in the wind speed distribution are amplified when converted to power. Accordingly, we use the Earth Mover's Distance (EMD) to evaluate the differences in the shape of two frequency distributions. This metric was used for the sensitivity experiments for the New European Wind Atlas (Hahmann et al., 2020). The EMD, also known as the first Wasserstein distance, is popular in image processing (EMD; Rubner et al., 2000). The EMD can be interpreted as the amount of physical work needed to move a pile of soil in the shape of one distribution to that of another distribution. For one-dimensional distributions, the EMD is equivalent to the area between two cumulative distribution functions, and, this interpretation with slight modifications, can be applied also to circular variables (Rabin et al., 2008). More discussion about the EMD properties can be found in Lupu et al. (2017). The EMD was calculated using the Pyemd package (Pele and Werman, 2008). The circular EMD (CEMD; Rabin et al., 2008) extends the EMD concept to one-dimensional circular histograms, such as the frequency distribution of wind directions. An example of how to interpret the CEMD is available in the NEWA paper (Hahmann et al., 2020).

The information about temporal co-variability is provided herein by the Pearson's correlation coefficient,  $r$ , a measure of dependence between a simulated and an observed time series,

and the root mean square error (RMSE), which estimates of systematic biases in model skill (von Storch and Zwiers, 1999). These measures are defined as

$$r = \frac{1}{\sigma_o \sigma_m} \sum_{i=1}^N (U_o^i - \bar{U}_o)(U_m^i - \bar{U}_m), \quad (2.2)$$

$$\text{where} \quad (2.3)$$

$$\sigma_o = \frac{1}{N} \sqrt{\sum_{i=1}^N (U_o^i - \bar{U}_o)^2} \text{ and } \sigma_m = \frac{1}{N} \sqrt{\sum_{i=1}^N (U_m^i - \bar{U}_m)^2}, \quad (2.4)$$

$$\text{RMSE} = \sqrt{\frac{1}{N} \sum_{i=1}^N (U_m^i - U_o^i)^2}, \quad (2.5)$$

with  $U_o^i$  and  $U_m^i$  being the  $i$ -th observed and modelled values in the time series of length  $N$ .  $\sigma_o$  and  $\sigma_m$  are the standard deviations of the observed and simulated time series.

In the selection of the optimal configuration for the WAM wind atlas, we compared the results of an ensemble of WRF model setups against the observations at all sites. One of the ensemble members was designated to be the baseline or “BASE”. To evaluate if a certain model set up from the pool performs better or worse than the BASE configuration, we define a general skill score (von Storch and Zwiers, 1999):

$$\text{SS} = 1 - M_j/M_B, \quad (2.6)$$

where  $M_j$  is the value of the metric for the  $j$ -th ensemble member and  $M_B$  is that of the baseline. The metric  $M$  can be the absolute value of the bias, the RMSE,  $r$ , EMD, or CEMD. For the correlation, the formula is reversed:  $\text{SS} = r_j/r_B - 1$ , since a perfect correlation equals 1. If  $\text{SS} > 0$  the ensemble member  $j$  “improves” the metric with respect to the baseline case; if  $\text{SS} < 0$  it “worsens” it. A value of  $\text{SS} = 1$  means that the new simulation is perfect. The SS is easily understood and is applicable to all our evaluation metrics. However, when the BASE simulation evaluates extremely well against observations (e.g. when the bias is close to zero), the skill score can become very large. Therefore, the SS is a useful quantity for the RMSE, which is rarely close to zero, but can be misleading when used for the absolute bias or the EMD, indicating large improvements when the differences in metrics themselves are small. Accordingly, we suggest using both SS and the original metric when interpreting the results.

To facilitate the comparisons at all masts, we average the BIAS or EMD. For the BIAS, we use the mean absolute error, MAE, defined as

$$\text{MAE} = \frac{1}{M} \sum_{k=1}^M |\bar{x}_m^k - \bar{x}_o^k|, \quad (2.7)$$

with  $\bar{x}_m^k$  and  $\bar{x}_o^k$  being the mean of the variable at the  $k$ -th station; and  $M$  is the number of sites. Finally, we can also define a mean absolute percentage error (MAPE) by dividing by  $\bar{x}_o^k$ ,

$$\text{MAPE} = \frac{100}{M} \sum_{k=1}^M \frac{|\bar{x}_m^k - \bar{x}_o^k|}{\bar{x}_o^k}, \quad (2.8)$$

where  $x$  = wind speed,  $U$ , or wind power density,  $P$ .

## 2.2 WRF model simulations

The WRF model simulations follow the method used in previous wind atlases: WASA2 (Hahmann et al., 2018) and WASA3 (Hahmann et al., 2021). The database of simulated winds and wind-energy relevant parameters for the model simulations was created by splitting the simulation period into a series of relatively short WRF model runs that, after concatenation, cover the desired time period. The simulations overlap in time during the spin-up period by 24 h, which is discarded, as described in Hahmann et al. (2015). In this approach, the use of nudging prevents the model solution from drifting from the observed large-scale atmospheric patterns, and the multi-days simulation ensures that the mesoscale flow is fully in equilibrium with the mesoscale characteristics of the terrain (Vincent and Hahmann, 2015). The method has the added advantage that the simulations are independent of each other, and therefore, can be computed in parallel, reducing the total time needed to complete a multi-year climatology. For WAM, we used eight-day simulations with an overlapping period of 24 hours.

The WRF model domain and configuration used in the sensitivity studies and the production run will be presented in sections 3.1 and 3.3, respectively.

## 2.3 Data processing

Wind speeds and directions are derived from the WRF model output, which represents nearly instantaneous values. For evaluating the model wind speed climatology, the zonal and meridional wind components on their original staggered Arakawa-C grid were interpolated to the coordinates of the mass grid. The interpolated wind components were then used to compute the wind speed and rotated to the true north to derive the wind direction. For a given height, e.g., 100 m, wind speeds are interpolated between neighboring model levels using linear interpolation in logarithmic height. It was found that this interpolation procedure preserves more of the original features in the model wind profile compared to other schemes (e.g., linear or polynomial interpolation of the wind components).

# Chapter 3

## Mesoscale modeling

### 3.1 Sensitivity experiments

As discussed in [Hahmann et al. \(2020\)](#), mesoscale models are, in general, not specifically developed for wind energy applications; however, over the last decade they have been extensively used for that purpose. Developing an optimal WRF model configuration for wind resource assessment is not a straightforward task, considering the large number of degrees of freedom in the model configuration, and the different choices of input data. Among the configuration options offered in the WRF model are, physical parameterisations such as planetary boundary layer (PBL), surface layer (SL), land surface model (LSM), cloud micro-physics, and radiation. Also numerical and technical options (e.g., domain layout, nudging options, time step), and the initial and boundary conditions of the atmosphere, sea surface, and land surface are relevant aspects to be explored before determining the set up that better fits a specific application. Arguably, an optimal configuration that performs best at all time and spatial scales cannot be expected, and we search herein for a configuration that tends to perform better at most instances within the ensemble of sensitivity experiments performed.

It is impossible to test every combination of the WRF model setup and possible parameterisations, as the number of such experiments would be in the thousands, which is unfeasible in terms of computational resources. Therefore, a compromise between available computational power and scientific soundness had to be found. The approach in WAM was to first define a “best practice” setup from the WASA3 production run ([Hahmann et al., 2021](#)), and then to test the sensitivity of the results to changes in the model configuration that were not tested in previous wind atlas projects.

The first set of sensitivity simulations for WAM covered one full year (2018) and used similar modelling strategy. What is varied in each sensitivity experiment is detailed in Table 3.1: PBL scheme (MYNN level 2.5 [Nakanishi and Niino \(2009\)](#), YSU [Hong et al. \(2006\)](#)), surface layer scheme (MYNN [Nakanishi and Niino \(2009\)](#), MM5 [Jiménez et al. \(2012\)](#) and M-O [Janjic and Zavisla \(1994\)](#)). We also varied the horizontal grid spacing (3.33 km versus 5 km) and the height of the vertical levels close to the ground.

The statistics for these simulations against mast values are presented in Fig. 3.1. For most metrics the differences among stations are larger than differences between models in a single station, expressed in this figure as consistent colours for each line. Three sites report considerably large biases: M3, M4 and M7. Biases at M7 are the largest, with  $3.1 \text{ m s}^{-1}$  or 57 % in the YSU-MM5 simulation. At other sites the biases are between  $-0.5$  and  $0.4 \text{ m s}^{-1}$ .



**Table 3.1** – Overview of the ensemble of simulations varying planetary boundary layer (PBL), surface layer (SL), horizontal grid spacing and height of the model levels. Standard levels: 0, 11.3, 32.3, 48.5, 64.7, 80.9, 100.5, 125.8 m; higher first level: 0., 19.4, 40.3, 56.5, 72.7, 89.0, 108.5, 133.8 m

run name	WRF version	PBL (#)	SL (#)	resolution (km)	vertical levels
MYNN-MO	V3.8.1	MYNN (5)	M-O (2)	30/10/3.33	standard
MYNN-MO-UP	V3.8.1	MYNN (5)	M-O (2)	30/10/3.33	higher first level
MYNN-MO-5KM	V3.8.1	MYNN (5)	MYNN	45/15/5	standard
MYNN-MO	V3.8.1	MYNN (5)	MYNN (5)	30/10/3.33	standard
YSU-MM5-UP	V3.8.1	YSU (1)	MM5 (1)	30/10/3.33	higher first level

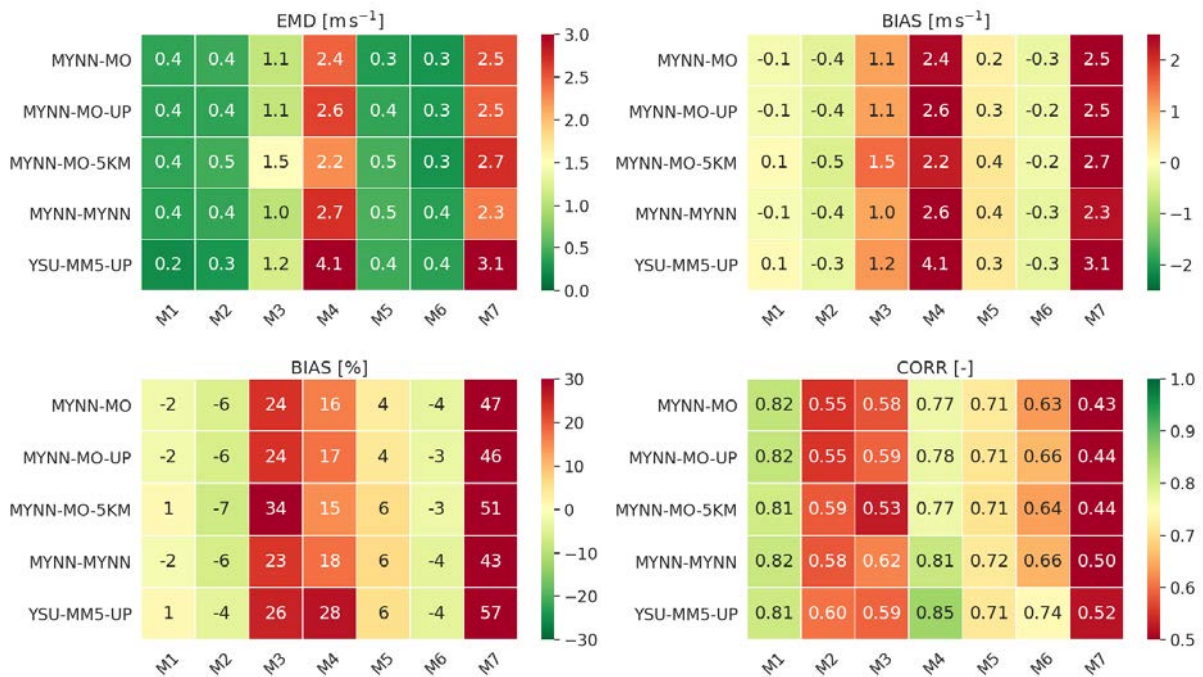


**Figure 3.1** – Summary statistics of the first set of sensitivity simulations presented in Table 3.1 for the wind speed at 80 m.

The effect of resolution is not particularly strong, with small increases in the biases at M3 and M7, but decreases at M4 when decreasing the horizontal resolution from 3.33 to 5 km. With these results in mind, the main objective of subsequent simulations was to improve the simulations at these two sites, hopefully without degrading the results at other sites.

The second set of sensitivity tests for WAM covered a six-week period from 1 January to 11 February 2018, which corresponds to a particularly windy period in Mexico. The description of the simulations is presented in Fig. 3.3. All simulations use the WRF model version 4.2.1. The various changes involve:

- The WRF model grid projection: Mercator or Lambert (Fig. 3.2)
- The WRF model grid configuration: 27/9/3 km, 10/3.33 km or 9/3 km
- The model physical parameterizations; NEWA represents the configuration used in the

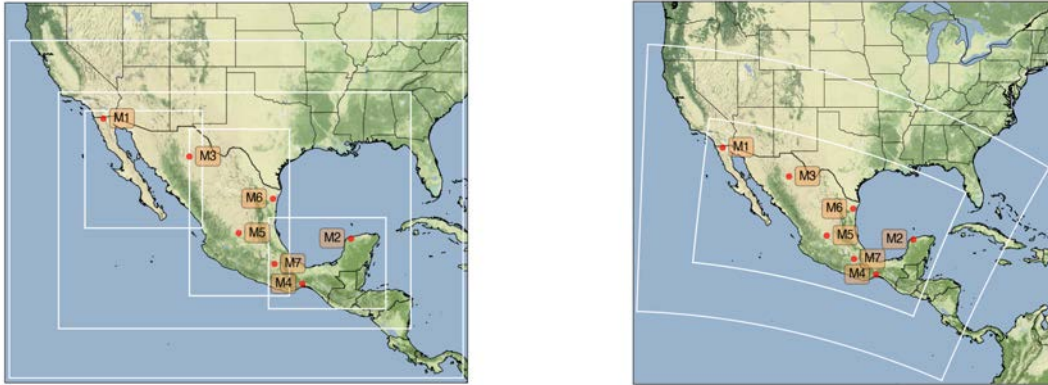


**Figure 3.2** – The WRF model projection used in the NEWA\_27KM (Mercator; left) and PROD\_DIFF2 (Lambert; right) simulations described in Fig. 3.3.

NEWA production run (Dörenkämper et al., 2020).

- The location of the vertical levels:  $h=0, 19.6, 40.3, 56.5$  m as in the MYNN-MO-UP experiment in Table 3.1, first level at 20 or 30 m above ground level using the automatic level determination available in WRF 4.2.1
- The source of the model land use: ESA-CCI (Poulter et al., 2015) or the standard MODIS. All simulations use the sub-tiling option for NOAH (Li et al., 2013).
- The surface roughness length of forest patches is increased to  $z_0 = 0.9$  m from the standard value of  $z_0 = 0.5$  m in the standard WRF vegetation table.
- Model numerical options: `diff_opt` and `gwd_opt` control whether gradients use full metric terms to more accurately compute horizontal gradients in sloped coordinates and gravity wave drag option, respectively

The sub-tiling option generates more realistic values of surface roughness length in areas of mixed vegetation, which could reduce the biases in wind speed (Santos-Alamillos et al., 2015).

Simulation	Projection	Grid spacing (size)	Physics	Land	Additional options
NEWA_9KM	Mercator	9 km, 3 km (403 x 271)	NEWA [h=0,19.6,40.3, 56.5,...]	ESA-CCI, mosaic forest=0.9m	
NEWA_27KM	Mercator	<b>27 km</b> , 9 km, 3 x 3 km	NEWA [h=0,19.6,40.3, 56.5,...]	ESA-CCI, mosaic forest=0.9m	
PROD_LAM	<b>Lambert</b>	<b>10 km, 3.33 km</b>	NEWA [h=0,30,68.2,116.7,...]	ESA-CCI, mosaic forest=0.9m	diff_opt=2 <b>gwd_opt=1,1</b>
PROD_DIFF1	Lambert	10 km, 3.33 km	NEWA [h=0,30,68.2,116.7,...]	ESA-CCI, mosaic forest=0.9m	<b>diff_opt=1</b> gwd_opt=1,0
PROD_DIFF2	Lambert	10 km, 3.33 km PROD_LAM grid	NEWA [h=0,30,68.2,116.7,...]	ESA-CCI, mosaic <b>forest=0.5m</b>	<b>diff_opt=2</b> gwd_opt=0
<b>PROD_3KM</b>	<b>Lambert</b>	<b>9 km, 3 km</b> <b>(550 x 370)</b>	<b>NEWA</b> <b>[h=0,30,68.2,116.7,...]</b>	<b>ESA-CCI, mosaic</b> <b>forest=0.9m</b>	<b>diff_opt=2</b> <b>gwd_opt=0</b>
PROD_3KM_20M	Lambert	9 km, 3 km (550 x 370)	NEWA <b>[h=0,20,43.8,72.2,...]</b>	ESA-CCI, mosaic forest=0.9m	diff_opt=2 gwd_opt=0
PROD_MER	<b>Mercator</b> <b>(larger)</b>	9 km, 3 km <b>(500 x 370)</b>	NEWA [h=0,30,68.2,116.7,...]	ESA-CCI, mosaic forest=0.9m	diff_opt=2 gwd_opt=0
PROD_3KM_SM	Lambert	9 km, 3 km	NEWA [h=0,20,43.8,72.2,...]	ESA-CCI, mosaic <b>forest=0.5m</b>	diff_opt=2 gwd_opt=0
PROD_MODIS	Lambert	9 km, 3 km	NEWA [h=0,20,43.8,72.2,...]	<b>MODIS land</b> forest=0.9	diff_opt=2 gwd_opt=0

**Figure 3.3** – Description of the sensitivity simulations. The text in red represents what is changed from the experiment directly above. The highlighted line represents the final configuration used in the production run.

## 3.2 Evaluation of the WRF ensemble simulations

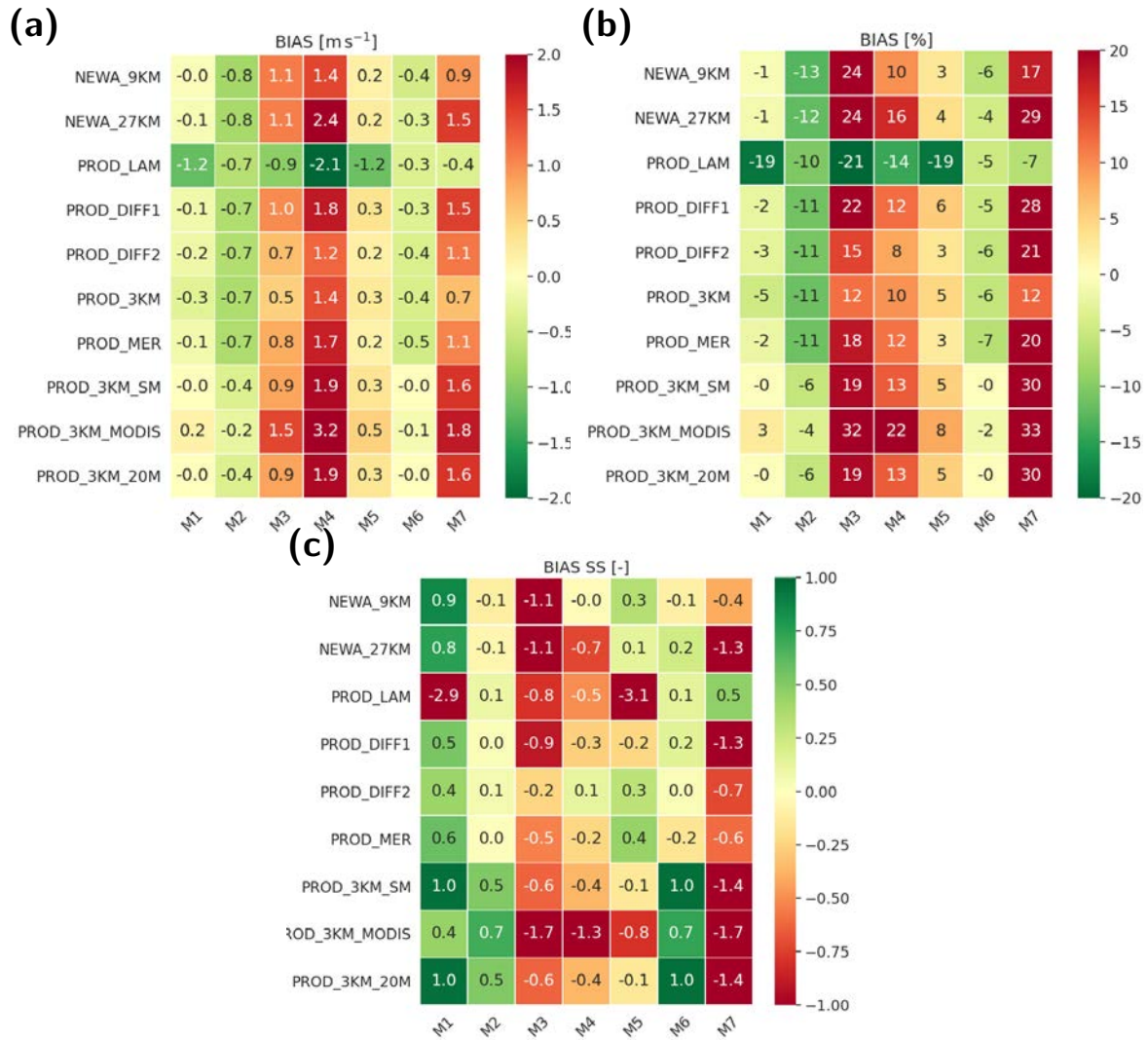
To facilitate the intercomparison among the ensemble members, we computed all the evaluation metrics of the wind speed for each simulation (Figs. 3.4–3.8). The metrics compare the observed wind speed (at 80 m) and wind direction (at 80 m) with the corresponding WRF-simulated time series interpolated to the same height. To better quantify the differences between the simulations, the figures also show the skill score (SS) using the PROD\_3KM simulation as baseline as defined in Chapter 2. Positive numbers (in green) show a increase in relative skill, which point to a more accurate simulation.

Figure 3.4 shows the statistics for the biases. As with the initial sensitivity simulations, biases are the largest for M4 and M7 and M3 in a relative sense, but considerable reduced from those in Fig. 3.1. No simulation shows improved biases from the PROD\_3KM simulation (Figure 3.4c).

Figures 3.5a and 3.5b provide further information about the sensitivity tests based on the EMD metric defined in Chapter 2 to evaluate the shape of the wind speed distributions. The worst simulated site is M4, with little variation from one simulation to another. The PROD\_3KM\_20M simulation provides smaller EMD at M1, M2 and M6, but considerably degrades the simulation of the wind speed distribution at M3 and M7.

Figure 3.6 examine the temporal correlation between the WRF-simulated wind speed and that observed at the masts. M1 and M4 show the highest correlations (above 0.8, except for one simulation) and M7 the lowest among all sites. The differences among the simulations are small, except for the PROD\_LAM simulation with increased grid spacing and activated gravity wave drag.

Similar patterns are seen for the RMSE in Fig. 3.7. But in terms of RMSE, the statistics



**Figure 3.4** – Evaluation metrics: (a) bias [ $\text{ms}^{-1}$ ], (b) relative bias [%] and (c) bias SS [-] between the observed and simulated wind speed at the seven WAM sites and 80 m height and the various sensitivity studies in the ensemble (Table 3.1) for the period 1 January to 11 February 2018. All SS are relative to the PROD\_3KM simulation.

of the PROD\_3KM simulation are worst at M3 and M7 than in any other simulation. The reason for this behaviour is unknown.

Finally Fig. 3.8 shows the statistics for the circular EMD (CEMD). Most simulations show CEMD between  $2\text{--}10^\circ$ , except for M4 with values above  $14^\circ$  except for the PROD\_LAM. This is likely an artifact of the distance between the selected grid point and mast location. No single simulation improves the CEMD at all sites.

In conclusion, two simulations, PROD\_3KM and PROD\_DIFF2 that differ only by the grid spacing are the top two contenders for the chosen configuration of the production run. In the last set of sensitivity simulations we run these two model configurations for one full year (2018). By mistake we also ran the PROD\_3KM\_SM simulation (analogous to PROD\_3KM, but with lower forest roughness). The results of this latest validation are shown in Fig. 3.9.



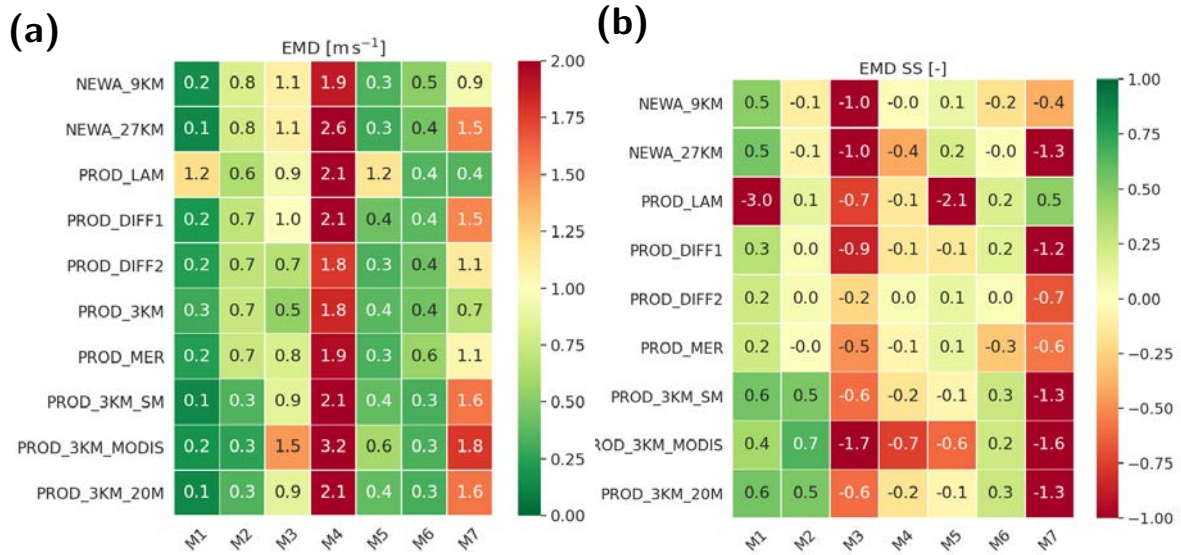


Figure 3.5 – As for Fig. 3.4 but for the (a) EMD and (b) EMD SS.

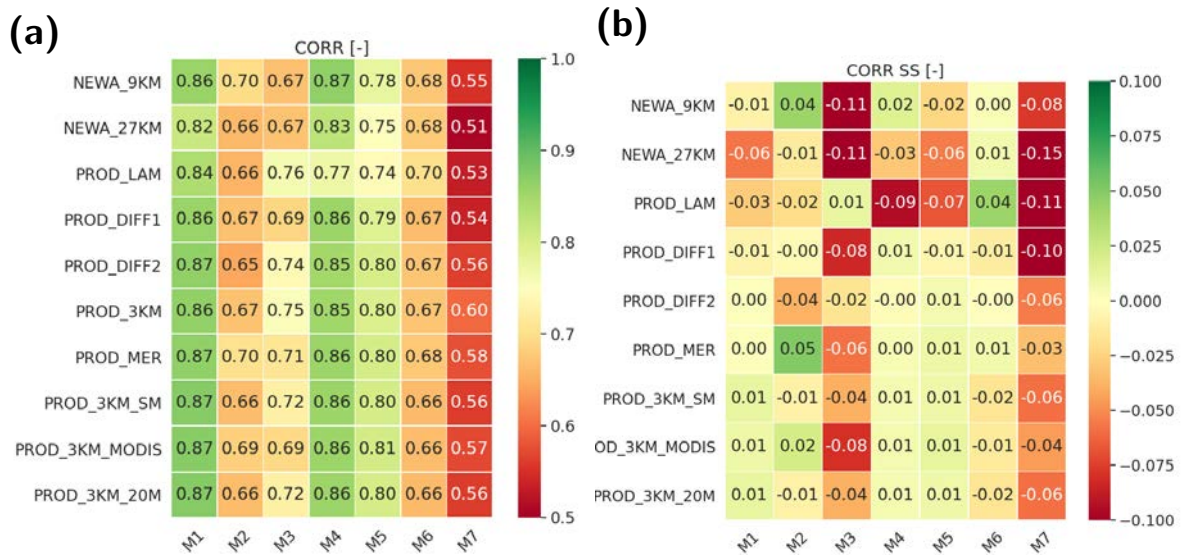


Figure 3.6 – As for Fig. 3.4 but for the synchronous correlation ( $r$ ) between the wind speed in the model and the observations.

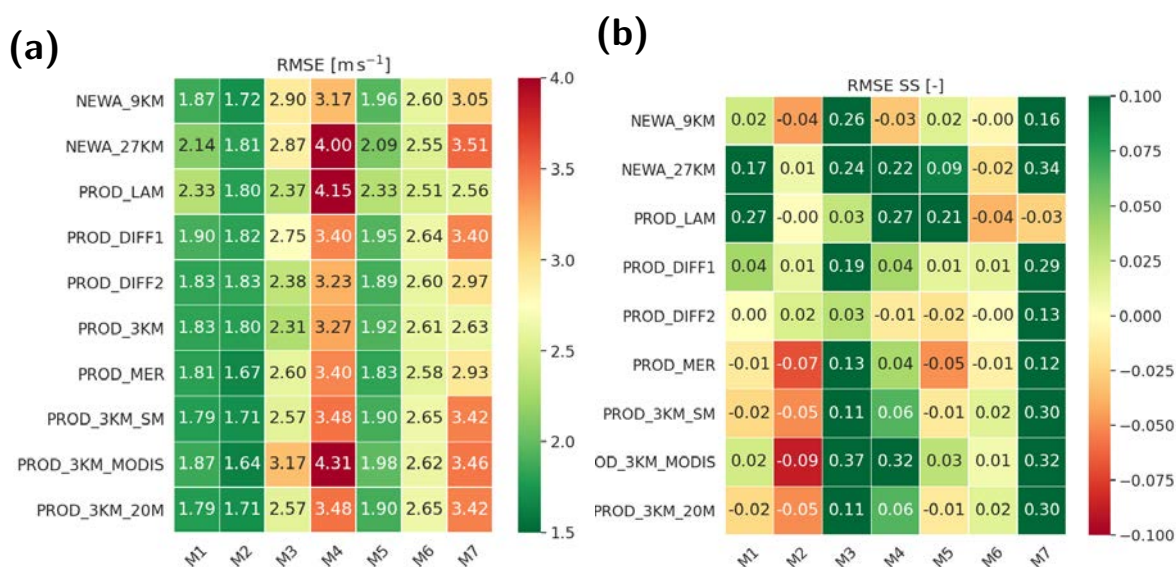


Figure 3.7 – As for Fig. 3.4 but for the (a) RMSE and (b) RMSE SS.

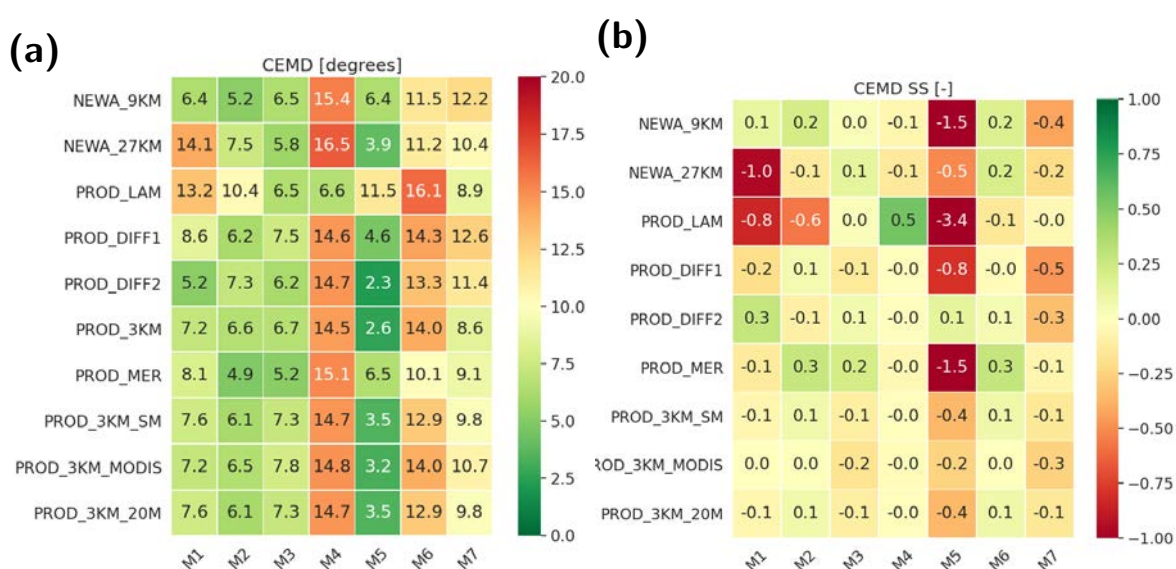
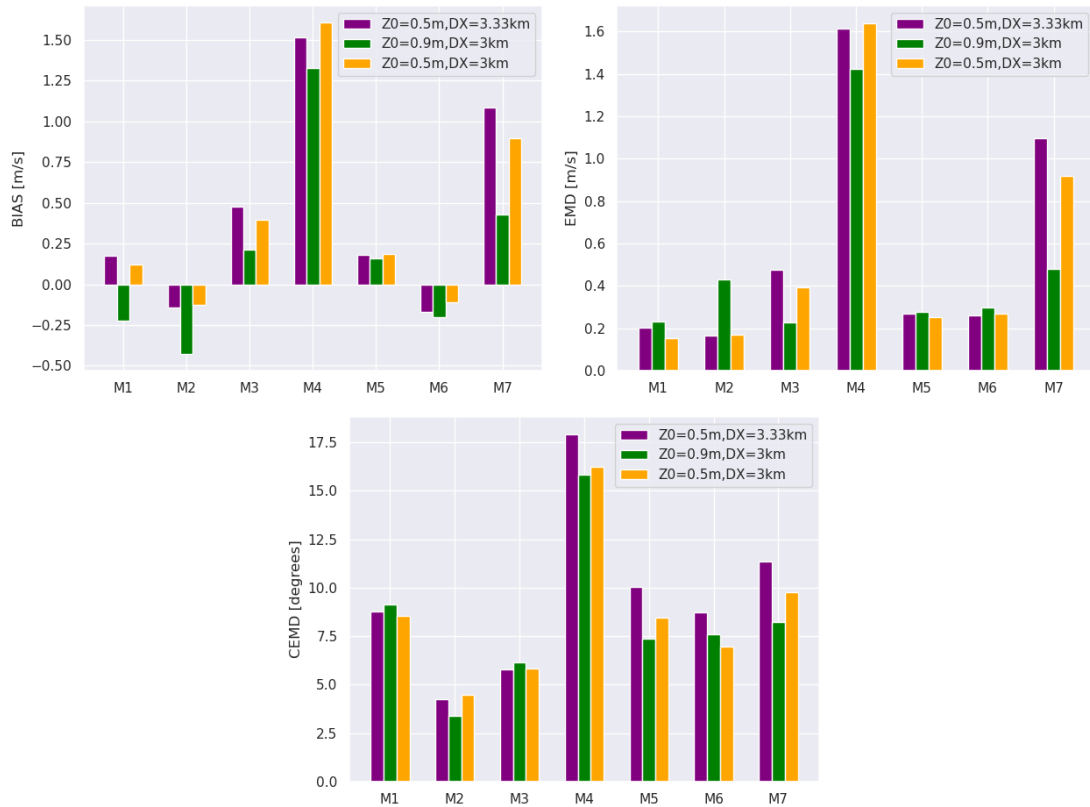


Figure 3.8 – As for Fig. 3.4 but for the (a) circular EMD and (b) CEMD SS.



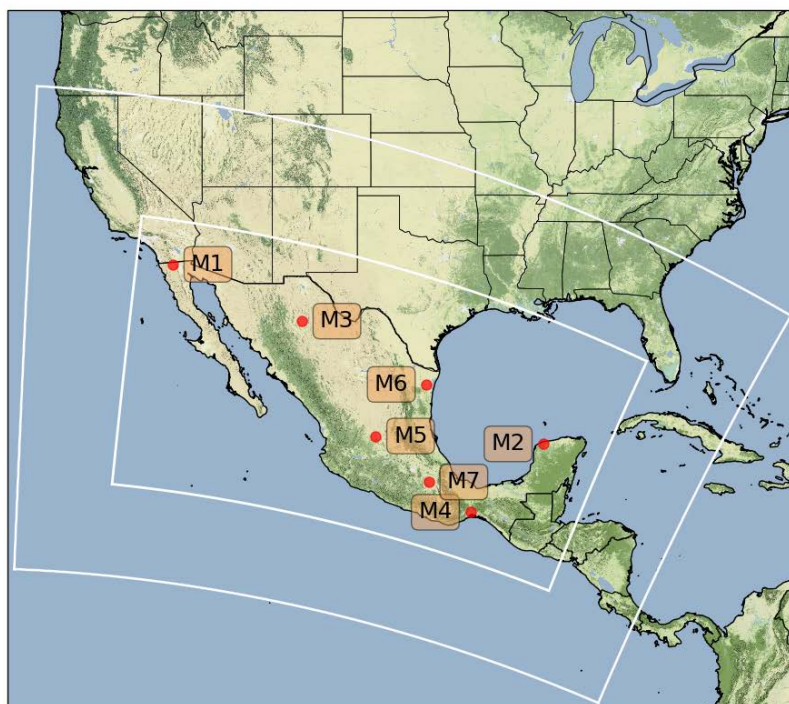
**Figure 3.9** – Comparison of the model statistics for wind speed and wind direction at 80 m for the PROD\_3KM, PROD\_DIFF2 and PROD\_3KM.SM simulations for the full year 2018.

Figure 3.9 compares the BIAS, EMD and CEMD between the best simulations in Table 3.3. For the two windiest sites, M4 and M7, the PROD\_3KM simulation shows improved statistics than the other two simulations. The WRF model grid spacing and surface roughness length are particularly important at M7.

In view of these results, the PROD\_3KM WRF model configuration was chosen for the 10-year production run.

### 3.3 The production run

The configuration of the production run is detailed in Table 3.2. The full namelist used in the simulations is presented in Appendix A.



**Figure 3.10** – WRF model grid configuration: D1:  $550 \times 370$  grid points (9 km) and D2:  $1165 \times 625$  grid points (3 km)

For the production run, we used a two-domain configuration, with 9 km and 3 km in the outer and inner grids, respectively; Fig. 3.10 shows the location of these domains. The model top was set to 50 hPa, following the best practices recommended by the WRF developers (Wang et al., 2019).

The terrain elevation and dominant land use classes are shown in Figures 3.11, and 3.12, respectively.



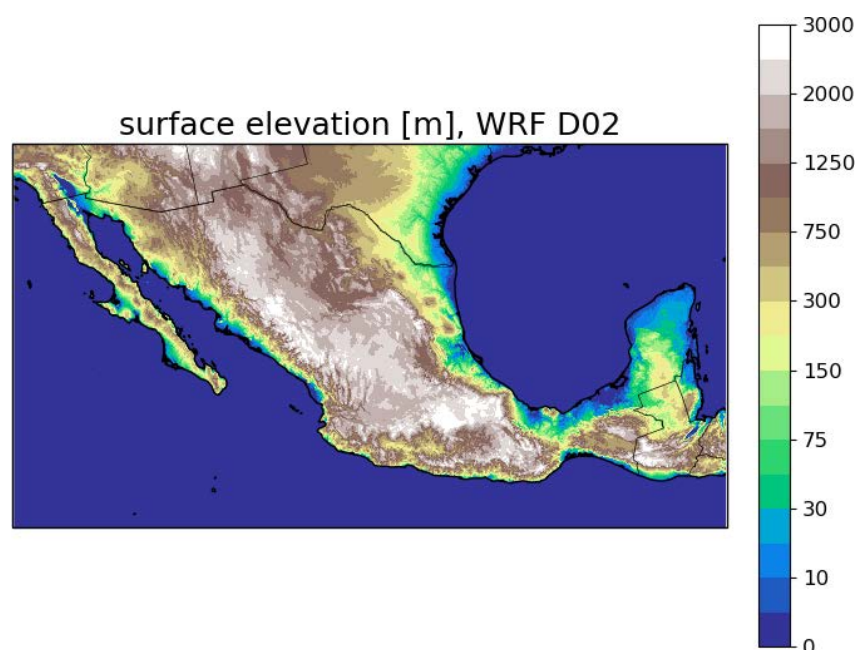


**Figure 3.11** – Terrain elevation of the WRF D2 ( $3\text{ km} \times 3\text{ km}$ ) domain.

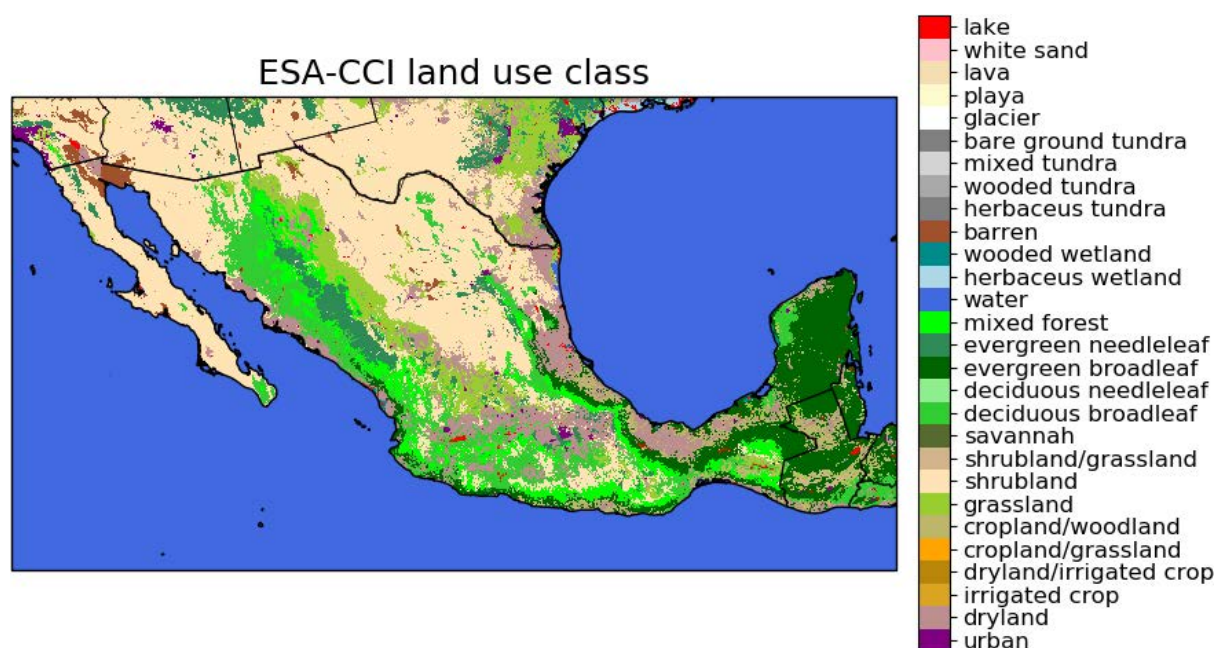


**Figure 3.12** – Dominant land use classification of the WRF D2 ( $3\text{ km} \times 3\text{ km}$ ) domain.

**Table 3.2** – WRF model configuration of the production run.

option	setting
WRF Model	WRF V4.2.1 released on July 22, 2020
Model grid	spacing: D1: 9 km / D2: 3 km Lambert conformal grid projection Grid centered at 102°W and 24.°S, with a 32° rotation Grid sizes: 550 × 370 (D1), 1165 × 625 (D2)
Terrain data	Global Multi-resolution Terrain Elevation Data 2010 at 30" ( <a href="#">Danielson and Gesch, 2011</a> )
Land use	ESA-CCI land-cover ( <a href="#">Poulter et al., 2015</a> ), converted to USGS categories.
Surface roughness length	As in Table C.1.
Vertical discretisation	61 vertical levels with model top at 50 hPa and first model full level at 30 m
Model levels	20 model levels below 1 km
Diffusion	Full (option 2), 2D deformation (option 4) 6th order positive definite numerical diffusion (option 2) No vertical damping Positive definite advection of moisture and scalars
Forcing data	ERA5 ( <a href="#">Hersbach et al., 2020</a> ) reanalysis at 0.25° × 0.25° on 34 pressure levels
Sea surface temperature	Operational Sea Surface Temperature and Sea Ice Analysis (OSTIA, <a href="#">Donlon et al., 2012</a> ) Lake temperatures from time-averaged ERA5 ground temperatures
PBL	MYNN ( <a href="#">Mellor and Yamada, 1982</a> )
Surface layer	M-O (Eta similarity) ( <a href="#">Janjic and Zavis, 1994</a> )
Land surface model	Unified Noah Land Surface Model ( <a href="#">Tewari et al., 2004</a> )
Cloud micro-physics	WRF Single-Moment 5-class scheme ( <a href="#">Hong et al., 2004</a> )
Cumulus convection	Kain-Fritsch Scheme ( <a href="#">Kain, 2004</a> ); D1 and D2
Nesting	One way nesting with smoothing (option 2)
Nudging	Spectral nudging U, V, T and q on D1 above level 20, no PBL nudging
Nudging constant	0.0003 s <sup>-1</sup>
Nudging wavelength	18 (x) and 12 (y) equivalent to about 400 km (synoptic wave length)

# Chapter 4

## Microscale modeling

### 4.1 Generalisation

According to the Numerical Wind Atlas concept, a generalized wind climate can be obtained by removing the effects of terrain and roughness from the mesoscale model grid ([Badger et al., 2014](#); [Lennard et al., 2015](#)). In [Hahmann et al. \(2021\)](#), it was shown that the generalization using PyWAsP had low absolute relative errors in power density and therefore that approach is used. The generalization as described in [Dörenkämper et al. \(2020\)](#), which relies on the linearized flow model LINCOM to compute orographic speedups, was not tested here.

The generalization procedure relies on the WAsP model engine version 12.7, which is part of PyWAsP version 0.5. The default wind profile setting was used and the baroclinicity model was switched off ([Floors et al., 2015, 2018](#)).

At present, there is no method to obtain geostrophic shear from the WRF model and using it from another source, such as ERA5, would have introduced issues with the ERA5 tiles being visible in the output. In [Hahmann et al. \(2021\)](#), it was shown that the new stability model performed better than the default model, but since this feature has not yet been released, users currently have no access to it. Therefore, the default model was used for the final high-resolution wind atlas.

For the topography modeling, the 'spider-grid' roughness analysis was used, which keeps the terrain description in its original land cover classes together with a lookup table when processing the zooming grid around the point of interest ([Floors et al., 2021](#)). The size of the first grid cell is 25 m and the radial length of a cell in a wind direction sector increases with 5% for each consecutive radial grid cell starting from the origin. For the computation of the orographic speedups, the Bessel expansion on a zooming grid (BZ) model was used. The BZ model is extensively described in Ch. 8.5 in [Troen and Petersen \(1989\)](#). Although it generally gives good results in simple terrain, it is known to have issues in complex terrain. Due to its linearized nature, flow separation that occurs when the terrain slopes are more than  $\approx 30\%$  ( $17^\circ$ ) cannot be modeled. This results in the calculation of too high speedup effects at sites that are located near the top of a hill or mountain. Therefore, the ruggedness index (RIX) is used to identify the ability of the BZ model to correctly calculate orographic speedups ([Mortensen et al., 2006](#)). It is defined as the percentage of slopes that are steeper than 30% in a circle of 3.5 km around the point of interest.

## 4.2 Downscaling

The downscaling was performed with PyWAsP version 0.5 with the same configuration as the generalization procedure (see previous section). For the computation of the orographic speedups the high resolution elevation obtained from NASA's Shuttle Radar Topography Mission (SRTM) version 3 were used as input. The data were void-filled with the Viewfinder DEM data (De Ferranti, 2012). These elevation data have a resolution of 3" ( $\approx 90$  m).

**Table 4.1** – Overview of the different microscale configurations that were evaluated.

Microscale model	Land cover table
PyWAsP	DTU
PyWAsP	EMD
PyWAsP	WRF <sub>low</sub>
PyWAsP	WRF <sub>high</sub>

The 2015 ESA-CCI dataset was used for high-resolution land cover data (Poulter et al., 2015). To translate each class of the raster to surface roughness values, four different conversion tables were tested (See Table C.2 in the appendix). The way these lookup tables were generated is based on subjective estimates of what  $z_0$  values gives the correct behavior of the logarithmic wind profile over different types of surfaces. The four tables are:

- 'DTU': a lookup table developed by DTU that has been used for the Global Wind Atlas (Badger et al., 2015)
- 'EMD': Refers to EMD International and is the lookup table used in the windPRO software and was obtained from EMD's website (Thøgersen, 2020)
- 'WRF<sub>low</sub>' and 'WRF<sub>high</sub>': are lookup tables that use the corresponding roughness values used in the WRF model setup, with either low or high roughness values (see the forest=0.5 m and forest=0.9 m simulations in Fig. 3.3 for WRF runs with either the low or high table). In previous modeling studies, it was found that the generalization procedure performed better when using similar roughness values for both WRF and PyWAsP (Dörenkämper et al., 2020).

## 4.3 Procedure for microscale validation steps

For validation against the observations, the WRF grid cell nearest to the mast cup (in both space and height) was generalized, as described in section 4.1 using the WRF maps. Subsequently, following section 4.2, the downscaling was performed to the exact height of the mast measurement height, using the high-resolution elevation and land cover maps with the different roughness conversion tables. The generalization was performed in the WRF-native metric projection (Lambert conformal conic) and the downscaling was done in the local metric UTM projection. Because the downscaled results obtained from PyWAsP are given as sector-wise Weibull  $A$  and  $k$  parameters and the validation was performed on wind climate histograms (bins of wind speed and direction), they cannot be directly compared to the observed wind climates. Therefore the distributions were transformed to histograms with 12 30° wide sectors and 30 one  $\text{m s}^{-1}$  wide wind speed bins, matching the observed histograms.

## 4.4 Production of the microscale wind atlas

The final high-resolution wind resource maps (see section 6.1) was produced using PyWAsP at a resolution of  $0.0025^\circ$  ( $\approx 250$  m). A geographical projection on latitude/longitude grid was chosen as the output model grid (WGS84, identified by EPSG code 4326). Because WAsP is based on point calculations, the results are calculated on these exact points, although all input information used in PyWAsP has to be in a projected (metric) coordinate system. For the calculation projection the local UTM zone was used. In total about 91 million output points are calculated per map layer, which calls for paralleling during calculation. To achieve this, Mexico was decomposed in tiling steps, first into MGRS zones, and secondly each MGRS zone was decomposed into  $800 \times 800$  grid tiles for doing the calculations. In the PyWAsP downscaling tiling artifacts between each calculation tile are avoided by using a natural neighbor interpolation of the generalized wind climates and by preprocessing far-upstream surface roughness values.

To run the individual calculation tiles with PyWAsP (version 0.5), the PyWAsP-swarm package (Version 0.1) was used to parallelize the tasks. This version of PyWAsP corresponds to WAsP version 12.7, which will be available for download on [www.wasp.dk](http://www.wasp.dk) later in 2021. WAsP 12.7 uses ERA5-derived variables (temperature, specific humidity, surface pressure and lapse rate) for estimating the local air densities (Floors and Nielsen, 2019) when computing the power density.

# Chapter 5

## Wind atlas validation

### 5.1 Evaluation of WRF ensemble including downscaling

To understand the sensitivity of the complete model-chain, the majority of the WRF sensitivity experiments were downscaled using the WAsP model generalization (see Section 4.1) and downscaling procedures (see Section 4.2). Four different lookup tables for the ESA-CCI land cover classes were evaluated for the downscaling.

In table 5.1, the results, from the PyWAsP procedure with different WRF experiments and land cover tables as input, are shown. Results from the raw WRF production simulation and from ERA5 are also included as reference. The ERA5 is one of the most popular reanalysis datasets used to obtain historical meteorological data and thus provides a good baseline for comparison. Results from the rest of the raw mesoscale simulations can be seen in section 3. The results in table 5.1 are shown in terms of the average MAPE in power density and wind speed for the six masts with RIX below 2%. This RIX threshold to define non-complex sites was also used in (Dörenkämper et al., 2020). The numbers correspond to the one year validation period, covering the year 2018.

From table 5.1 it is clear that PyWAsP using the WRF production setup and the land cover table that corresponds to the WRF roughnesses ( $WRF_{high}$ ) give the best results (11.7 % MAPE for  $P$ ), while the raw WRF results from the production setup comes second (14.7 % MAPE for  $P$ ). The ERA5 output from the nearest grid cell clearly fails to accurately estimate the MAPE in  $P$  and  $U$ , with errors of  $\approx 53\%$  and  $\approx 25\%$ , respectively. These numbers reflect an underestimation of the wind speed at all sites.

The second best performing PyWAsP results comes from using the production setup but with lower-roughness values ("PROD\_3KM\_SM") together with the  $WRF_{high}$  land cover table for downscaling. On the other hand, using  $WRF_{low}$  with the "PROD\_3KM\_SM" WRF simulation results in overestimation of wind speeds and power density, reflected in a MAPE of  $P$  of 21.3 %. The initial five WRF sensitivity simulations have much greater errors than the final production setup, which is also reflected in the downscaled results (27.8 % MAPE of  $P$  at best).



**Table 5.1** – The MAPE in power density ( $P$ ) and wind speed ( $U$ ) at all masts with RIX below 2% (only M7 is excluded) using the PyWAsP microscale model chain and one of the four different land cover tables for different mesoscale WRF experiments (see Tables 3.1 and 3.3). The MAPE are relative to the year 2018 in simulations and observations. For reference, raw ERA5 and the WRF production run results are also shown. The results are ordered by lowest MAPE  $P$ . A constant air density of  $1.225 \text{ kg m}^3$  is used for calculating the power density.

Model	WRF experiment	Land cover table	MAPE $U$ [%]	MAPE $P$ [%]
WAsP	PROD_3KM	WRF <sub>high</sub>	5.6	11.7
WRF	PROD_3KM	WRF <sub>high</sub>	6.2	14.7
WAsP	PROD_3KM_SM	WRF <sub>high</sub>	6.9	15.0
WAsP	PROD_3KM	EMD	5.9	16.9
WAsP	PROD_3KM_SM	EMD	7.0	18.9
WAsP	PROD_3KM	DTU	7.8	19.2
WAsP	PROD_3KM	WRF <sub>low</sub>	7.4	19.4
WAsP	PROD_3KM_SM	WRF <sub>low</sub>	6.7	21.3
WAsP	PROD_3KM_SM	DTU	9.0	21.7
WAsP	MYNN-MO-5KM	WRF <sub>high</sub>	12.2	27.8
WAsP	MYNN-MO-5KM	EMD	12.2	30.3
WAsP	MYNN-MO-5KM	WRF <sub>low</sub>	11.6	32.2
WAsP	MYNN-MO	WRF <sub>low</sub>	11.4	33.7
WAsP	MYNN-MO-UP	WRF <sub>low</sub>	11.4	34.2
WAsP	MYNN-MO	WRF <sub>high</sub>	13.6	34.8
WAsP	MYNN-MO-5KM	DTU	14.3	34.8
WAsP	MYNN-MYNN	WRF <sub>low</sub>	11.2	34.8
WAsP	MYNN-MYNN	WRF <sub>high</sub>	13.1	34.8
WAsP	MYNN-MO	EMD	12.9	35.1
ERA5	ERA5	ERA5	24.7	52.9

## 5.2 Validation at all sites of the WRF production run and PyWAsP downscaling

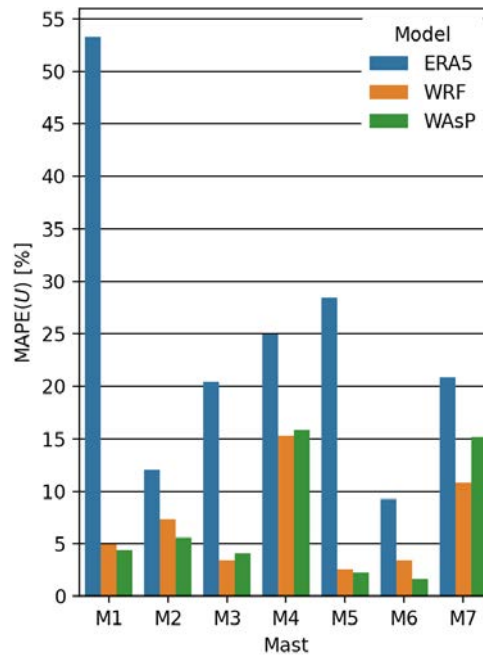
A comparison between the observed wind climatology at the 80 m level of the masts and both WRF and downscaled WRF results is presented in Table 5.2. For comparison, the same results are also graphically shown in Fig. 5.1. Mast M7 has a RIX higher than 2% and is, therefore, not included in the overall aggregated scores. ERA5 underestimates the wind speed at all sites, but the relative underestimation varies considerably from mast to mast, from a MAPE of  $U$  of about 9% at M6 to 53% at M1. Mast M4 and M7 are located in complex terrain. Mast M7 due to the steep orography and surrounding forests, and mast M4 due to the extreme conditions related to the gap-flow in the region and strong variation in surface roughness nearby. At both those masts, M4 and M7, WRF and PyWAsP show large overestimation of wind speed (more than 10% MAPE of  $U$ ). At the rest of the sites, both WRF and PyWAsP have MAPE of  $U$ 's between 1 and 7%.

Finally, in Figs. 5.2 and 5.3 we show the distributions of MAPE for mean wind speed and mean power density with and without mast M7, the mast in the most complex terrain with RIX above 2%. We leave M7 out in the final results because of the special behavior of the

Mast	$U_o$ ( $\text{m s}^{-1}$ )	RIX [%]	$U_m$ ( $\text{m s}^{-1}$ )			MAPE of $U$ (%)		
			ERA5	WRF	PyWAsP	ERA5	WRF	PyWAsP
M1	6.8	0.3	3.2	6.4	6.5	53.3	5.0	4.4
M2	6.3	0.0	5.5	5.8	5.9	12.0	7.4	5.6
M3	5.0	0.0	4.0	5.2	5.2	20.4	3.4	4.1
M4	9.4	0.0	7.1	10.8	10.9	25.0	15.3	15.8
M5	5.9	0.09	4.2	6.0	6.0	28.4	2.6	2.2
M6	7.2	0.0	6.5	7.0	7.1	9.3	3.4	1.7
M7	4.3	2.6	3.4	4.8	5.0	20.9	10.9	15.2
Mean (RIX $\pm$ 2%)	6.8	-	5.1	6.9	6.9	24.7	6.2	5.6

**Table 5.2** – Comparison of the mean wind speed at 80 m AGL for all WAM masts for the observations ( $U_o$ ) and both ERA5, raw WRF, and after downscaling with PyWAsP ( $U_m$ ). All numbers represent concurrent wind speed data for the year 2018 validation period.

**Figure 5.1** – MAPE in the long-term wind speed at 80 m AGL for all sites.



linearized flow model used in PyWAsP. In complex terrain, with very steep slopes, it can lead to overestimations. It is usually recommended to run CFD simulations in such places. The error distribution of the mean wind speed and power density biases shows the large underestimation in the ERA5 data very clearly. Both the WRF and the downscaled simulations perform much better. Considering all the seven masts, WRF and the downscaled results overestimate the wind speed and power density on average (Fig. 5.2). After removing M7, both WRF and PyWAsP has mean biases very close to zero and the downscaled simulations have the lowest spread of the models, but a slightly larger bias than WRF. These figures indicate that there is a value of applying a full meso- and microscale model chain in non-complex terrain.



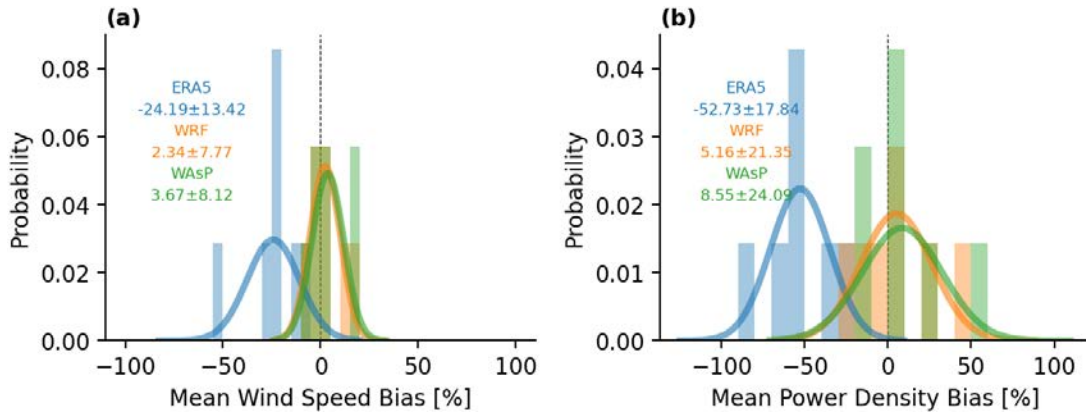


**Figure 5.2** – Distribution of the bias in wind speed (left) and power density (right) for the ERA5, ERA5+WRF (WRF) and ERA5+WRF+PyWAsP (WAsP) downscaling at all 7 sites at 80 m AGL. A constant air density of  $1.225 \text{ kg m}^{-3}$  is used for calculating the power density.

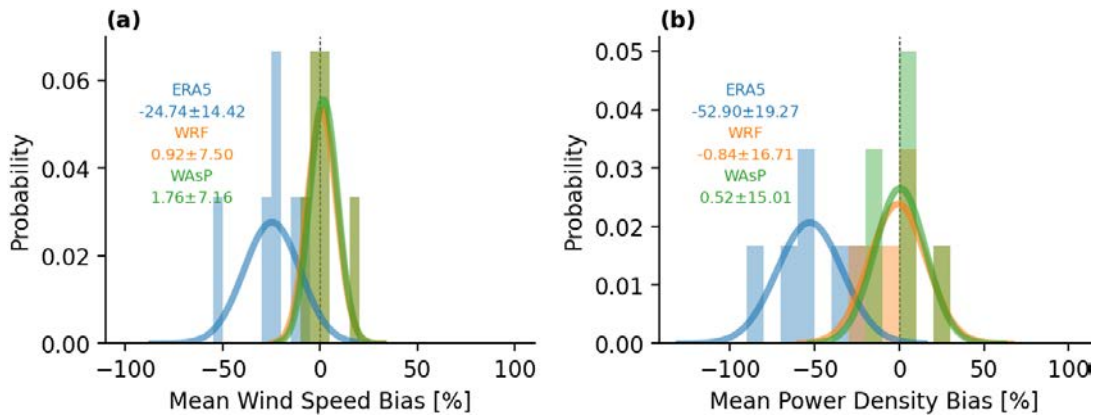


**Figure 5.3** – Distribution of the bias in wind speed (left) and power density (right) for the ERA5, ERA5+WRF (WRF) and ERA5+WRF+PyWAsP (WAsP) downscaling at all sites with a RIX below 2% (M7 removed) at 80 m AGL. A constant air density of  $1.225 \text{ kg m}^{-3}$  is used for calculating the power density.

### 5.3 Validation at each site



**Figure 5.4** – Location of all the validation sites. The blue outline is the outer edge of the WRF D2 domain.

To understand the details of the topography and the simulations results at each site, a more extensive validation is performed in the following parts. For illustrative purposes, we present the WRF roughness and elevation maps and the high-resolution roughness and elevation maps used for microscale modeling in the sensitivity study (section 5.1). Visualizing these maps also helps us in checking that computations related to e.g. the transformation of map projections were performed correctly, and that the maps appear consistent with aerial views of the site (see appendix B), which is recommend when doing a wind resource assessment using the WAsP software. The land cover maps from both the ESA-CCI dataset, which was used for both WRF and microscale modeling, and from the 2019 Copernicus land use classification dataset, are also shown, giving further indication of the accuracy and consistency of the input maps.

The observed wind climatology, in terms of wind roses and wind speed distributions, of the measurements from the masts are compared with the corresponding modeling results from ERA5, the raw WRF production, and downscaling. The local wind climate varies during the year and during the day, so to investigate how well WRF is able to reproduce these patterns we compare heatmaps of mean wind speed separated into hour and month groups. In all the following figures and descriptions, the validation period, year 2018, is used. Also, the measurements and model simulations (at 60 min frequency) are synchronised and always contain the same amount of samples.

### 5.3.1 La Rumorosa (M1)

The first mast of the WAM project is located near La Rumorosa in the northern part of Baja California, Mexico. The surface elevation is approximately 1350 m at the location of the mast, the terrain is dry and the climate arid (Fig. 5.8). The surrounding land-cover is mostly shrub-land (Fig. 5.6 and 5.7). In WRF (Fig. 5.8b) the roughness length varies between low and high roughness due to a mixture of shrub-land and forest patches in the ESA-CCI land-cover dataset.

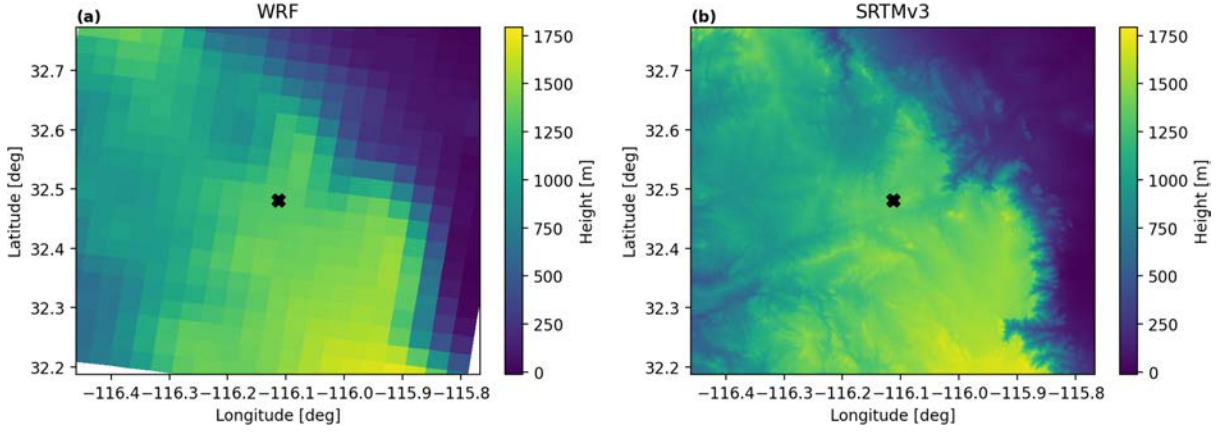


**Figure 5.5** – Surface elevation maps around mast M1 obtained from the WRF simulations (a), and from the high-resolution SRTMv3 data set (b).

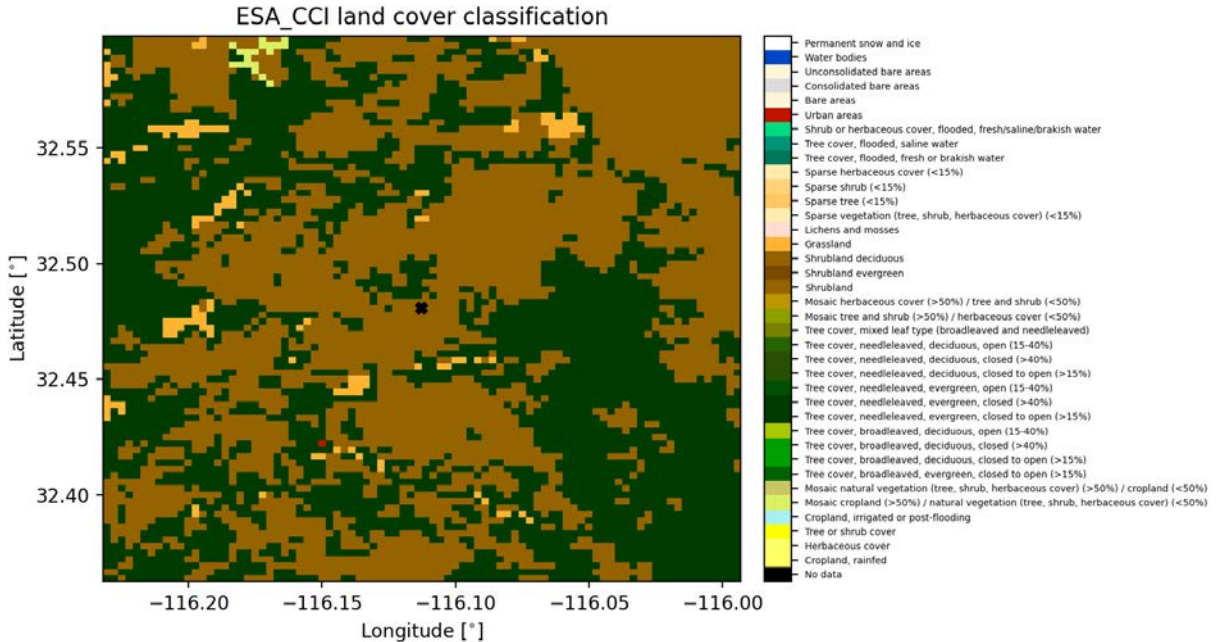


**Figure 5.6** – ESA-CCI land use classification at mast M1.

The observed and simulated wind climates at M1 are shown in Fig. 5.9 and 5.10. The predominant wind direction is from the southwest. This is captured well by the models.

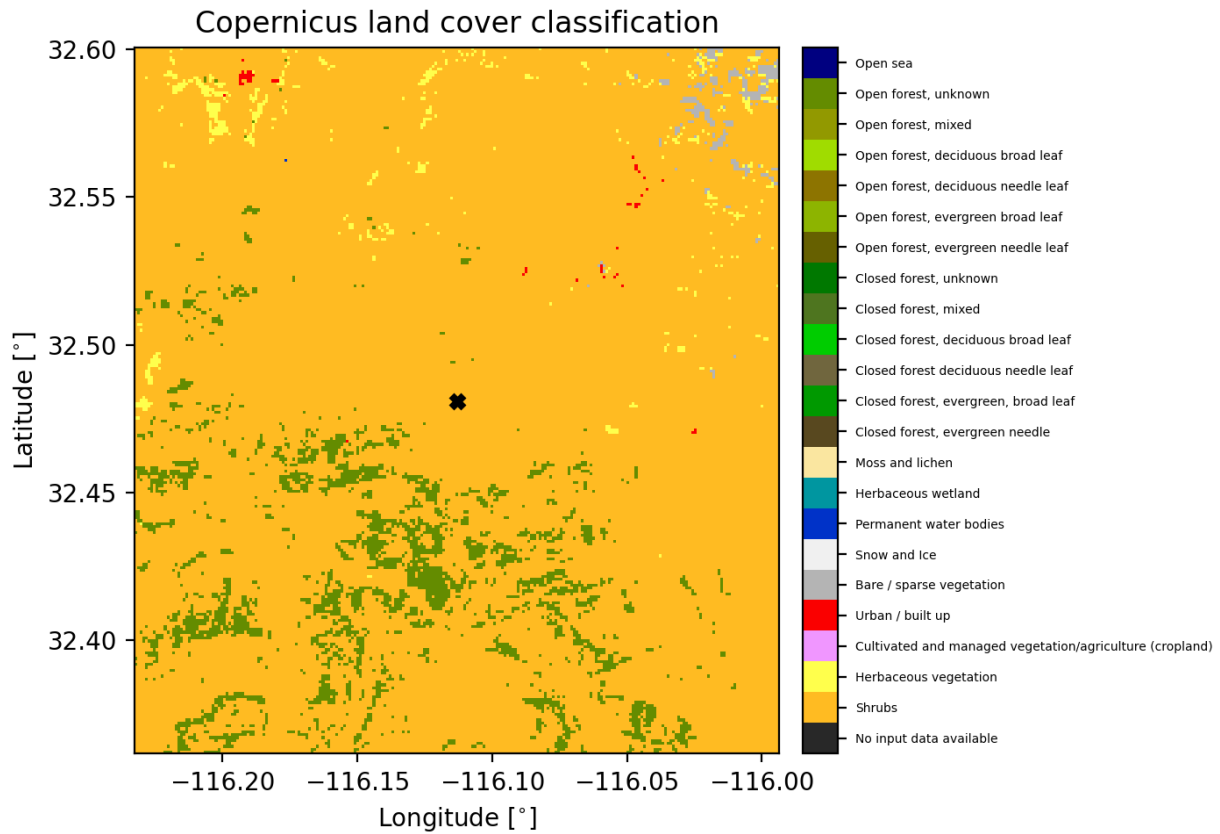


**Figure 5.7** – Copernicus land use classification for the year 2019 at mast M1.

The WRF simulation drastically improves the wind speed distributions compared to that from ERA5, which underestimates the wind speed significantly. The PyWAsP downscaling overestimates the extreme ends of the wind speed distribution compared to those from WRF.

The amplitude of the diurnal and annual cycles in wind speed (Fig.5.11) are notable. The wind speed has a minimum in the summer months and around mid-day. The maximum wind speeds occur during the spring months and the night time. The phase and amplitude of these cycles are generally well captured by the WRF model simulations.



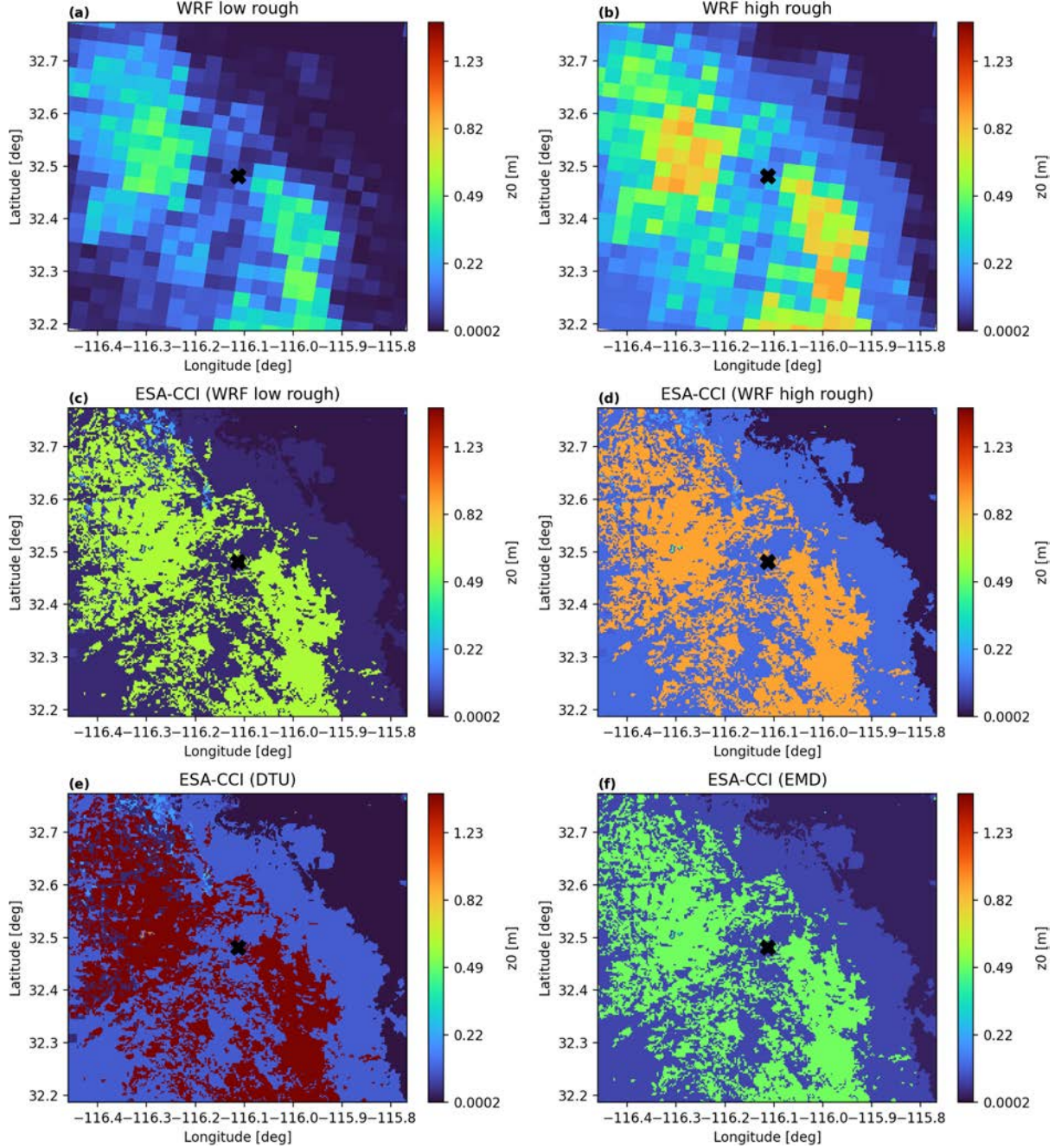


**Figure 5.8** – Surface roughness length maps around mast M1 obtained from the WRF simulations using low (a) and high (b) surface roughness, from the high-resolution ESA-CCI land cover generated with the low roughness WRF (c), high roughness WRF (d), DTU (e) and EMD (f) lookup tables.

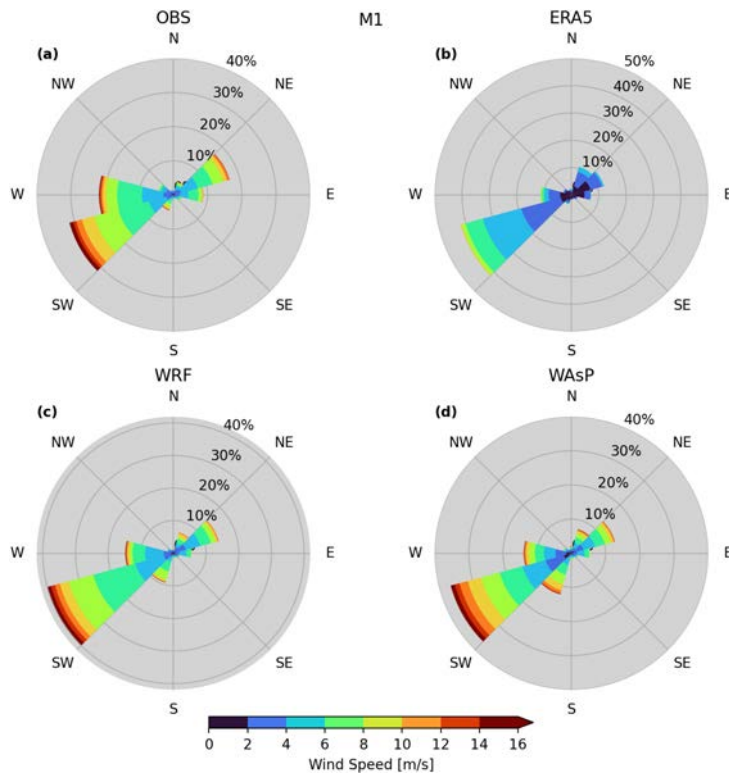


**Figure 5.9** – Observed and simulated wind climatologies at 80 m AGL at site M1 during 2018: (a) observed, (b) ERA5, (c) raw WRF production run, (d) PyWAsP downscaling.

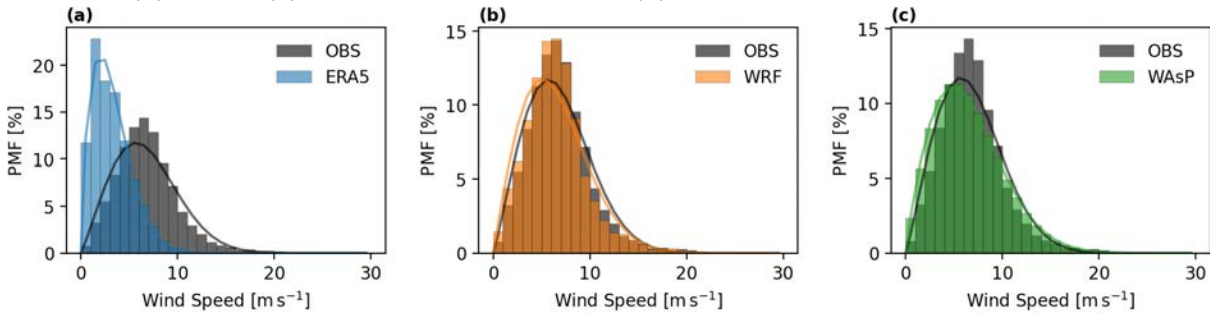


**Figure 5.10** – Observed and simulated (a) ERA5, (b) WRF and (c) PyWAsP frequency distribution of wind speed at 80 m AGL at site M1 during 2018.

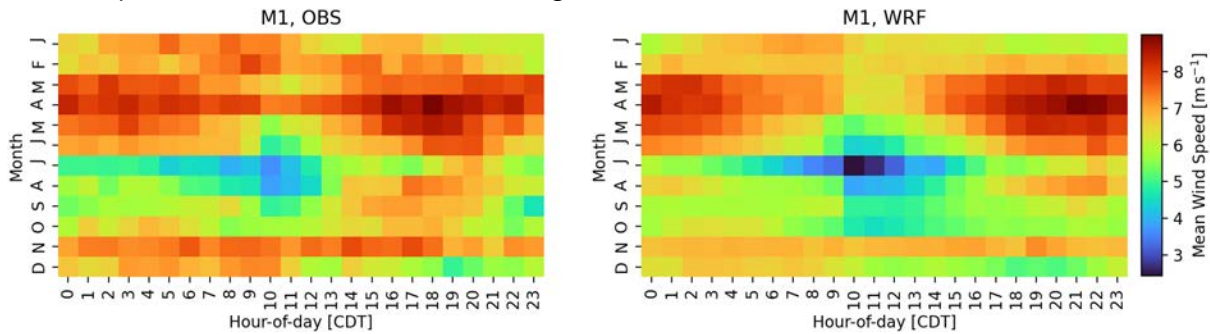


**Figure 5.11** – Observed and WRF-simulated seasonal and diurnal cycle of wind speed at 80 m AGL at site M1 during 2018. Times are in Central Daylight Time.

### 5.3.2 Mérida (M2)

Site M2 is located near the city of Mérida in the northern coast of the Yucatan in Mexico. The site is flat (Fig. 5.12) and the vegetation consists of mainly deciduous trees. The climate is hot and semi-arid. The surface roughness length at the site is high (Fig. 5.15), varying from about 0.5 m to about 1.0 m for the different land-cover lookup tables.

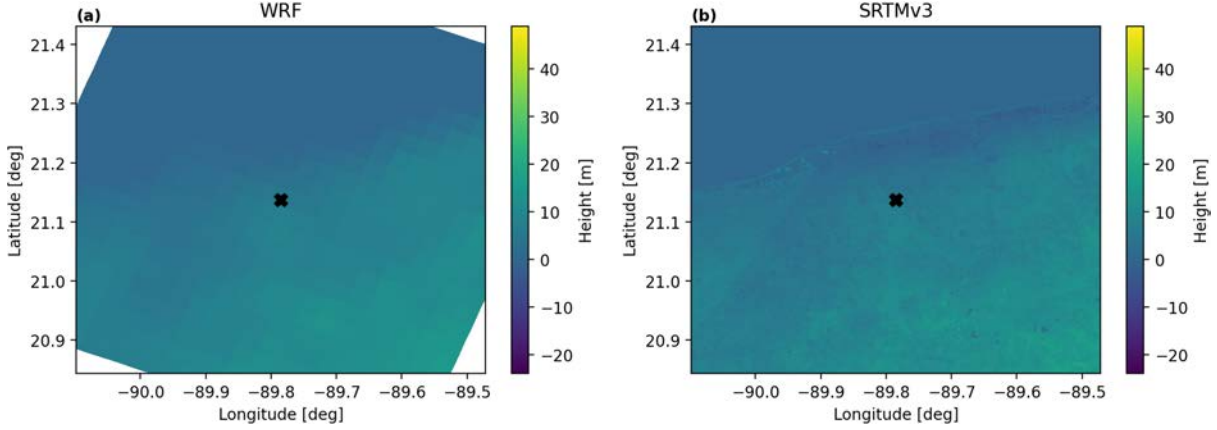


**Figure 5.12** – Surface elevation maps around mast M2 obtained from (a) the WRF simulations, and (b) the high-resolution SRTMv3 data set.

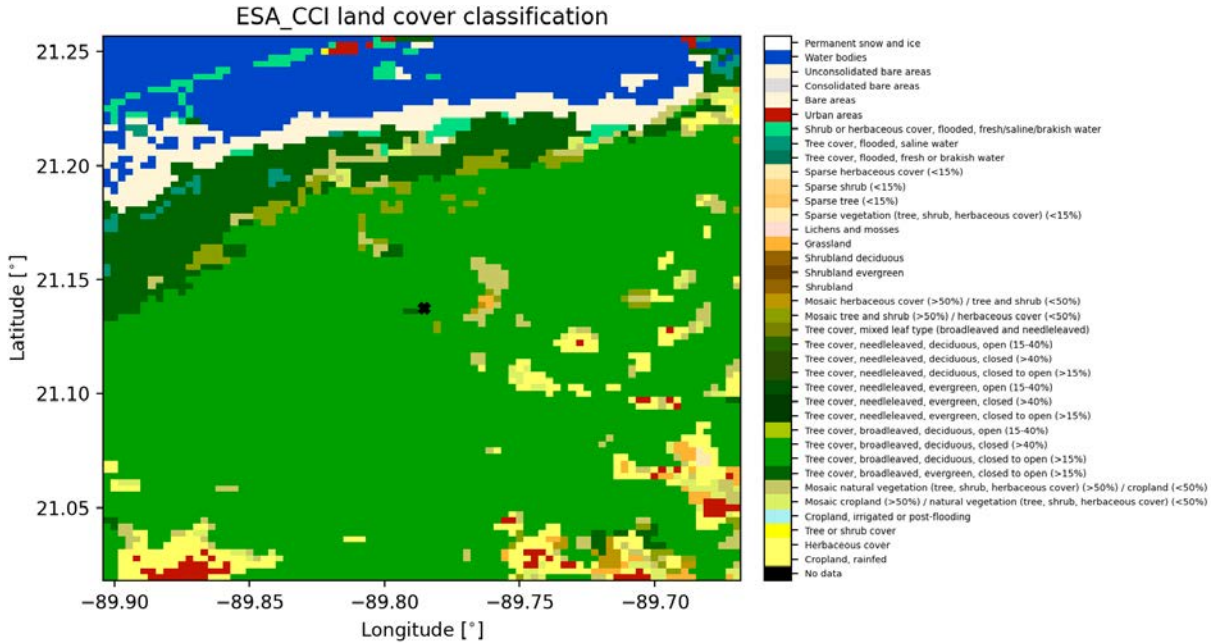


**Figure 5.13** – ESA-CCI land use classification at mast M2.

The observed and simulated wind climate at M2 are shown in Fig. 5.16. The site is influenced by the trade winds and the wind roses also show that the wind comes predominantly from the east. The models capture the wind roses well. The wind speed distributions (Fig. 5.17) reveal a small underestimation of the wind speed by ERA5, while WRF captures the



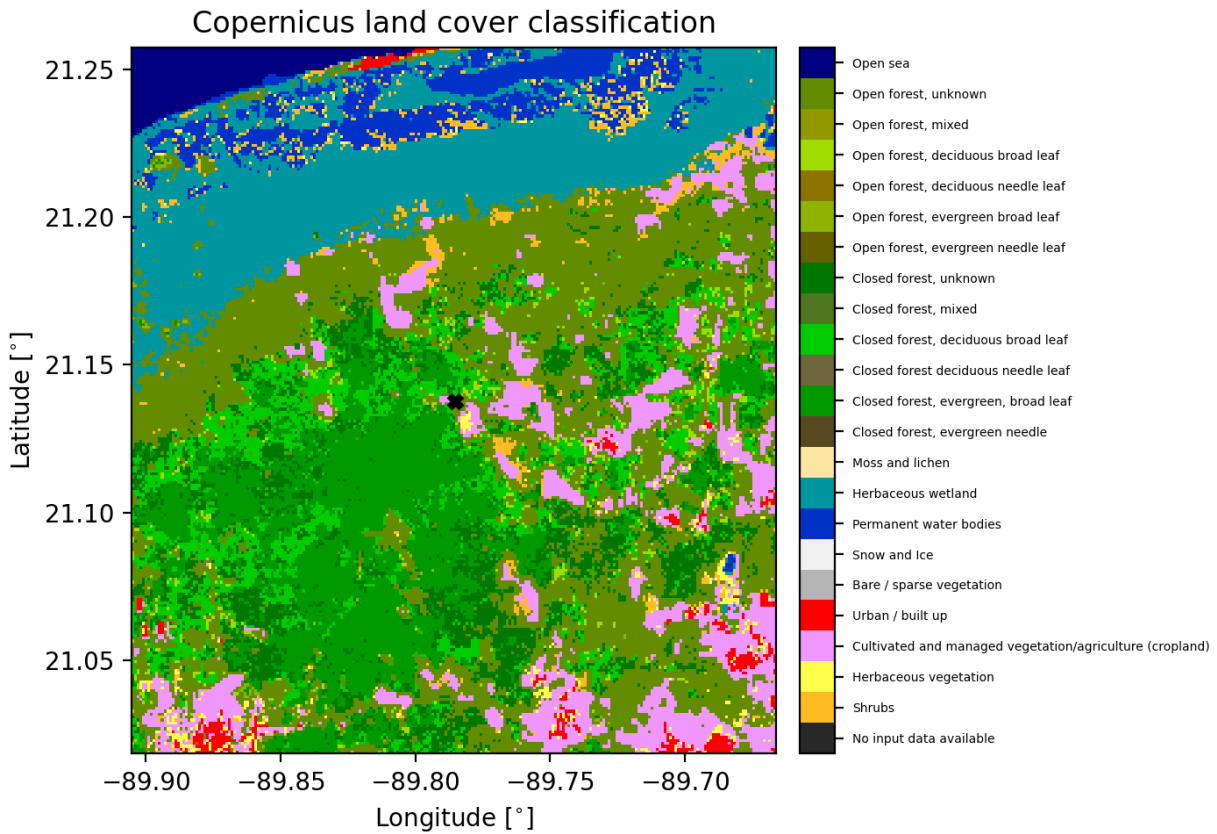


**Figure 5.14** – Copernicus land use classification for the year 2019 at mast M2.

distribution better. Downscaling with PyWASP, does not change the wind speed distribution much compared to WRF.

The annual and seasonal cycles (Fig. 5.18), shows that the diurnal cycle is strongest in the spring and summer months, with the strongest winds happening in the afternoon hours. The annual cycle is not very pronounced, but the wind is strongest in the winter season. WRF captures the patterns, but under predicts the strong winds during the evening hours, with a 4 hours lag that over predicts the calms during the morning hours. A phase error between the strong and weak winds is also present, with the WRF peak wind speeds happening later than in the observations.



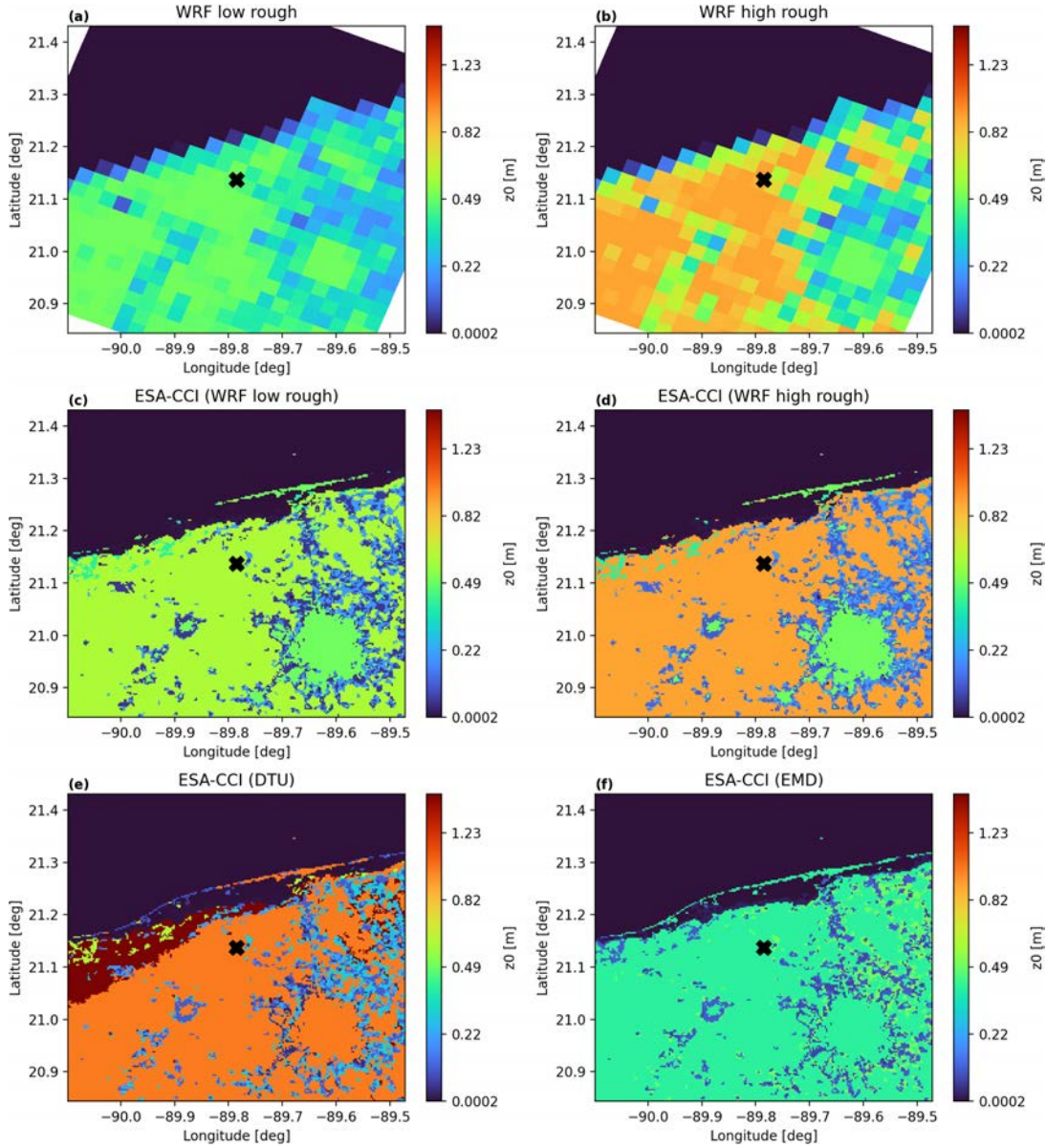


**Figure 5.15** – Roughness maps around mast M2 obtained from the WRF simulations using low (a) and high (b) surface roughness, from the high-resolution ESA-CCI land cover generated with the low roughness WRF (c), high roughness WRF (d), DTU (e) and EMD (f) lookup tables.

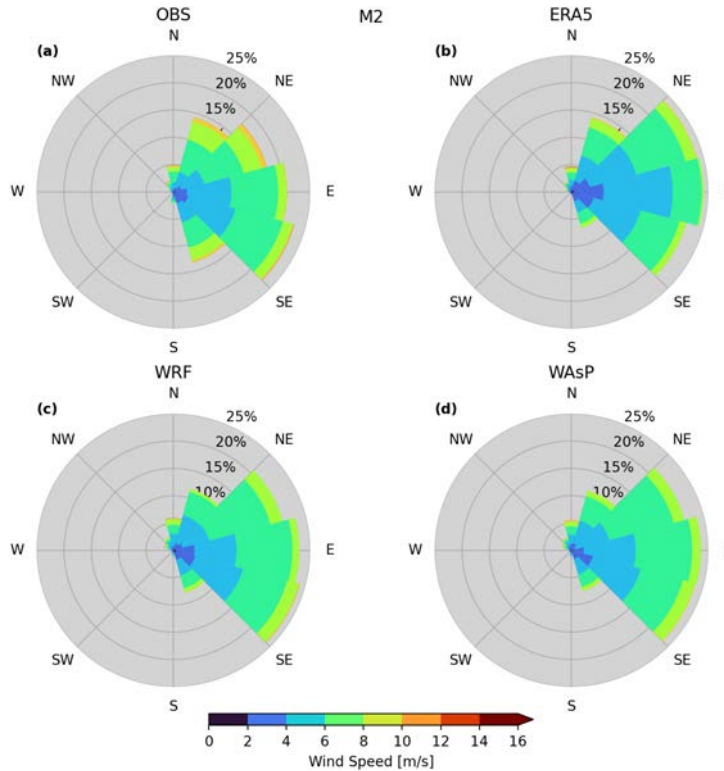


**Figure 5.16** – Observed and simulated wind climatologies at 80 m AGL at site M2 during 2018: (a) observed, (b) ERA5, (c) raw WRF production run, (d) PyWAsP downscaling.

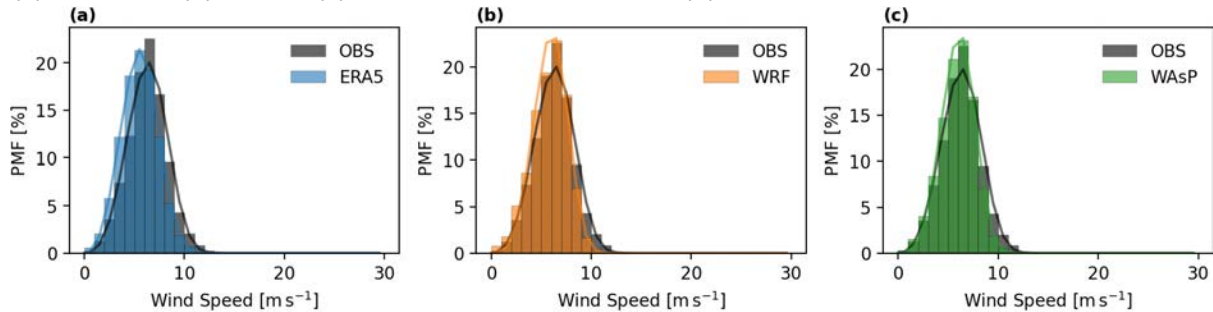


**Figure 5.17** – Observed and WRF-simulated frequency distribution of wind speed at 80 m AGL at site M2 during 2018.

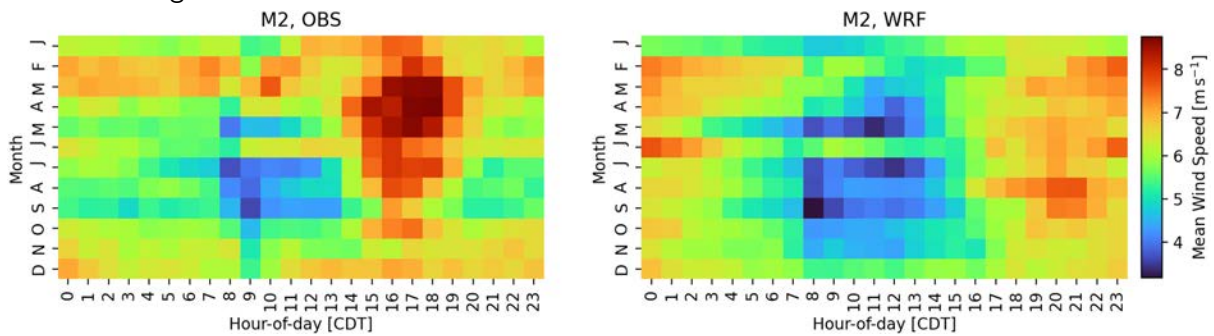


**Figure 5.18** – Observed and WRF-simulated seasonal and diurnal cycle of wind speed at 80 m AGL at site M2 during 2018. Times are in Central Daylight Time.

### 5.3.3 Ciudad Cuauhtémoc (M3)

The M3 mast is located in the Chihuahua region of Mexico. The area is at a high altitude more than 2 km above sea-level (Fig. 5.19), and has a semi-arid climate. The land-cover in the area is mostly grass- and shrub-lands, with patches of forest about 5–10 km away to the south. This manifests in the surface roughness (Fig. 5.22) maps as very low roughness very near the site, but higher roughness to south and south west.

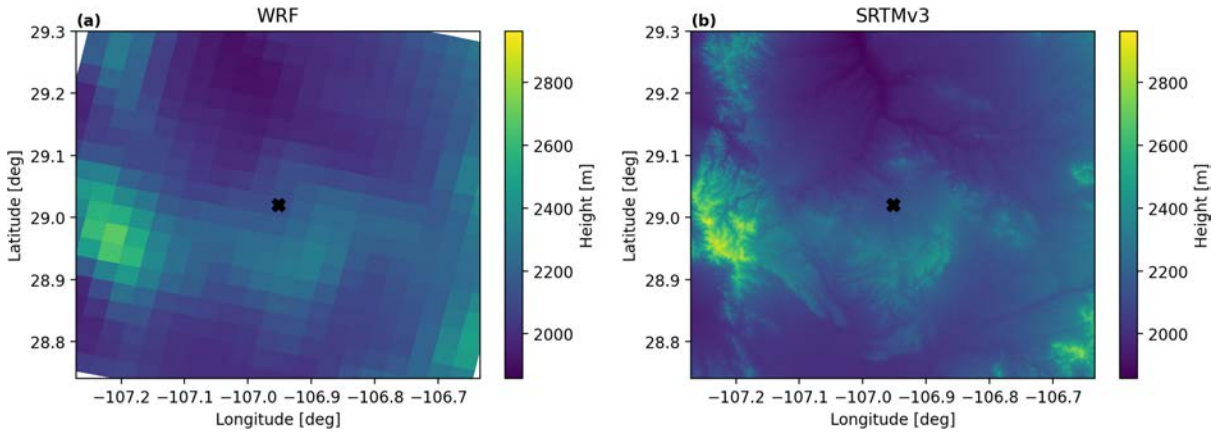


**Figure 5.19** – Surface elevation maps around mast M3 obtained from the WRF simulations (a), and from the high-resolution SRTMv3 data set (b).

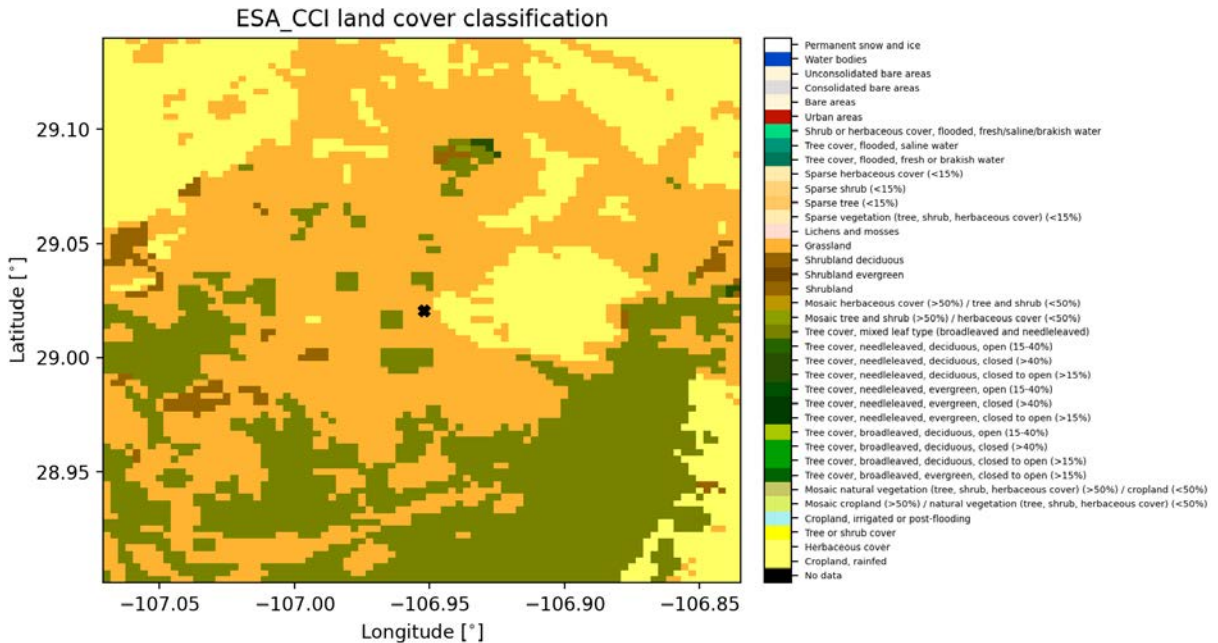


**Figure 5.20** – ESA-CCI land use classification at mats M3.

The observed and simulated wind climate at M03 are shown in Fig. 5.23 and 5.24. The wind roses show that the predominant wind directions are from the south and southwest, which correspond to the areas with forest patches of open land and forests. ERA5 does not

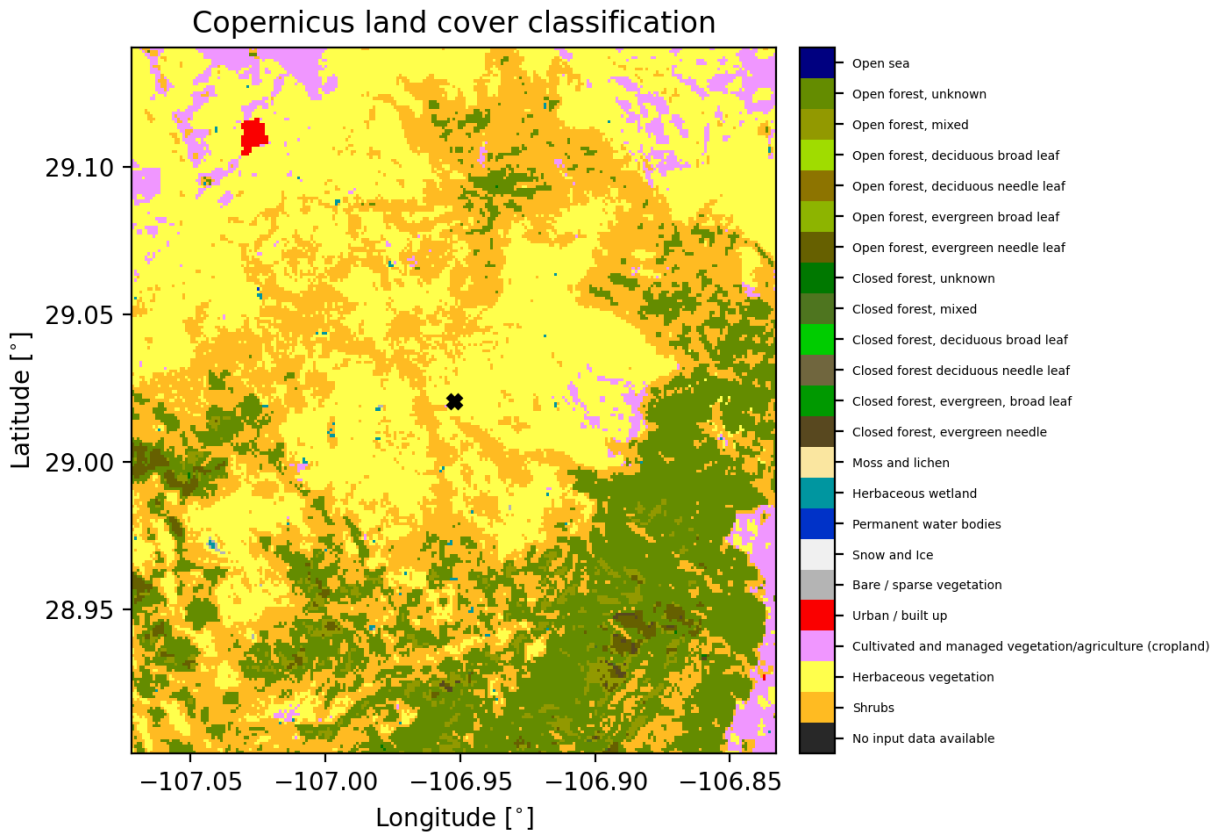


**Figure 5.21** – Copernicus land use classification for the year 2019 at mats M3.

capture the wind rose accurately and shows a predominant wind direction from the west. WRF and PyWAsP on the other hand captures the wind rose better, but with a predominant wind direction further to the southwest, than the observed. The wind speed distributions (Fig. 5.24) show that ERA5 underestimates the wind speed at the site, while WRF and PyWAsP capture the distribution more accurately.

At M3, winds are stronger during the spring and during the afternoon and evening hours (Fig. 5.25). The diurnal and annual cycles of the wind speed are very well simulated by WRF.



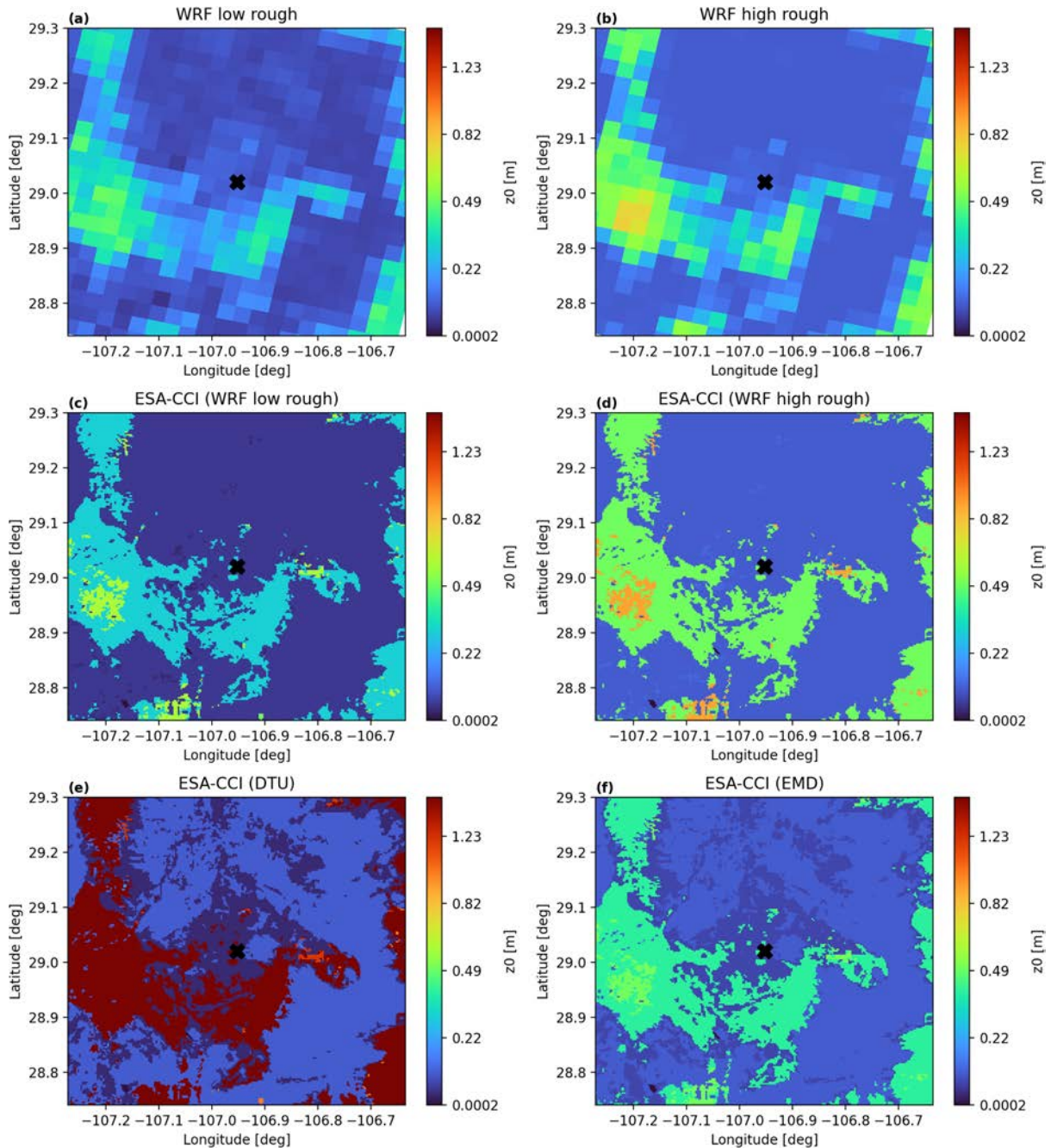


**Figure 5.22** – Roughness maps around mast M3 obtained from the WRF simulations using low (a) and high (b) surface roughness, from the high-resolution ESA-CCI land cover generated with the low roughness WRF (c), high roughness WRF (d), DTU (e) and EMD (f) lookup tables.

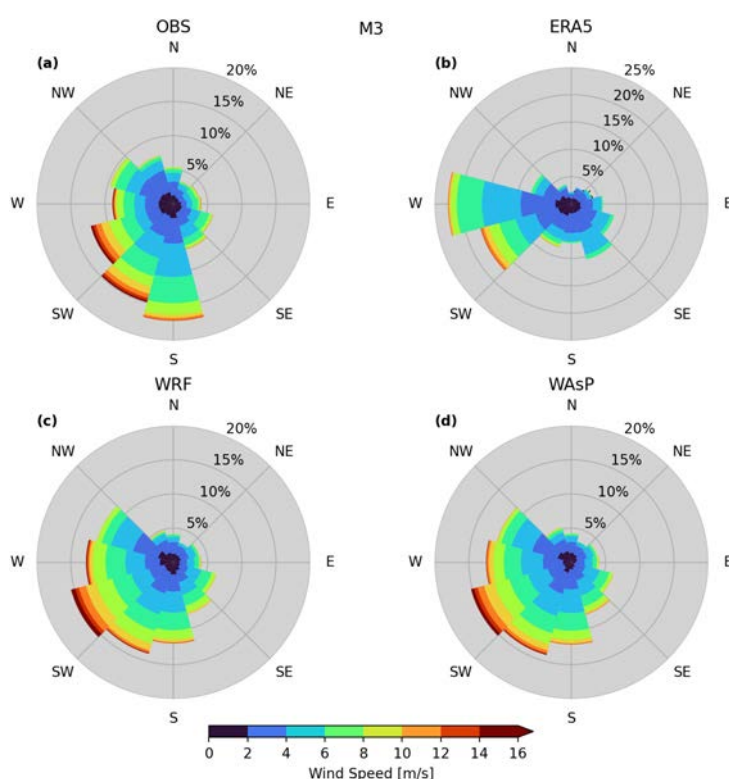


**Figure 5.23** – Observed and simulated wind climatologies at 80 m AGL at site M3 during 2018: (a) observed, (b) ERA5, (c) raw WRF production run, (d) PyWAsP downscaling.

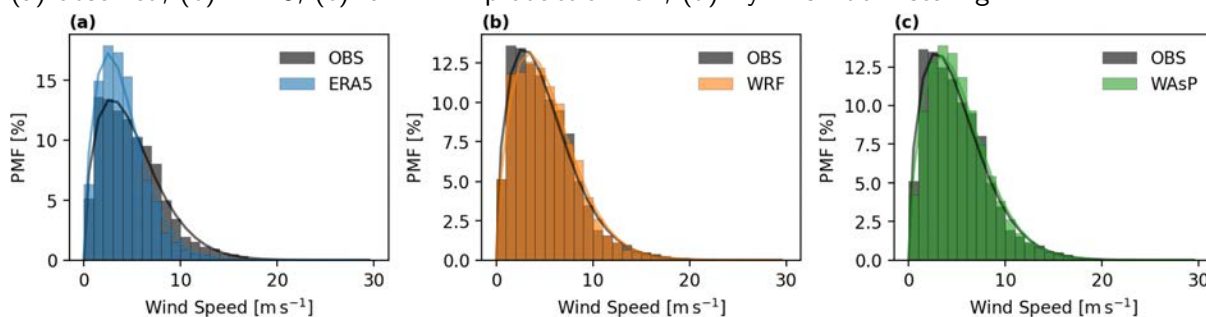


**Figure 5.24** – Observed and WRF-simulated frequency distribution of wind speed at 80 m AGL at site M3 during 2018.

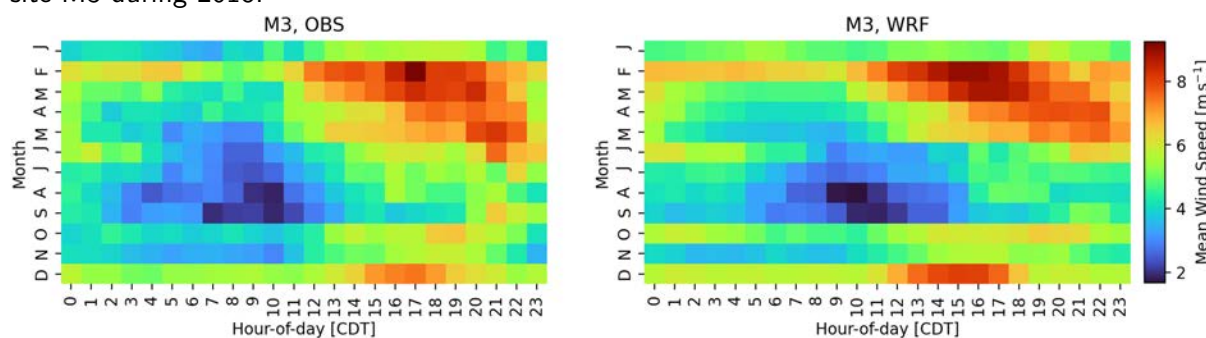


**Figure 5.25** – Observed and WRF-simulated seasonal and diurnal cycle of wind speed at 80 m AGL at site M3 during 2018. Times are in Central Daylight Time.

### 5.3.4 Certe (M4)

The M4 mast is located in the Chivela Pass which is heavily influenced by the Tehuano wind (Tehuantepecer), a strong northerly gap flow taking place in-between the Mexican and Guatemalan mountains. The site is located in mostly flat terrain, but with a gentle slope towards the coast to the south and larger mountain ranges to the north, east, and west of the site (Fig. 5.26). The surrounding land-cover is a mixture of urban / built-up land, forest patches, cultivated land, and grassland. Large parts of the Chivela pass is populated with rows of wind turbines. This heterogeneity of the land-cover is also reflected in the surface roughness in the area (Fig. 5.29).

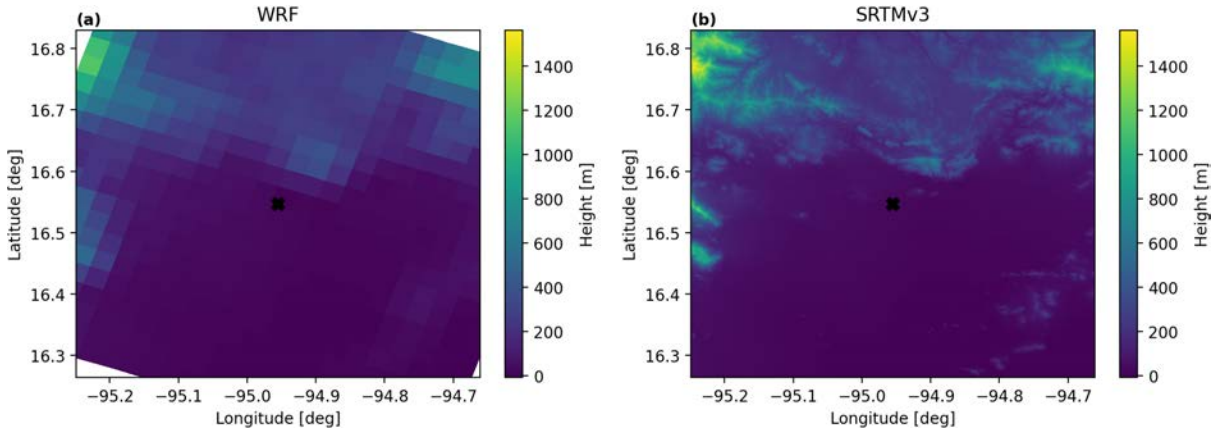


**Figure 5.26** – Surface elevation maps around mast M4 obtained from the WRF simulations (a), and from the high-resolution SRTMv3 data set (b).

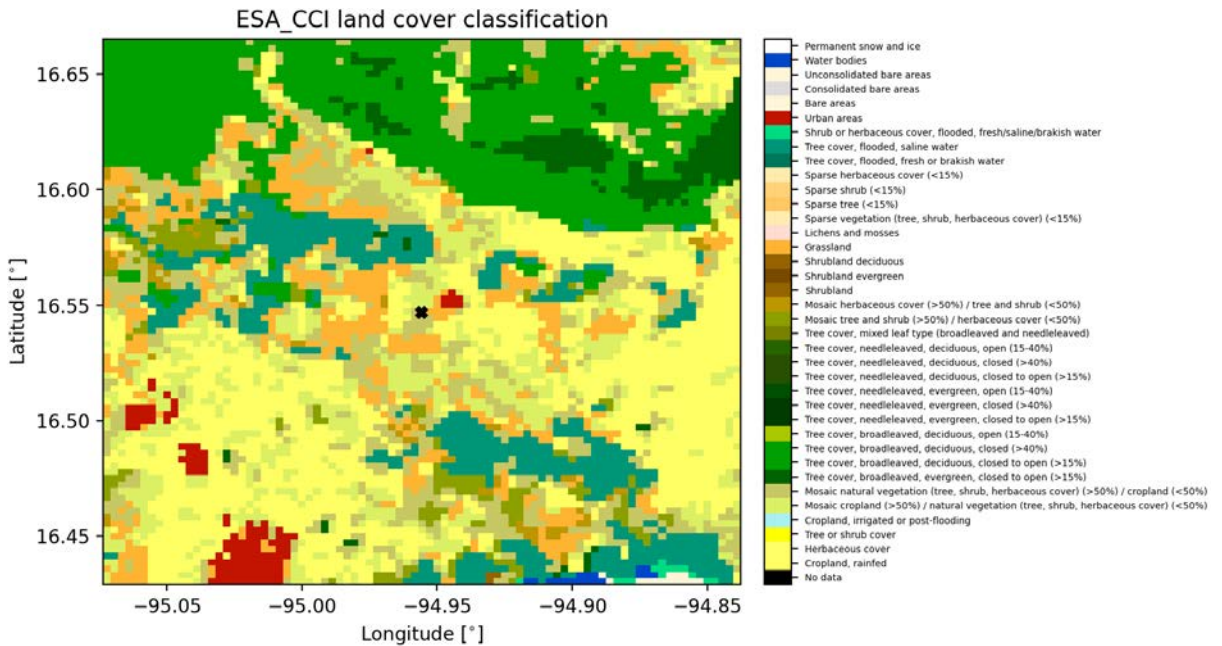


**Figure 5.27** – ESA-CCI land use classification at mats M4.



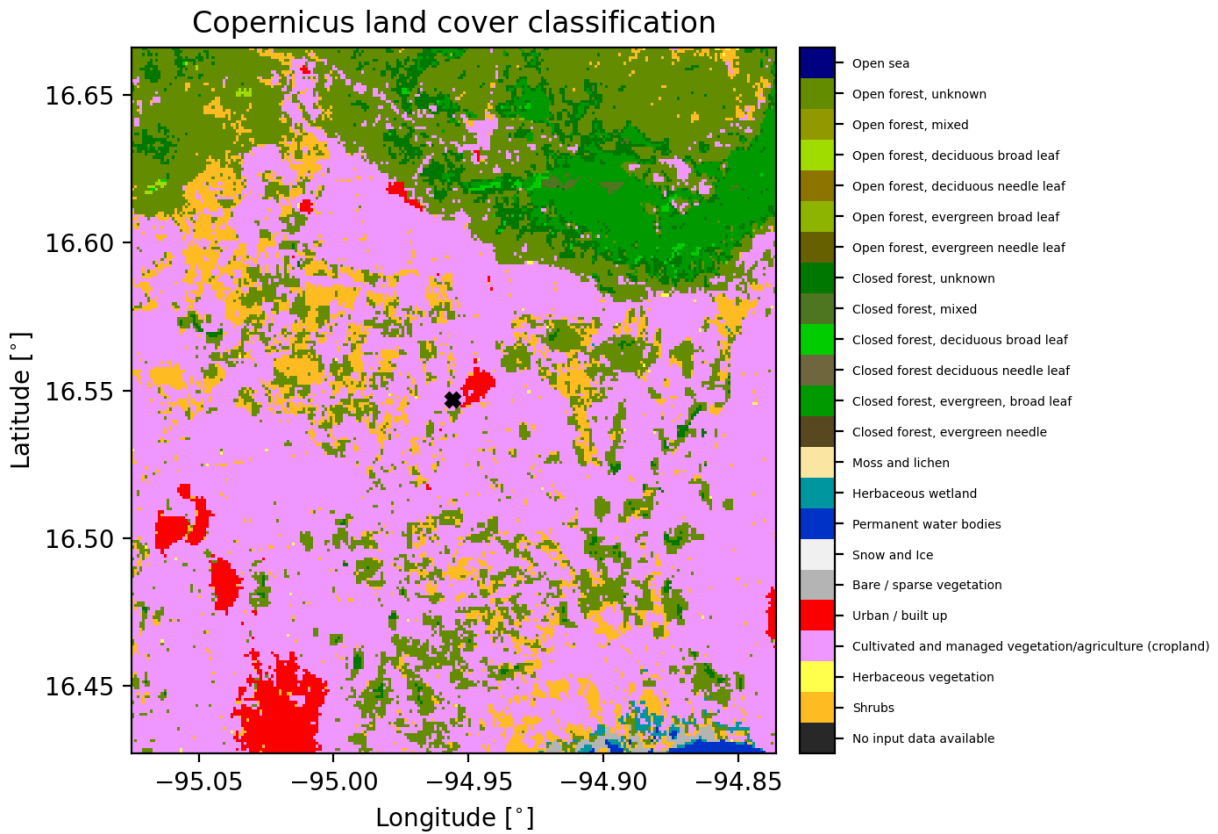


**Figure 5.28** – Copernicus land use classification for the year 2019 at mats M4.

The observed and simulated wind climate at M4 are shown in Fig. 5.30. The wind roses reveal the highly uni-directional pattern at the site, but also indicate that the models have more northerly dominated wind roses, as oppose to slightly north-westerly as seen in the observations. The observed wind speed distribution has a bi-modal shape (Fig. 5.31), associated with the annual pattern of the Tehuano wind, which peaks in late fall or winter. ERA5 significantly underestimates the wind speed at M4, while WRF and the PyWAsP downscaled results both overestimate the wind speed significantly (Fig. 5.31).

The diurnal and annual wind speed cycles (Fig. 5.32) show the strong Tehuano wind in November, December, and January. The diurnal cycle is similar to some of the other sites in that the strongest winds tend to happen in the afternoon or evening hours. The dominant annual cycle is well simulated by WRF, but the diurnal cycle is not captured to the same degree (Fig. 5.32).



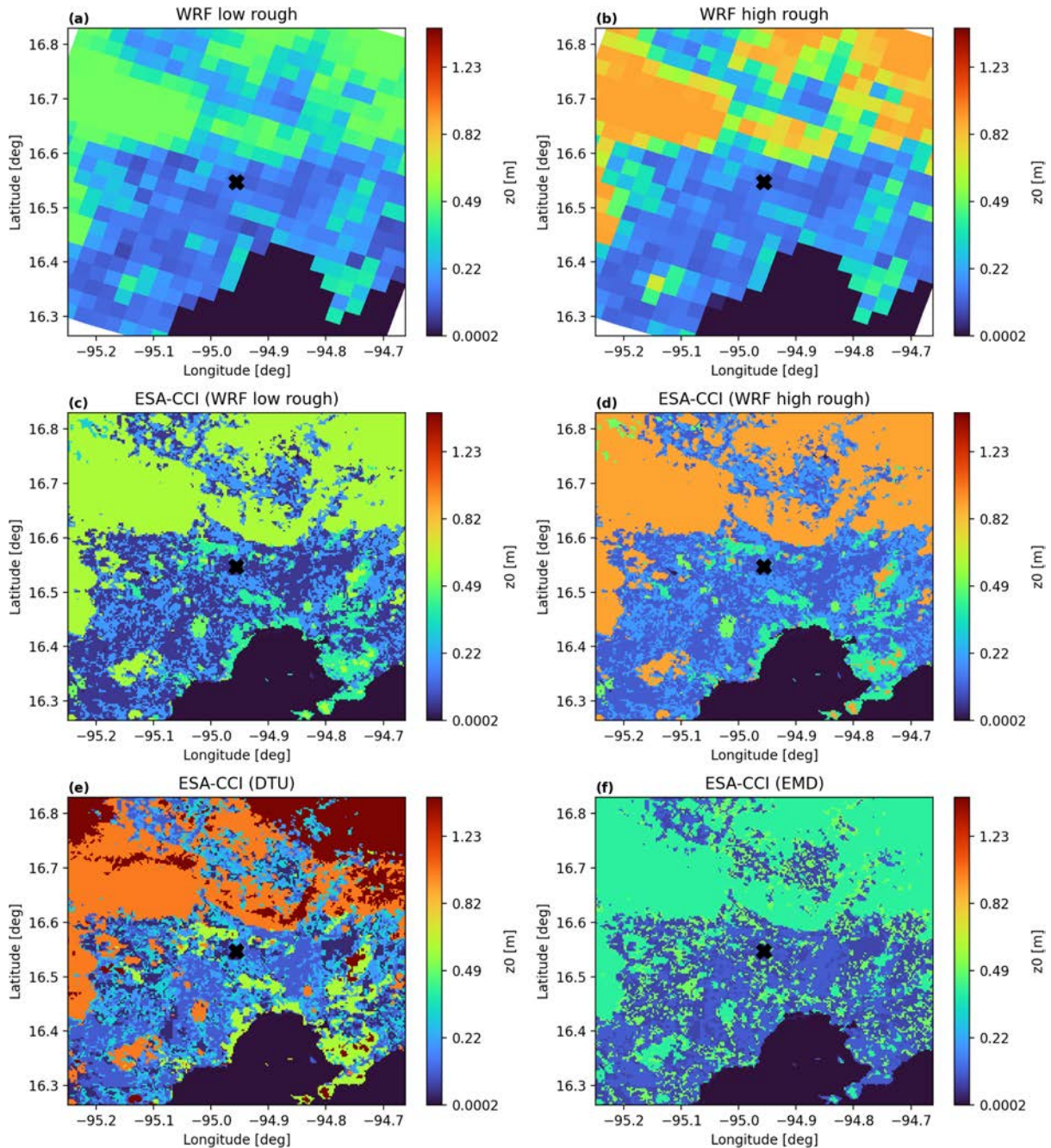


**Figure 5.29** – Roughness maps around mast M4 obtained from the WRF simulations (a), and from the high-resolution ESA-CCI land cover generated with the EMD (b), DTU (c) and WRF lookup table (d).

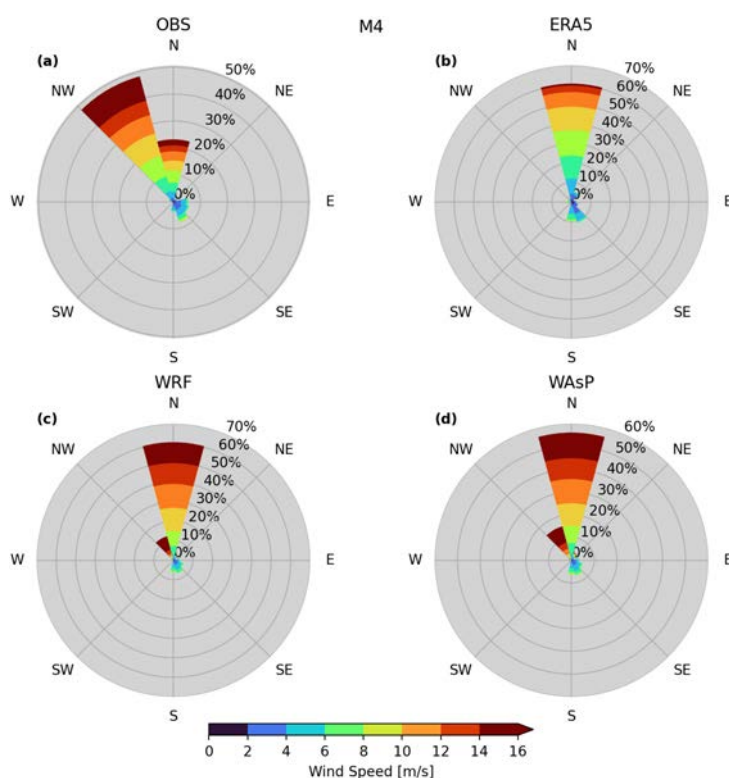


**Figure 5.30** – Observed and simulated wind climatologies at 80 m AGL at site M4 during 2018: (a) observed, (b) ERA5, (c) raw WRF production run, (d) PyWAsP downscaling.

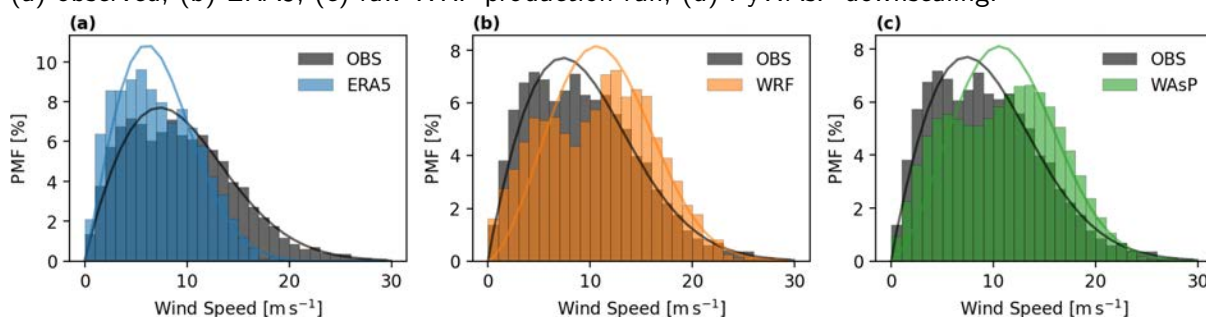


**Figure 5.31** – Observed and WRF-simulated frequency distribution of wind speed at 80 m AGL at site M4 during 2018.

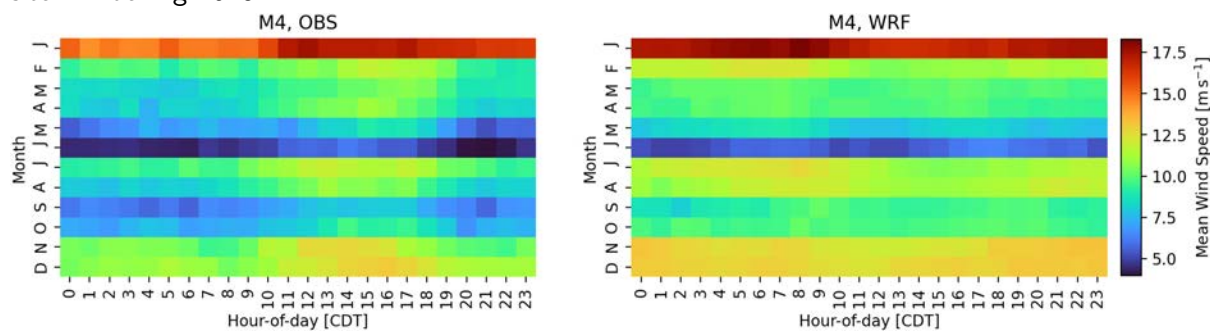


**Figure 5.32** – Observed and WRF-simulated seasonal and diurnal cycle of wind speed at 80 m AGL at site M4 during 2018. Times are in Central Daylight Time.

### 5.3.5 Ojuelos (M5)

The mast M5 is located in the central part of Mexico in the Jalisco region on top of the plateau of a larger mountain range (Fig. 5.33). The climate is subtropical highland climate and the surrounding vegetation is primarily grass- and shrubland with smaller patches of forest in-between and one larger patch of forest to the south (Fig. 5.34 and 5.35). The resulting surface roughness is of  $O(\sim 10 \text{ cm})$  from all directions, except from the south and south-east (Fig. 5.36).

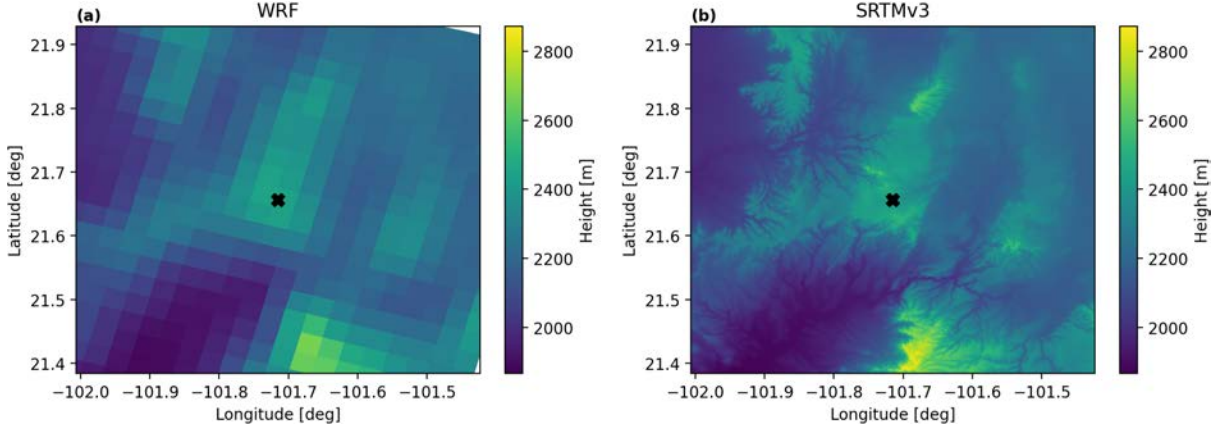


**Figure 5.33** – Surface elevation maps around mast M5 obtained from the WRF simulations (a), and from the high-resolution SRTMv3 data set (b).

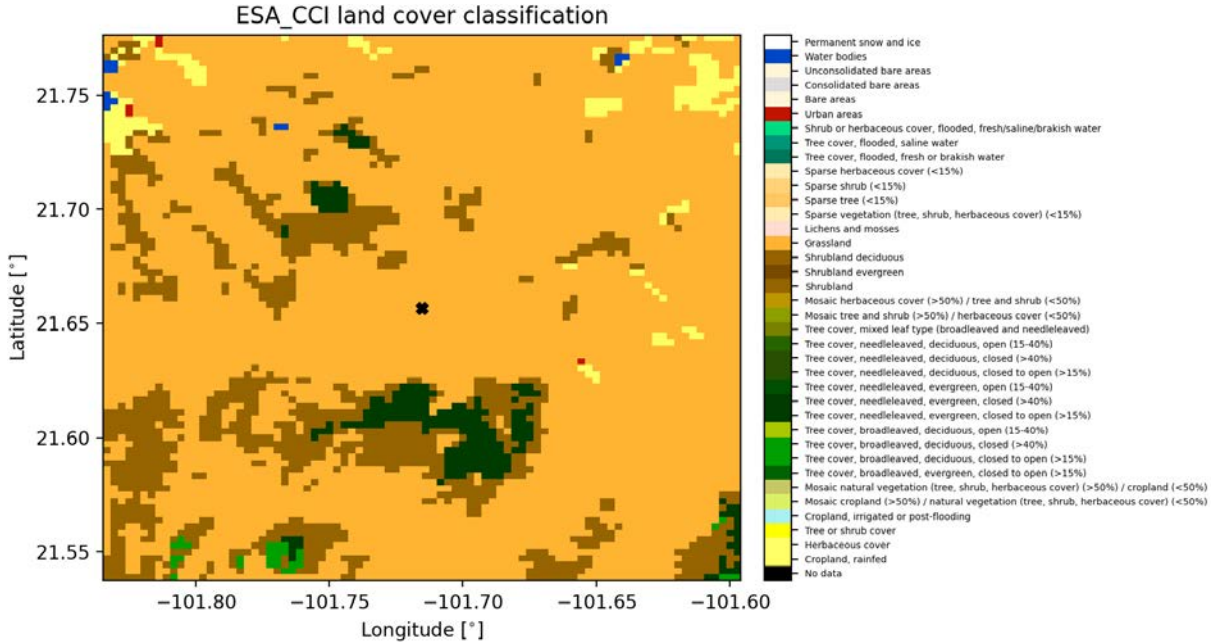


**Figure 5.34** – ESA-CCI land use classification at mats M5.

The observed and simulated wind climate at M5 are shown in Figs. 5.37 and 5.38. The models all capture the bidirectional nature of the observed wind rose well. The wind speed is



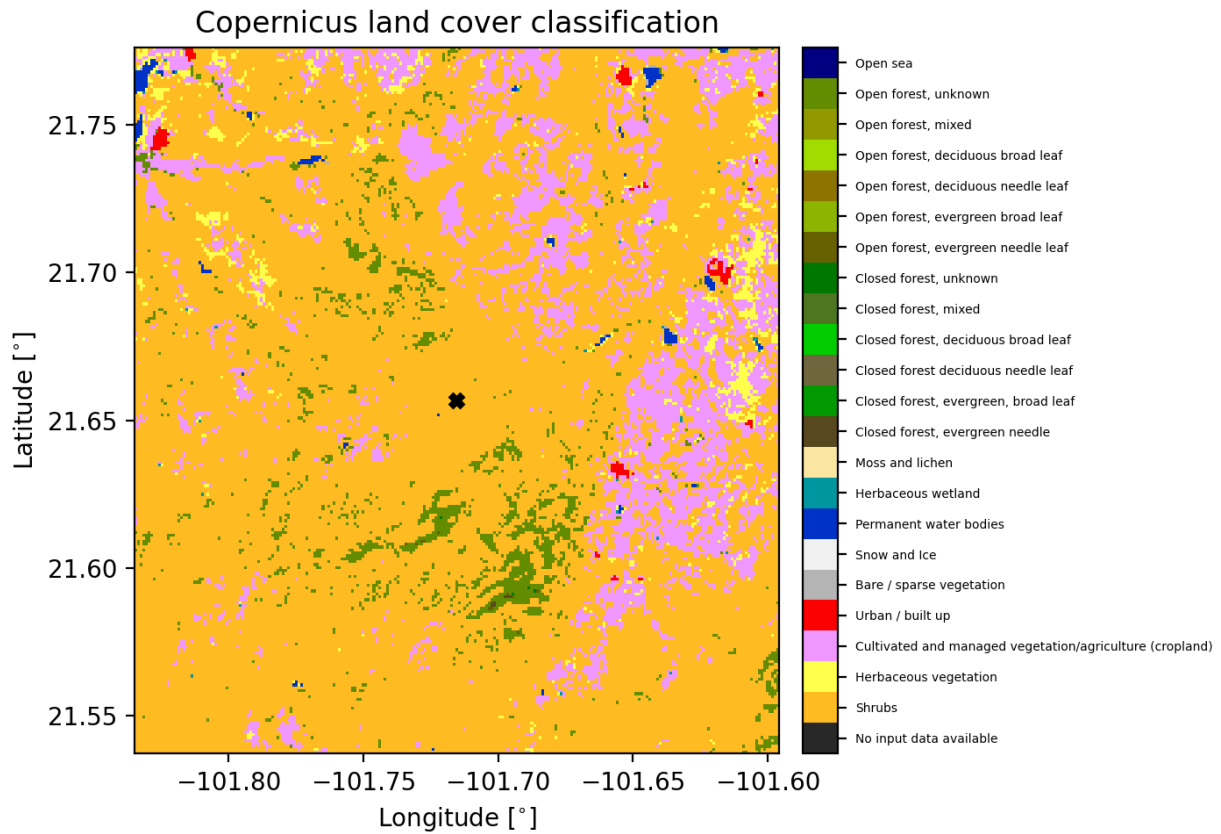


**Figure 5.35** – Copernicus land use classification for the year 2019 at mats M5.

underestimated by ERA5 and overestimated slightly by WRF. Downscaling with WAsP reduces the overestimation made by WRF.

At M5, the annual and diurnal cycles of wind speed are captured by WRF (Fig. 5.39). However, the night-time peaks and morning lows of the diurnal cycle are, respectively, over and under estimated.

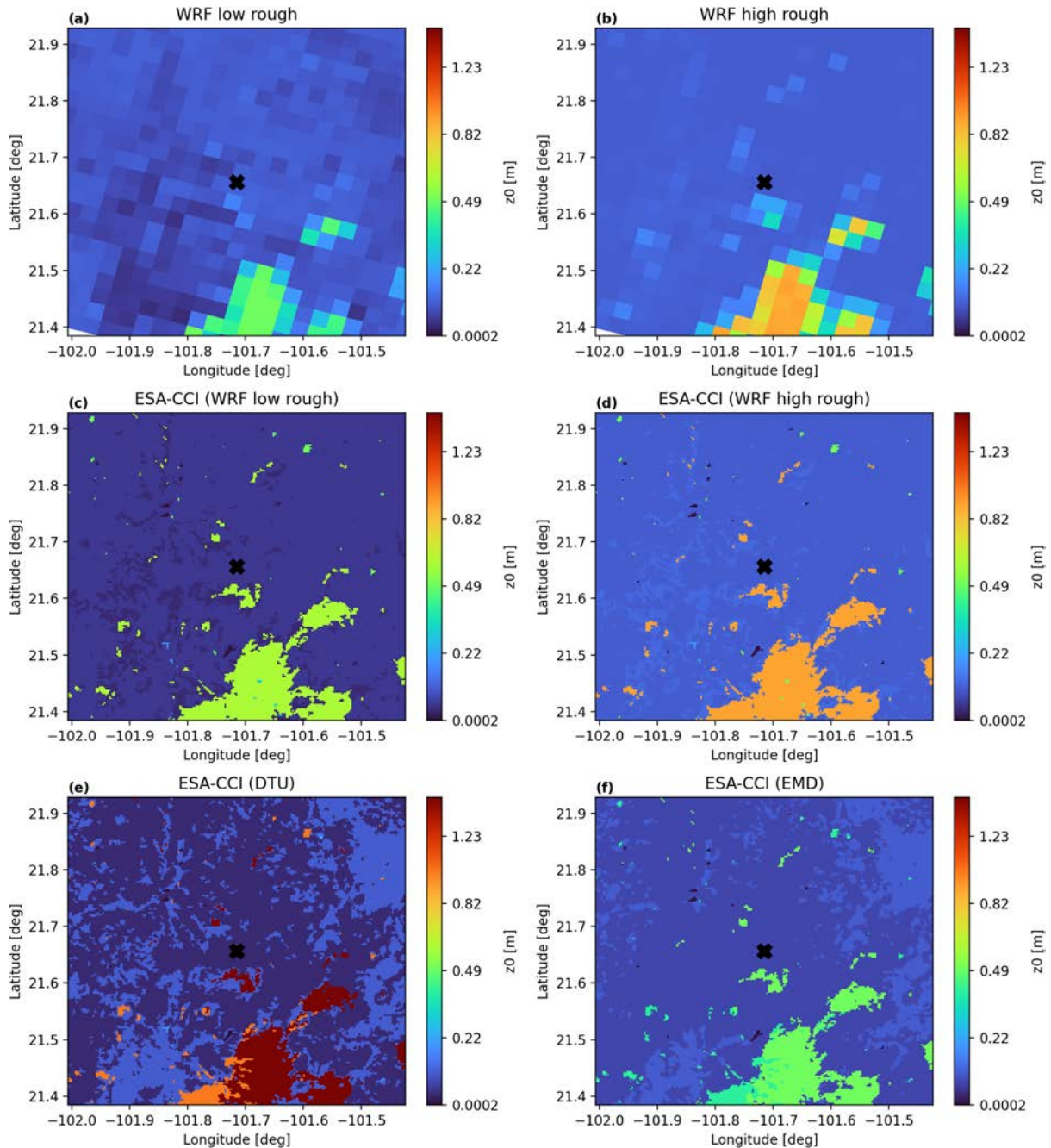


**Figure 5.36** – Roughness maps around mast M5 obtained from the WRF simulations (a), and from the high-resolution ESA-CCI land cover generated with the EMD (b), DTU (c) and WRF lookup table (d).

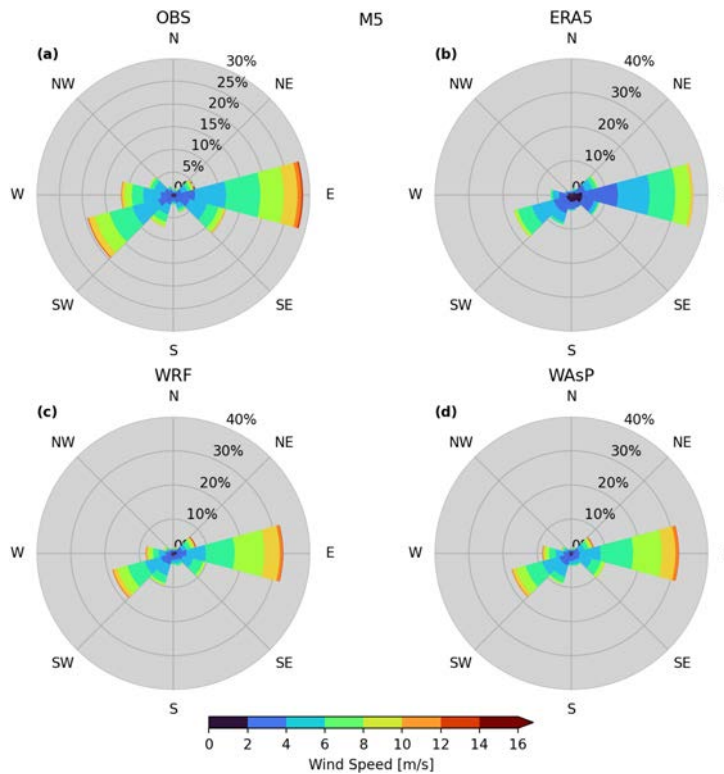


**Figure 5.37** – Observed and simulated wind climatologies at 80 m AGL at site M5 during 2018: (a) observed, (b) ERA5, (c) raw WRF production run, (d) PyWAsP downscaling.

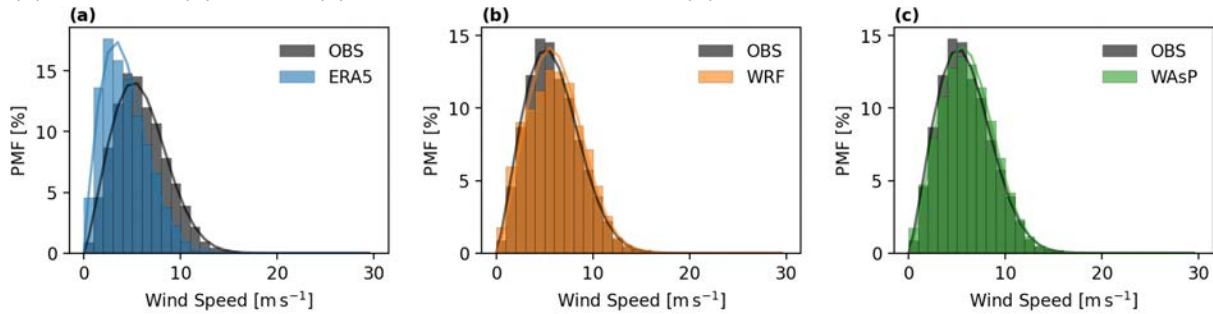


**Figure 5.38** – Observed and WRF-simulated frequency distribution of wind speed at 80 m AGL at site M5 during 2018.

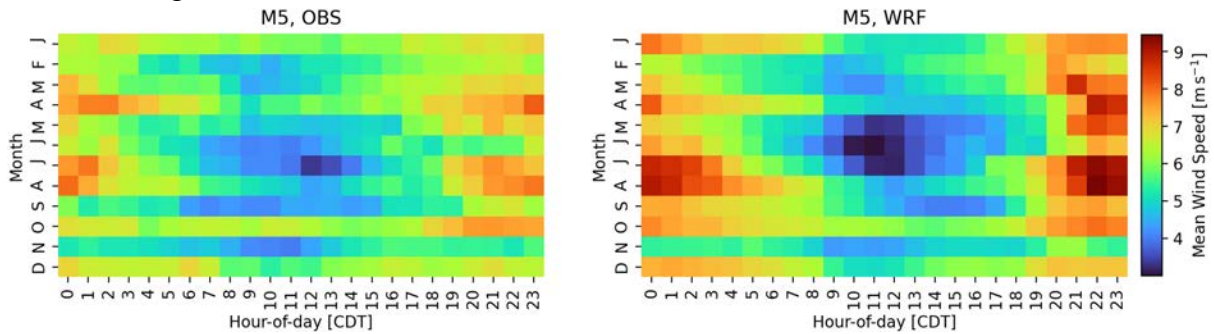


**Figure 5.39** – Observed and WRF-simulated seasonal and diurnal cycle of wind speed at 80 m AGL at site M5 during 2018. Times are in Central Daylight Time.

### 5.3.6 San Fernando (M6)

Mast M6 is located in Tamaulipas, not far from the Mexican coast along the gulf of Mexico, near the small village Gral Francisco Villa. The surrounding landscape is open and flat, but to the west the terrain slopes upwards towards some smaller hills (Fig. 5.40). The land cover is mostly cultivated land with smaller patches of urban areas, shrubland, and forests (Fig. 5.42 and 5.41), which results in surface roughness values of  $\sim 10$  cm.

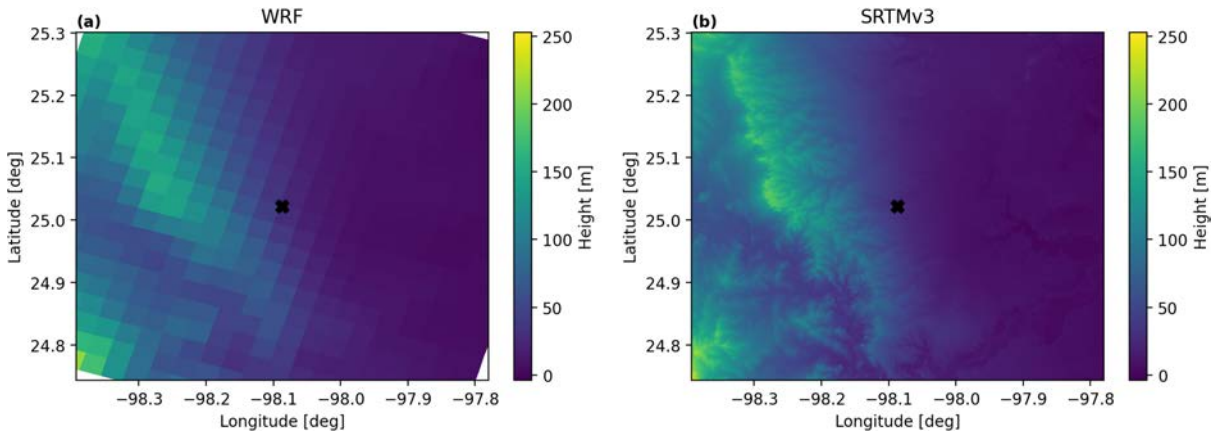


**Figure 5.40** – Surface elevation maps around mast M6 obtained from the WRF simulations (a), and from the high-resolution SRTMv3 data set (b).

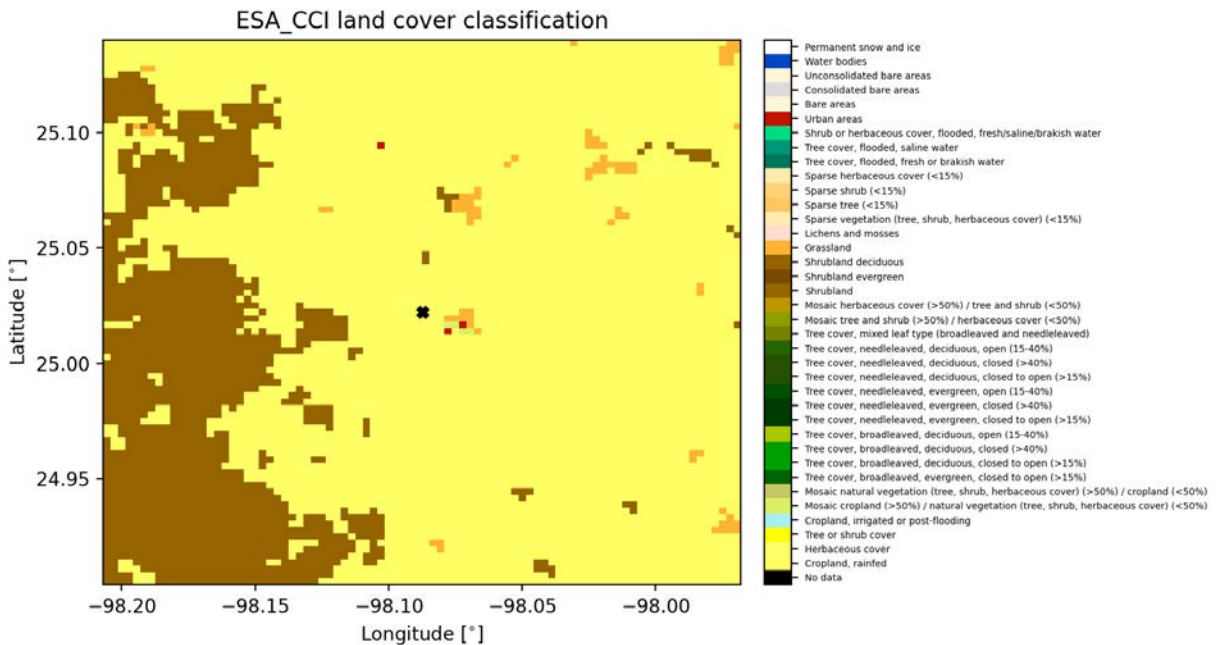


**Figure 5.41** – ESA-CCI land use classification at mats M6.

The observed and simulated wind climate at M6 are shown in Figs. 5.44 and 5.45. All three models capture both the south-easterlies dominated wind rose and the wind speed distribution well, but underestimate the tail of the wind speed distribution (strong winds). The (negative) bias of ERA5 is, however, slightly larger than for WRF and WAsP.

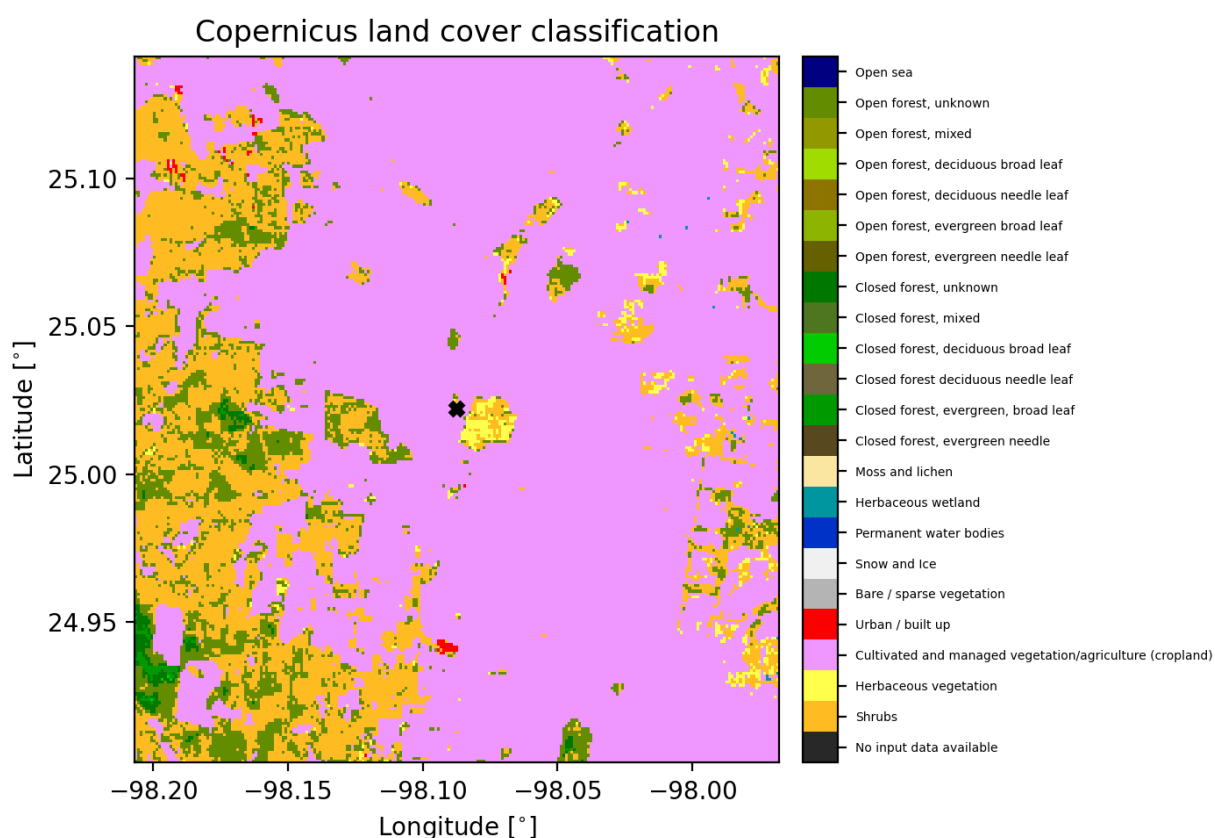


**Figure 5.42** – Copernicus land use classification for the year 2019 at mats M6.

As revealed by Fig. 5.46, the wind is strongest at M6 in the spring and summer months in particular in the evening. These annual and diurnal patterns are mostly well captured by WRF, but the afternoon peaks are underestimated.



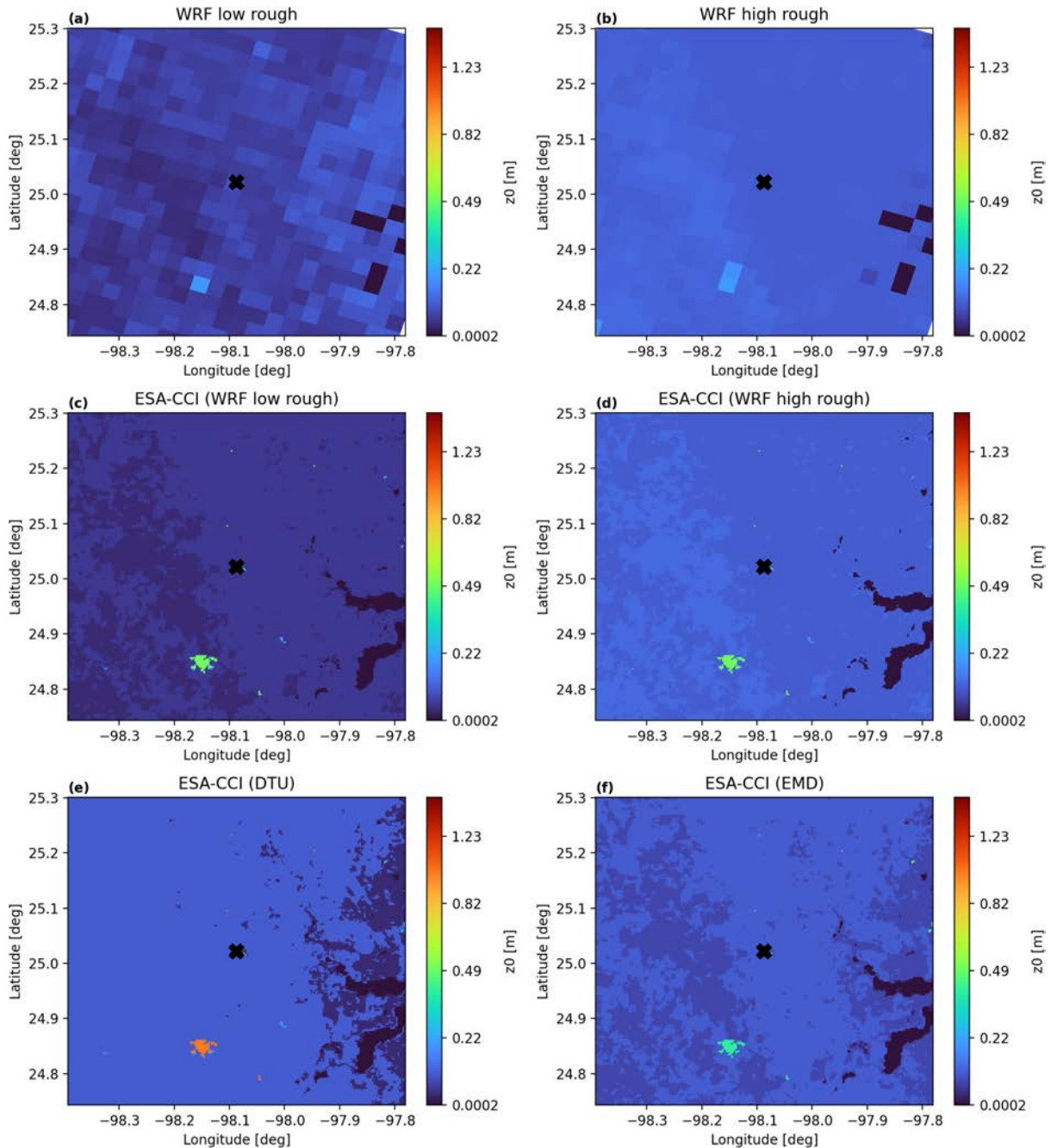


**Figure 5.43** – Roughness maps around mast M6 obtained from the WRF simulations (a), and from the high-resolution ESA-CCI land cover generated with the EMD (b), DTU (c) and WRF lookup table (d).

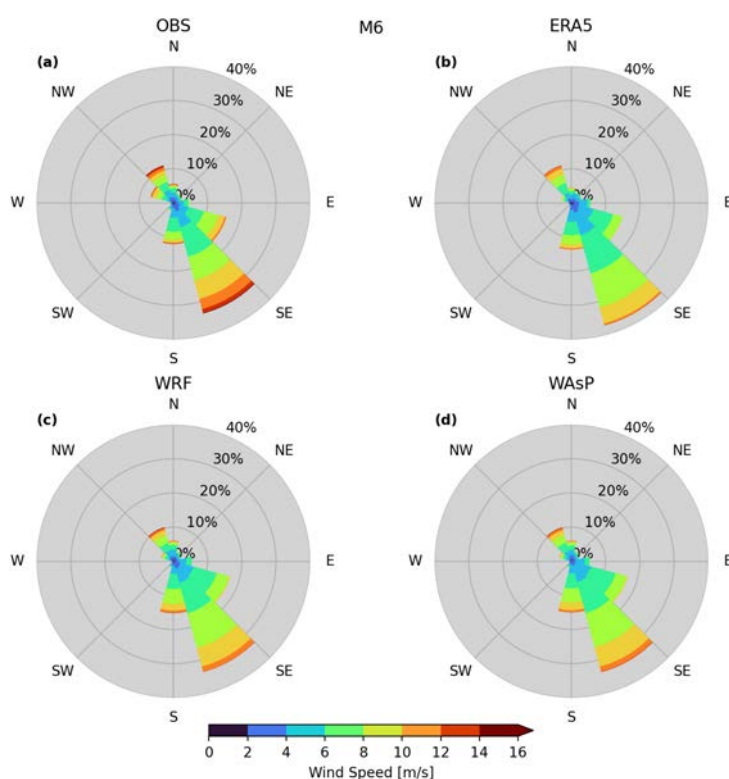


**Figure 5.44** – Observed and simulated wind climatologies at 80 m AGL at site M6 during 2018: (a) observed, (b) ERA5, (c) raw WRF production run, (d) PyWAsP downscaling.

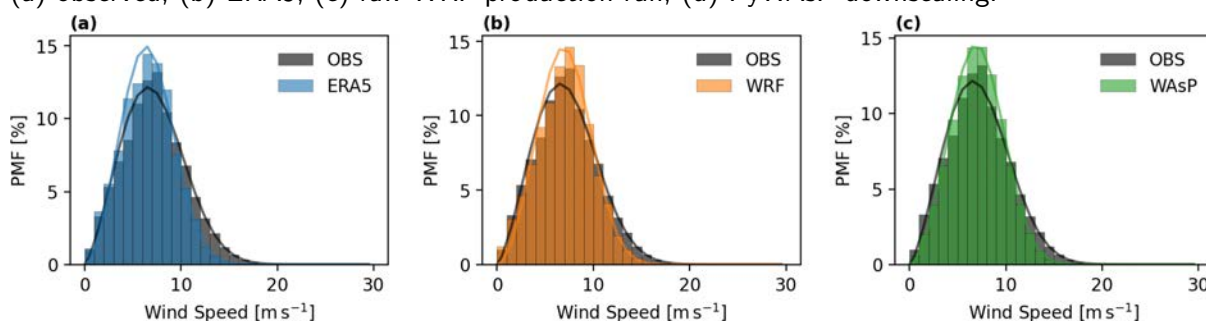


**Figure 5.45** – Observed and WRF-simulated frequency distribution of wind speed at 80 m AGL at site M6 during 2018.

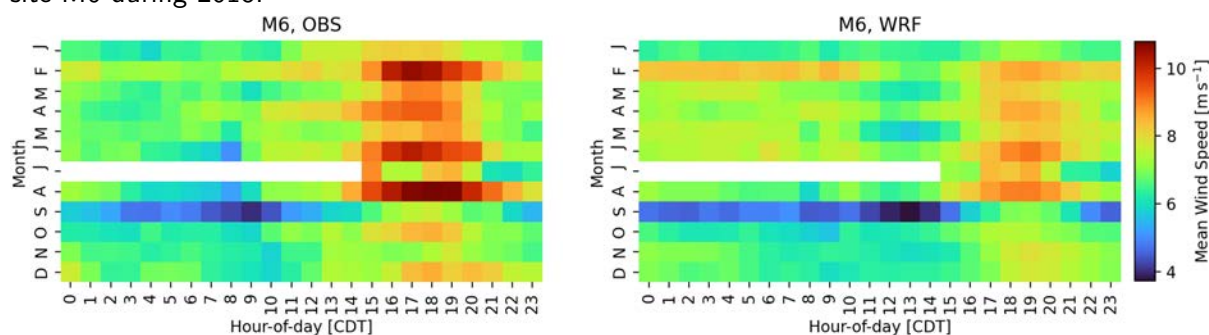


**Figure 5.46** – Observed and WRF-simulated seasonal and diurnal cycle of wind speed at 80 m AGL at site M6 during 2018. Times are in Central Daylight Time.

### 5.3.7 Tepexi (M7)

Mast M7 is located in the Puebla region of Mexico near the city of Tepexi de Rodríguez. The site sits in between the Sierra Madre Oriental and the Trans-Mexican Volcanic Belt mountain ranges and the orographic complexity at the site is therefore quite high (Fig. 5.47). The land cover in the area is dominated by shrubland, forests, and some urban areas (Figs. 5.48 and 5.49), resulting in a high degree of in-homogeneity of surface roughness (Fig. 5.50).

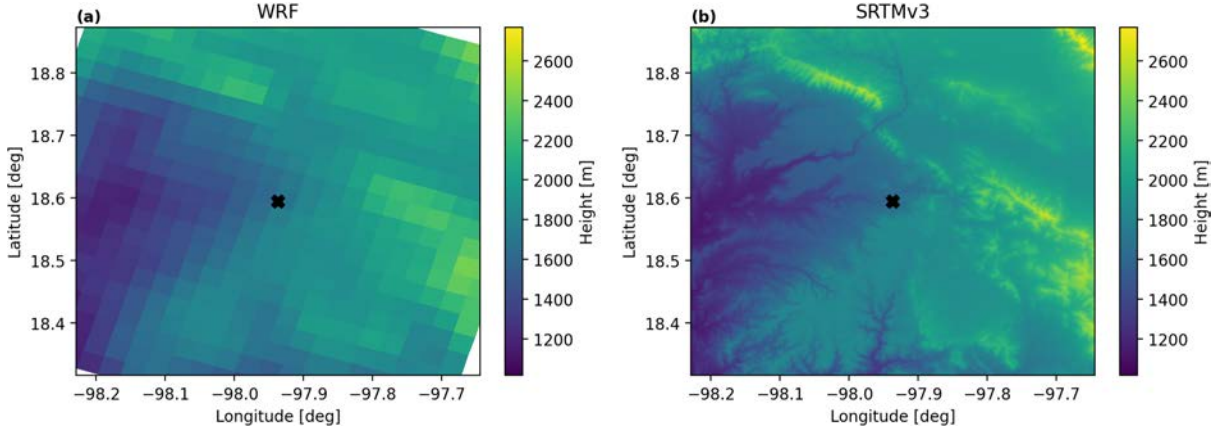


**Figure 5.47** – Surface elevation maps around mast M7 obtained from the WRF simulations (a), and from the high-resolution SRTMv3 data set (b).

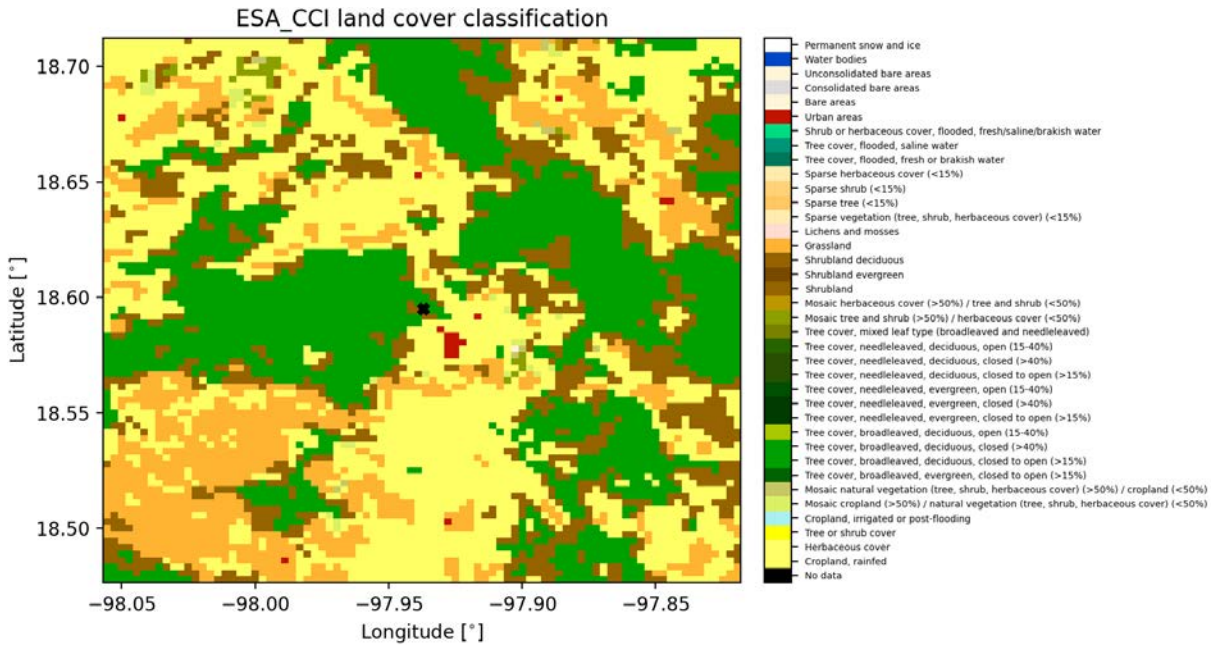


**Figure 5.48** – ESA-CCI land use classification at mast M7.

The observed and simulated wind climate at M7 are shown in Figs. 5.51 and 5.52. Compared to the measurements all of the simulations show too little south-north variation in the easterly wind components of the wind rose. The wind speed at M7 is underestimated by ERA5, while WRF and WASP overestimate it.

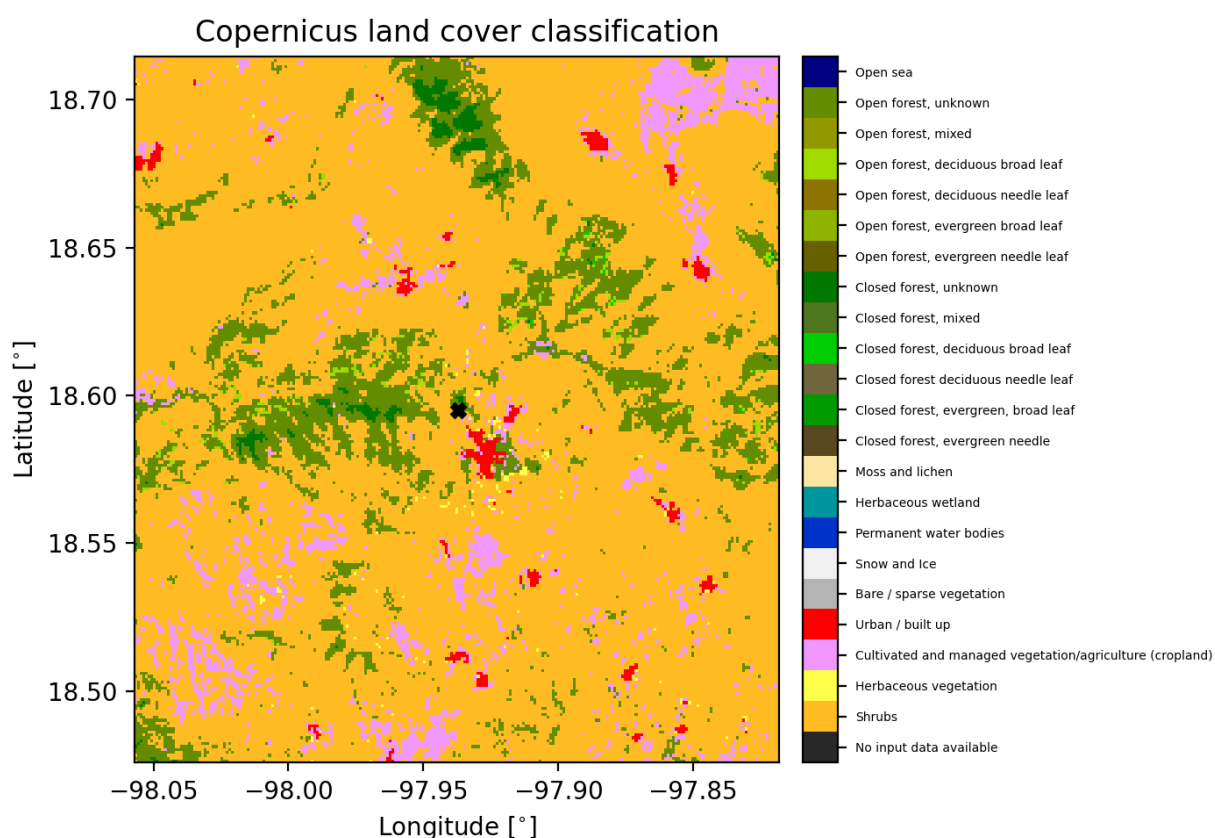


**Figure 5.49** – Copernicus land use classification for the year 2019 at mast M7.

The annual and diurnal wind speed map at M7 (Fig. 5.53) shows that the wind speed is overestimated by WRF in the evening hours and in the first part of the night. This overestimation is especially pronounced in the summer and early fall months.



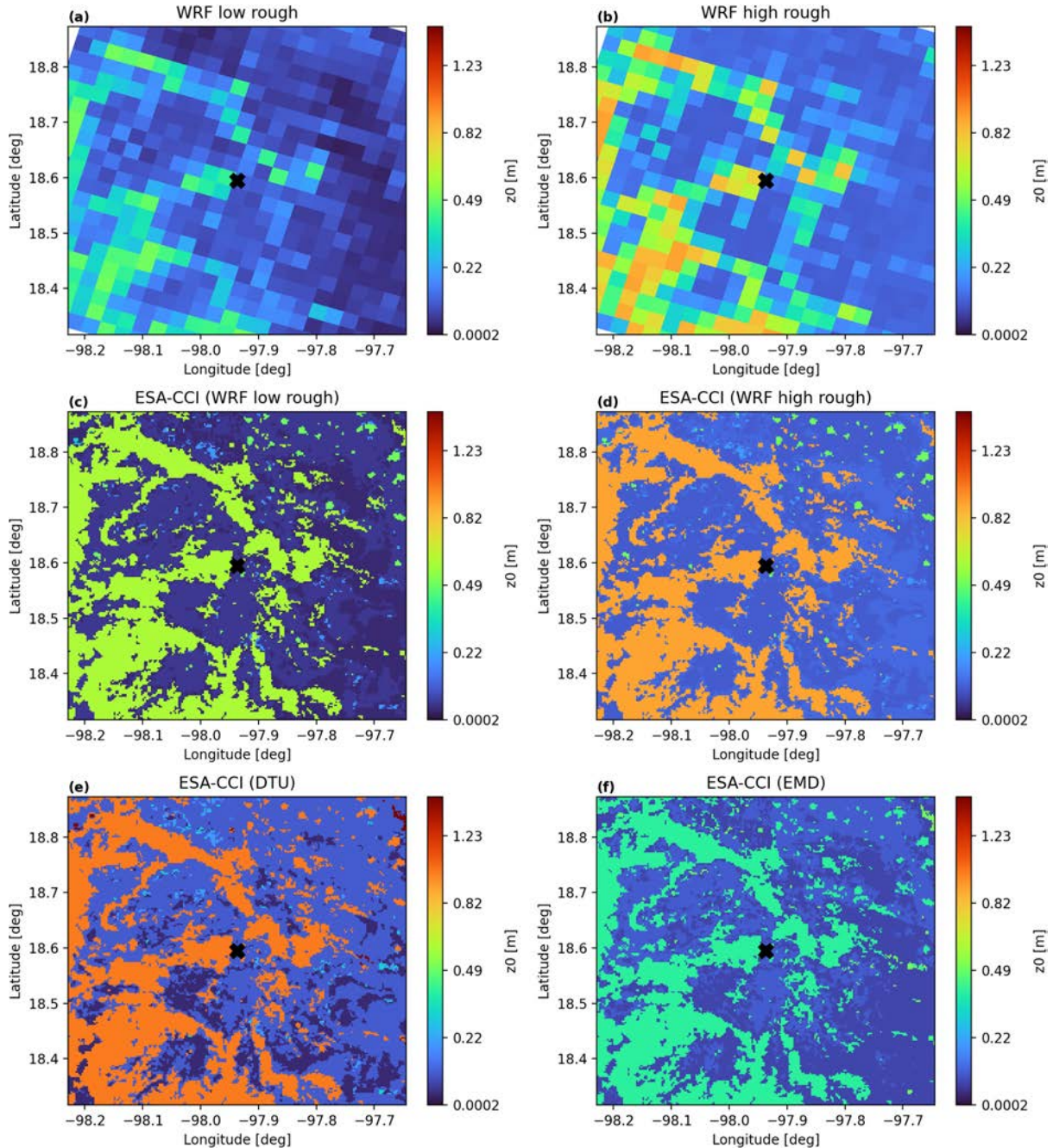


**Figure 5.50** – Roughness maps around mast M7 obtained from the WRF simulations (a), and from the high-resolution ESA-CCI land cover generated with the EMD (b), DTU (c) and WRF lookup table (d).

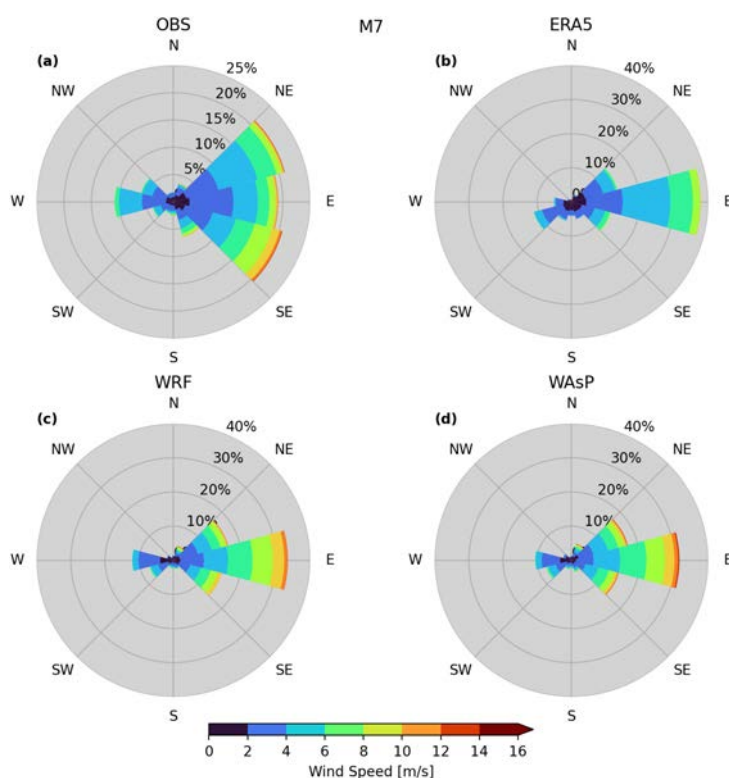


**Figure 5.51** – Observed and simulated wind climatologies at 80 m AGL at site M7 during 2018: (a) observed, (b) ERA5, (c) raw WRF production run, (d) PyWAsP downscaling.

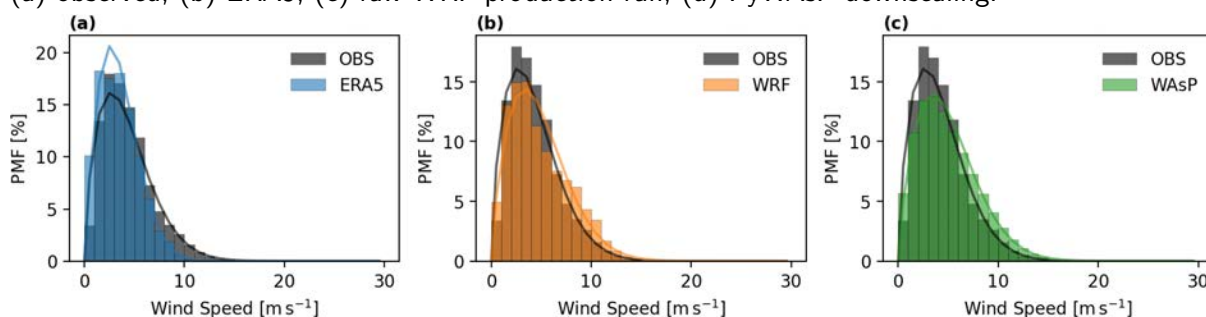


**Figure 5.52** – Observed and WRF-simulated frequency distribution of wind speed at 80 m AGL at site M7 during 2018.

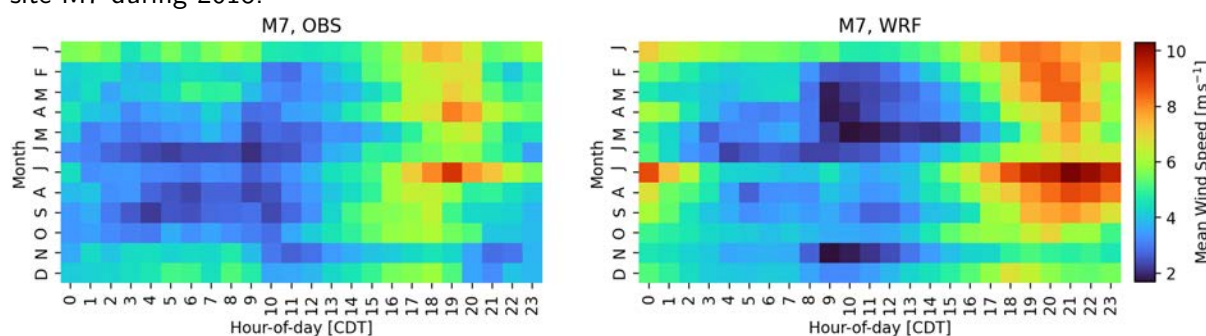


**Figure 5.53** – Observed and WRF-simulated seasonal and diurnal cycle of wind speed at 80 m AGL at site M7 during 2018. Times are in Central Daylight Time.



# Chapter 6

## Wind resource maps

### 6.1 Wind atlas resource maps

Maps of the WRF- and PyWAsP-based numerical wind atlas are now presented, with ERA5 also included for reference. Figure 6.1 shows the long-term averaged (2010–2020) wind speed at 100 m AGL derived from ERA5, the raw WRF model simulations, and the results from downscaling with PyWAsP. Figure 6.2 shows the equivalent wind power density at 100 m AGL. For ERA5 and WRF, the air density used for calculating the power density was derived from the models surface level pressure and temperature fields, while ERA5-derived variables (temperature, specific humidity, surface pressure and lapse rate) was used in PyWAsP. The grid spacing of the maps are  $0.25^\circ \times 0.25^\circ$  for ERA5,  $3 \text{ km} \times 3 \text{ km}$  for WRF, and  $0.0025^\circ \times 0.0025^\circ$  for PyWAsP. The strong gap flow, Tehuano wind, is clearly visible on all three maps just south-west of the Mexican and Guatemalan mountains. However, the magnitude and fine-scale structure is more detailed in the WRF and PyWAsP results than in those of ERA5. The maps reveal the very limited wind resources in most regions of Mexico estimated by the ERA5 model, while WRF and PyWAsP paint a more nuanced picture with many more wind resources. Viewing the large scale structures of the wind resources at the scale of the maps, the WRF and PyWAsP results seem very similar, but zooming into specific onshore regions can reveal many local variations.

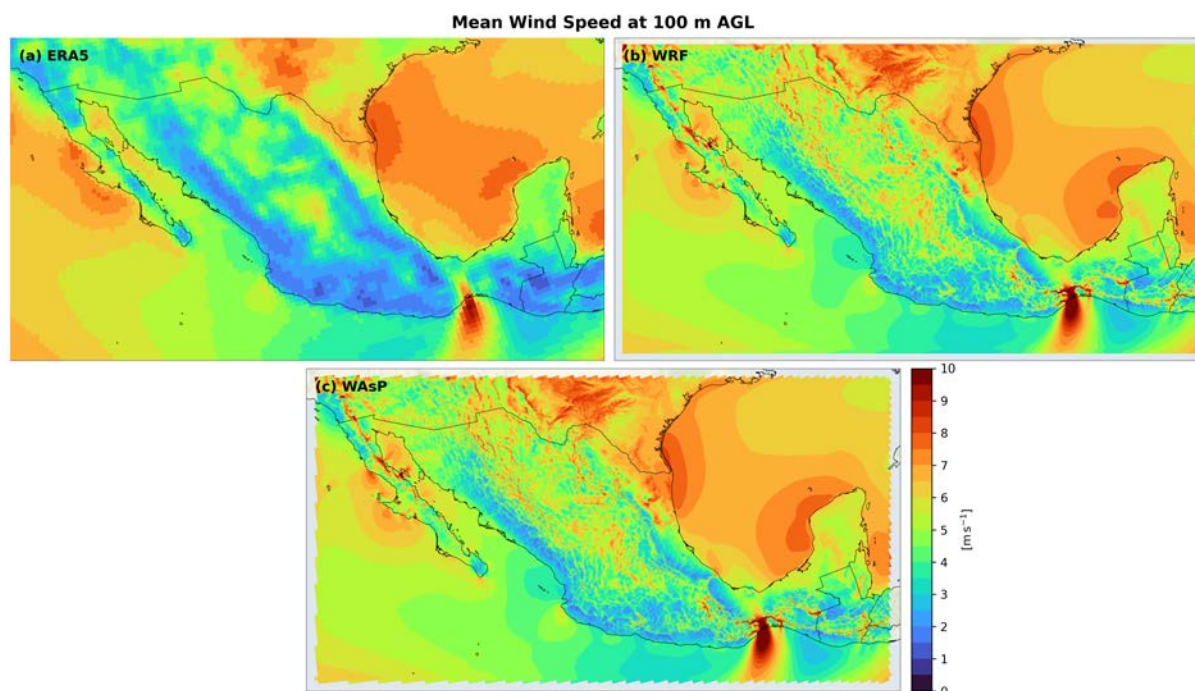


**Figure 6.1** – Long-term mean wind speed at 100 m AGL derived from ERA5, WRF, and PyWAsP.

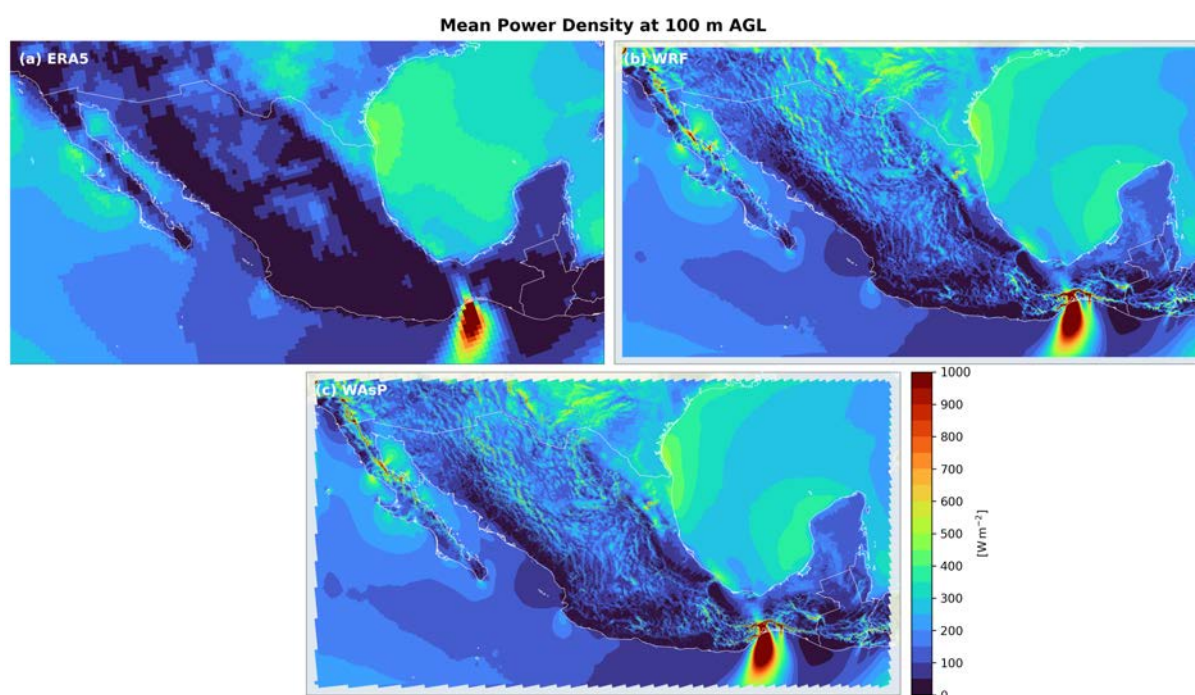


**Figure 6.2** – Long-term mean wind speed at 100 m AGL derived from (a) ERA5, (b) WRF model production run, and (c) PyWAsP.

## 6.2 Wind resources maps around M1

To illustrate the difference between the mesoscale and microscale wind resource maps, we show a closer look at the wind around the mast M1 (Figures 6.3 and 6.4), which is located at the northern end of Baja California on the border to the US. The mast is on top of a plateau with steep downwards slopes further to the east.

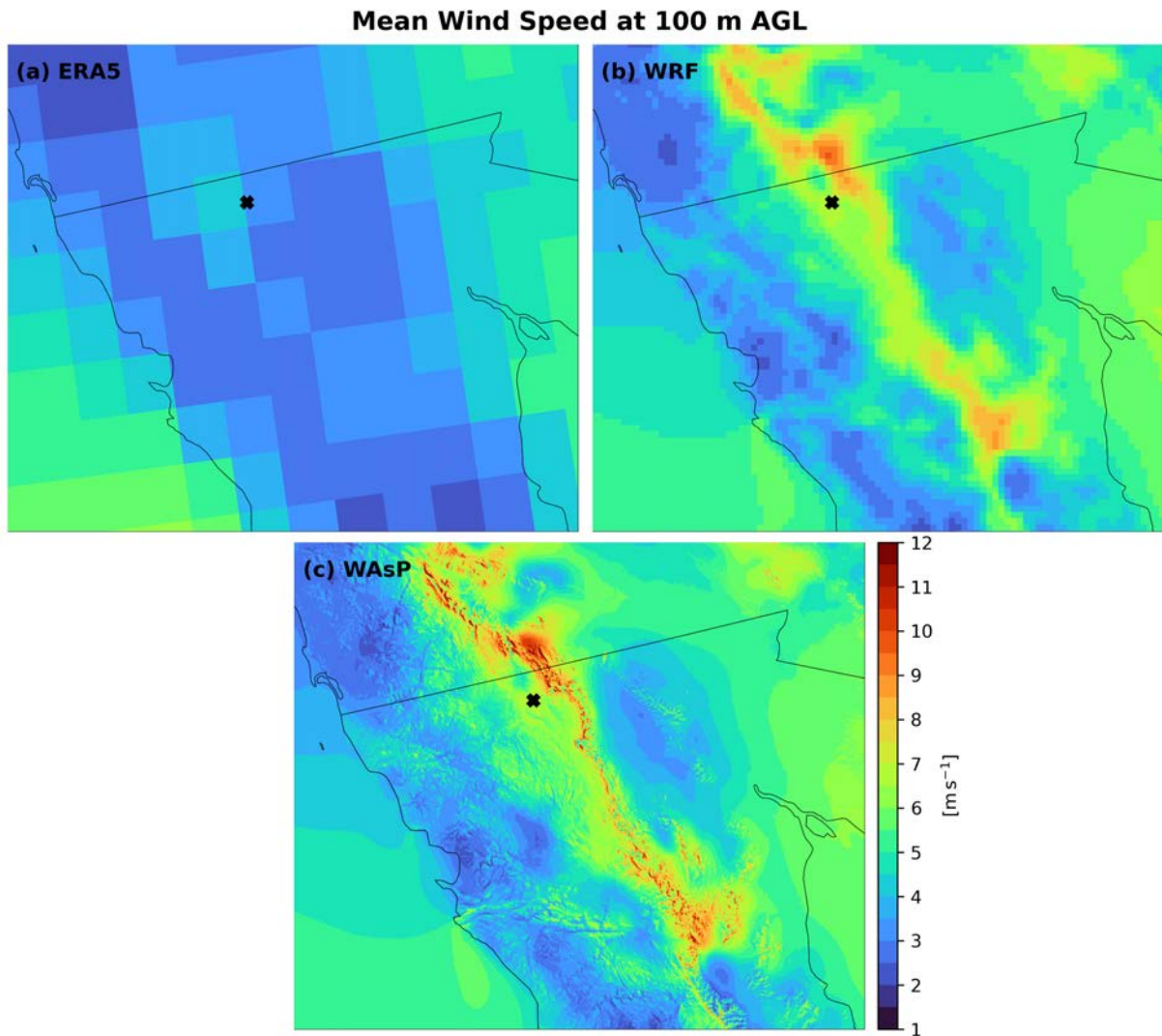


**Figure 6.3** – ERA5, WRF, and WAsP-estimated emergent wind speed at 100 m AGL around M1. The area shown is  $\approx 1^\circ$  around the site.

The figures clearly show the added details of the downscaling process from ERA5 to WRF to PyWAsP. In the ERA5 maps, the resources near M1 are low (less than  $100 \text{ W m}^{-2}$ ) and very little variation in the area is seen. Going to the WRF maps much greater variation is seen and an elongated band of high resources appear coinciding with the terrain of the Sierra de California. After downscaling with PyWAsP, effects of the high-resolution orographic and roughness features can be seen. Indeed the area with wind resources above  $1000 \text{ W m}^{-2}$  north of the border in Fig. 6.4 is where two wind farms are located.



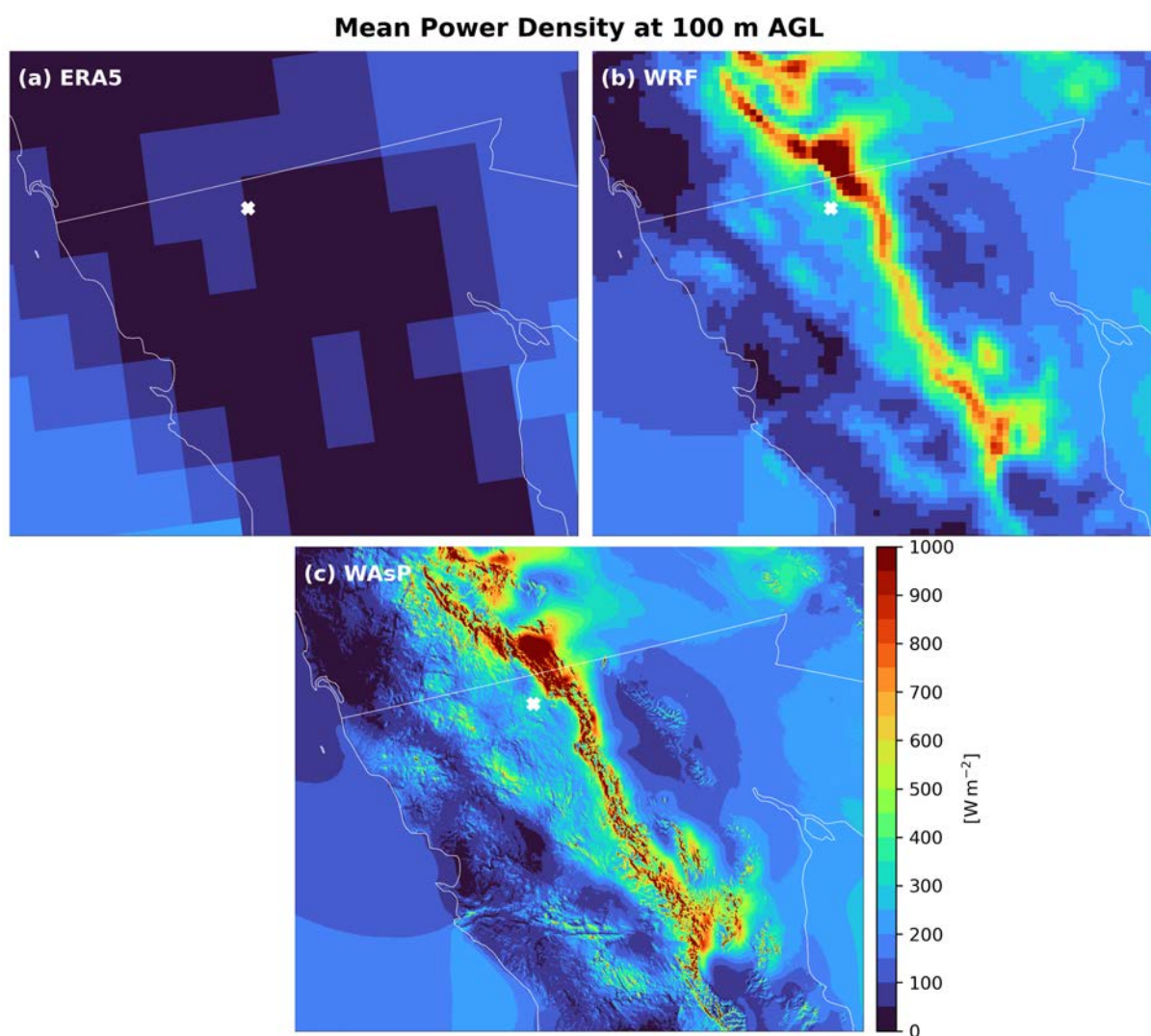


**Figure 6.4** – ERA5, WRF, and WAsP-estimated emergent wind power density at 100 m AGL around M1. The area shown is  $\approx 1^\circ$  around the site.

# Chapter 7

## Summary and conclusions

This document reports on the methods used to create and the results of the WRF- and WAsP-based numerical wind atlases developed for the Wind Atlas of Mexico (WAM) project.

Similar to the WASA3 project ([Hahmann et al., 2021](#)), the WAM production utilized several updates from the traditional configuration of numerical wind atlases documented, e.g. in [Hahmann et al. \(2018\)](#). Among the most important:

1. We ran seven one year simulations and ten 40 day simulations to identify the WRF model configuration most suited to the simulation of the wind climatology over Mexico.
2. We found that the WRF Version 4.2.1 using the MYNN scheme, and mosaic land surface parameters performed the best, both in the raw WRF output, but also in the downscaled wind climatologies.
3. We produced a high resolution (up to date) wind climatology for Mexico, 10 years (2010–2019) of simulation covering all Mexico at  $3 \text{ km} \times 3 \text{ km}$  spatial resolution and 60 min time output.
4. We used PyWAsP for both generalization of the WRF-derived wind climate and for downscaling to the microscale at  $0.0025^\circ \times 0.0025^\circ$  grid spacing.

The WRF mesoscale analysis method utilises the WRF mesoscale model to directly simulate atmospheric conditions over Mexico. Validation against measurements from 80 m AGL from six masts (leaving out one mast with complex orography,  $\text{RIX} > 2\%$ ) for the year 2018 show that the nearest WRF grid cells have a MAPE of 6.2 and 14.7% for wind speed power density. After downscaling with PyWAsP, the MAPE reduces to 5.6 and 11.7% respectively. For reference, using the raw ERA5 reanalysis dataset results in a MAPE of 24.7 and 52.8% due to large underestimations.

Many factors contribute to the uncertainty of the results. A few known sources of errors in the WRF-based wind atlas are listed below:

1. Uncertainty in the forcing reanalysis.  
Due to the sparse observing system, the ERA5 reanalysis, while of superior quality than the previously used ERA-Interim reanalysis, is expected to contain larger errors in Mexico than in Europe. These errors directly impact the quality of the WRF analyses.

2. Uncertainty in the WRF simulations:

The veracity of the WRF simulations themselves, and how these vary with the various setting in the simulations, will introduce errors in the final wind atlas. For example, as seen in the ensemble/sensitivity model results, large differences for specific sites are found. However, when the errors are averaged over all sites, the biases are much reduced.

3. Representativeness of the simulated period:

An additional error is introduced in the estimates derived from the WRF simulations because the mast measurements cover only one full year.

For the PyWAsP downscaling the main sources of uncertainty comes from accuracy of the high-resolution maps, the complexity of the terrain, the representatives of the generalization for capturing the WRF-resolved terrain effects such that the "correct" generalized wind climates are created.



## Chapter 8

# Acknowledgments

This work is a result of the joint Mexican-Danish project “Wind Atlas of Mexico” (WAM). The contribution from Denmark is financed by the Danish Ministry of Foreign Affairs through the Danish Climate Envelope.

We would also like to acknowledge the Danish Ministry of Foreign Affairs and Danida Fellowship Centre, which funded the ‘Multi-scale and model-chain Evaluation of Wind Atlases’ (MEWA) project. MEWA and WAM have been sharing synergies during the execution of both projects.

# Bibliography

- Badger, J., H. Frank, A. N. Hahmann, and G. Giebel, 2014: Wind-climate estimation based on mesoscale and microscale modeling: Statistical-dynamical downscaling for wind energy applications. *Journal of Applied Meteorology and Climatology*, **53**, 1901–1919.  
URL <http://journals.ametsoc.org/doi/abs/10.1175/JAMC-D-13-0147.1>
- Badger, J., A. Hahmann, X. G. Larsen, M. Badger, M. Kelly, N. Davis, B. T. Olsen, and N. G. Mortensen, 2015: The Global Wind Atlas. Tech. rep., DTU Wind Energy, Roskilde, Denmark.  
URL [https://www.energiteknologi.dk/sites/energiteknologi.dk/files/slutrapporter/gwa\\_64011-0347\\_finalreport.pdf](https://www.energiteknologi.dk/sites/energiteknologi.dk/files/slutrapporter/gwa_64011-0347_finalreport.pdf)
- Danielson, J. J. and D. B. Gesch, 2011: Global multi-resolution terrain elevation data 2010 (GMTED2010). Tech. Rep. 2011-1073, U.S. Geological Survey Open-File Report.
- De Ferranti, J., 2012: Viewfinder panorama DEMs.  
URL <http://viewfinderpanoramas.org/dem3.html>
- Donlon, C. J., M. Martin, J. D. Stark, J. Roberts-Jones, E. Fiedler, and W. Wimmer, 2012: The operational sea surface temperature and sea ice analysis (OSTIA). *Remote Sens. Environ.*, **116**.  
URL <https://www.sciencedirect.com/science/article/pii/S0034425711002197>
- Dörenkämper, M., B. T. Olsen, B. Witha, A. N. Hahmann, N. N. Davis, J. Barcons, Y. Ezber, E. García-Bustamante, et al., 2020: The making of the New European Wind Atlas – Part 2: Production and evaluation. *Geoscientific Model Development*, **13**, 5079–5102.  
URL <https://gmd.copernicus.org/articles/13/5079/2020/>
- Floors, R., M. Badger, I. Troen, K. Grogan, and F.-H. Permien, 2021: Satellite-based estimation of roughness lengths and displacement heights for wind resource modelling. *Wind Energy Sci.*, **submitted**.
- Floors, R. and M. Nielsen, 2019: Estimating air density using observations and re-analysis outputs for wind energy purposes. *Energies*, **12**, 2038.  
URL <https://www.mdpi.com/1996-1073/12/11/2038>
- Floors, R., A. Peña, and S.-E. Gryning, 2015: The effect of baroclinicity on the wind in the planetary boundary layer. *Q. J. R. Meteorol. Soc.*, **141**, 619–630.  
URL <http://doi.wiley.com/10.1002/qj.2386>

- Floors, R. R., I. Troen, and M. C. Kelly, 2018: Implementation of large-scale average geostrophic wind shear in WAsP12.1. Tech. rep., E-0169, DTU Wind Energy, Roskilde, Denmark.
- Hahmann, A., R. Floors, C. Lennard, D. Cavar, B. Olsen, N. Davis, N. Mortensen, and J. Hansen, 2021: Mesoscale and Microscale Downscaling for the Wind Atlas of South Africa (WASA) Project: Phase 3. Tech. Rep. E-0218, DTU Wind Energy, Denmark.
- Hahmann, A. N., A. Pian, C. Lennard, and N. G. Mortensen, 2018: Mesoscale modelling for the Wind Atlas of South Africa (WASA) Project – Phase II. Tech. rep., E-0188, DTU Wind Energy, Denmark.  
URL [https://orbit.dtu.dk/files/192964222/DTU\\_Wind\\_Energy\\_E\\_0188.pdf](https://orbit.dtu.dk/files/192964222/DTU_Wind_Energy_E_0188.pdf)
- Hahmann, A. N., T. Sīle, B. Witha, N. N. Davis, M. Dörenkämper, Y. Ezber, E. García-Bustamante, J. F. González-Rouco, et al., 2020: The making of the New European Wind Atlas – Part 1: Model sensitivity. *Geoscientific Model Development* (5.154), **13**, 5053–5078.  
URL <https://gmd.copernicus.org/articles/13/5053/2020/>
- Hahmann, A. N., C. L. Vincent, A. Peña, J. Lange, and C. B. Hasager, 2015: Wind climate estimation using WRF model output: Method and model sensitivities over the sea. *International Journal of Climatology*, **35**, 3422–3439.
- Hersbach, H., B. Bell, P. Berrisford, S. Hirahara, A. Horányi, J. Muñoz-Sabater, J. Nicolas, C. Peubey, et al., 2020: The ERA5 global reanalysis. *Q. J. R. Meteorolog. Soc.*, **2020**, 1–51.  
URL <https://rmets.onlinelibrary.wiley.com/doi/full/10.1002/qj.3803>
- Hong, S.-Y., J. Dudhia, and S.-H. Chen, 2004: A revised approach to ice microphysical processes for the bulk parameterization of clouds and precipitation. *Mon. Wea. Rev.*, **132**, 103–120.
- Hong, S.-Y., Y. Noh, and J. Dudhia, 2006: A new vertical diffusion package with an explicit treatment of entrainment processes. *Mon. Wea. Rev.*, **134**, 2318–2341.
- Janjic, Z. I. and I. Zavisla, 1994: The step–mountain eta coordinate model: Further developments of the convection, viscous sublayer, and turbulence closure schemes. *Mon. Wea. Rev.*, **122**, 927–945.
- Jiménez, P. A., J. Dudhia, J. F. Gonzalez-Rouco, J. Navarro, J. P. Montavez, and E. Garcia-Bustamante, 2012: A revised scheme for the WRF surface layer formulation. *Mon. Wea. Rev.*, **140**, 898–918.
- Kain, J. S., 2004: The Kain–Fritsch convective parameterization: An update. *J. Appl. Meteor. Clim.*, **43**, 170–181.
- Lennard, C., A. N. Hahmann, J. Badger, N. G. Mortensen, and B. Argent, 2015: Development of a Numerical Wind Atlas for South Africa. *Energy Procedia*, vol. 76, Elsevier Ltd.

- Li, D., E. Bou-Zeid, M. Barlage, F. Chen, and J. A. Smith, 2013: Development and evaluation of a mosaic approach in the WRF-Noah framework. *J. Geophys. Res.*, **118**, 11,918–11,935.
- Lupu, N., L. Selios, Z. Warner, et al., 2017: A new measure of congruence: The earth mover's distance. *Political Analysis*, **25**, 95–113.
- Mellor, G. L. and T. Yamada, 1982: Development of a turbulence closure model for geophysical fluid problems. *Rev. Geophys. and Space Phys.*, **20**, 851–875.
- Mortensen, N. G., A. J. Bowen, and I. Antoniou, 2006: Improving wasp predictions in (too) complex terrain. *2006 European Wind Energy Conference and Exhibition*, European Wind Energy Association (EWEA).
- Nakanishi, M. and H. Niino, 2009: Development of an improved turbulence closure model for the atmospheric boundary layer. *J. Meteor. Soc. Japan*, **87**, 895–912.
- Nawri, N., G. N. Petersen, H. Bjornsson, A. N. Hahmann, K. Jónasson, C. B. Hasager, and N.-E. Clausen, 2014: The wind energy potential of Iceland. *Renewable Energy*, **69**, 290–299.  
URL <http://linkinghub.elsevier.com/retrieve/pii/S0960148114002043>
- Pele, O. and M. Werman, 2008: A linear time histogram metric for improved sift matching. *Computer Vision–ECCV 2008*, Springer.
- Poulter, B., N. MacBean, A. Hartley, and coauthors, 2015: Plant functional type classification for earth system models: results from the European Space Agency's Land Cover Climate Change Initiative. *Geosci. Model Dev.*, **8**, 2315–2328.
- Rabin, J., J. Delon, and Y. Gousseau, 2008: Circular Earth Mover's Distance for the comparison of local features. *2008 19th Int. Conf. Pattern Recognit.*, IEEE.
- Rubner, Y., C. Tomasi, and L. J. Guibas, 2000: The Earth Mover's Distance as a metric for image retrieval. *International Journal of Computer Vision*, **40**, 99–121.  
URL <https://doi.org/10.1023/A:1026543900054>
- Santos-Alamillos, F., D. Pozo-Vázquez, J. Ruiz-Arias, and J. Tovar-Pescador, 2015: Influence of land-use misrepresentation on the accuracy of WRF wind estimates: Evaluation of GLCC and CORINE land-use maps in southern Spain. *Atmos. Res.*, **157**, 17–28.
- Skamarock, W. C., J. B. Klemp, J. Dudhia, D. O. Gill, D. M. Barker, M. G. Duda, X.-Y. Huang, W. Wang, et al., 2008: A Description of the Advanced Research WRF Version 3. Tech. Rep. NCAR/TN-475+STR, National Center for Atmospheric Research.
- Tammelin, B., T. Vihma, E. Atlaskin, J. Badger, C. Fortelius, H. Gregow, M. Horttanainen, R. Hyvönen, et al., 2012: Production of the Finnish Wind Atlas. *Wind Energy*, n/a–n/a.  
URL <http://dx.doi.org/10.1002/we.517>
- Tewari, M., F. Chen, W. Wang, J. Dudhia, M. A. LeMone, K. Mitchell, M. Ek, G. Gayno, et al., 2004: Implementation and verification of the unified Noah land surface model in the WRF model. *20th conference on weather analysis and forecasting/16th conference on numerical weather prediction*, Seattle, 12–16 January 2004, AMS.

Thøgersen, M., 2020: EMD wiki.

URL [https://help.emd.dk/mediawiki/index.php?title=Glob\\_Cover](https://help.emd.dk/mediawiki/index.php?title=Glob_Cover)

Troen, I. and E. L. Petersen, 1989: *European Wind Atlas*. Published for the Commission of the European Communities, Directorate-General for Science, Research, and Development, Brussels, Belgium by Risø National Laboratory.

Vincent, C. L. and A. N. Hahmann, 2015: The impact of grid and spectral nudging on the variance of the near-surface wind speed. *J. Appl. Meteor. Clim.*, **54**, 1021–1038.

von Storch, H. and F. Zwiers, 1999: *Statistical Analysis in Climate Research*. Cambridge University Press.

Wang, W., J. Dudhia, and M. Chen, 2019: *Application of WRF - How to get better performance*. National Center for Atmospheric Research, Boulder, CO, USA.

URL [http://www2.mmm.ucar.edu/wrf/users/tutorial/201901/chen\\_best\\_practices.pdf](http://www2.mmm.ucar.edu/wrf/users/tutorial/201901/chen_best_practices.pdf)



# Appendix A

## WRF namelists

### A.1 WPS namelist

```
&share
wrf_core = 'ARW',
max_dom = 2,
start_date = 2*'START_DATE',
end_date   = 2*'END_DATE',
interval_seconds = 21600,
io_form_geogrid = 2,
debug_level = 0,
/

&geogrid
parent_id      = 1, 1,
parent_grid_ratio = 1, 3,
i_parent_start  = 1, 80,
j_parent_start  = 1, 80,
e_we           = 550, 1165,
e_sn           = 370, 625,
dx = 9000,
dy = 9000,
map_proj = 'lambert',
ref_lat  = 24,
ref_lon  = -102,
truelat1 = 20.0,
truelat2 = 40.0,
stand_lon = -132,
geog_data_res = 3*'esa_cci+gmted2010_30s+10m+default'
/

&ungrib
out_format = 'WPS',
prefix     = 'FIELD',
```

```

/

&metgrid
  fg_name = 'FIELD','SST'
  constants_name = 'TAVGSFC',
  io_form_metgrid = 2,
/

```

## A.2 WRF namelist

```

&time_control
  interval_seconds      = 21600,
  input_from_file      = 2*T,
  history_interval     = 2*60,
  frames_per_outfile   = 2*24,
  restart              = F,
  restart_interval     = 100000,
  io_form_history      = 2
  io_form_restart      = 2
  io_form_input        = 2
  io_form_boundary     = 2
  auxinput4_inname     = "wrflowinp_d<domain>",
  auxinput4_interval   = 2*360,
  io_form_auxinput4    = 2,
  iofields_filename    = 2*"WAFields.txt",
  ignore_iofields_warning = T,
  debug_level          = 0,
/

```

```

&domains
  max_dom              = 2,
  time_step            = 72,
  use_adaptive_time_step = T,
  step_to_output_time  = T,
  adaptation_domain    = 1,
  target_cfl           = 2*0.64,
  target_hcfl          = 2*0.64,
  max_step_increase_pct = 5, 51,
  starting_time_step   = 54, 18,
  max_time_step        = 72, 24,
  min_time_step        = 18, 6,
  grid_id              = 1, 2,
  parent_id            = 1, 1,
  parent_grid_ratio    = 1, 3,
  i_parent_start       = 1, 80,

```

```

j_parent_start      = 1, 80,
s_sn                = 2*1,
e_we                = 550,1165,
s_we                = 2*1,
e_sn                = 370, 625,
s_vert              = 2*1,
e_vert              = 2*61,
num_metgrid_levels  = 33,
num_metgrid_soil_levels = 4,
dx                  = 9000.,3000.,
dy                  = 9000.,3000.,
p_top_requested     = 5000,
max_dz              = 500.      ! maximum level thickness allowed (m)
auto_levels_opt     = 2        ! new default (also set dzstretch_s, dzstretch_u
dzbot               = 30.      ! thickness of lowest layer (m) for auto_levels_
dzstretch_s         = 1.3      ! surface stretch factor for auto_levels_opt=2
dzstretch_u         = 1.1      ! upper stretch factor for auto_levels_opt=2
smooth_option = 2,
feedback = 0,
/

&physics
mp_physics          = 2*4,
ra_lw_physics       = 2*4,
ra_sw_physics       = 2*4,
radt                = 2*12,
swint_opt           = 1,
sf_surface_physics  = 2*2,
sf_surface_mosaic   = 1,
mosaic_cat          = 3,
sf_sfclay_physics  = 2*2,
bl_pbl_physics      = 2*5,
bl_mynn_mixlength   = 0,
bldt                = 2*0,
cu_physics          = 1,0,
cudt                = 2*5,
isfflx              = 1,
icloud              = 1,
surface_input_source = 1,
num_land_cat        = 28,
num_soil_layers     = 4,
sst_update          = 1,
ensdim              = 144,
prec_acc_dt         = 2*60,
/

```

```

&fdda
  grid_fdda           = 2, 0,
  gfdda_inname        = "wrffdda_d<domain>",
  gfdda_end_h         = 360, 0,
  gfdda_interval_m    = 360, 0,
  fgdt                = 2*0,
  if_no_pbl_nudging_uv = 2*0,
  if_no_pbl_nudging_t = 1, 0,
  if_no_pbl_nudging_q = 1, 0,
  if_zfac_uv          = 1, 0,
  k_zfac_uv           = 20, 0,
  if_zfac_t           = 1, 0,
  k_zfac_t            = 20, 0,
  if_zfac_q           = 1, 0,
  k_zfac_q            = 20, 0,
  guv                 = 2*0.0003,
  gt                  = 2*0.0003,
  gq                  = 2*0.0003,
  xwavenum            = 18,
  ywavenum            = 12,
  if_ramping          = 0,
  dtramp_min          = 60.0,
  io_form_gfdda       = 2,
/

&dynamics
  w_damping           = 1,
  diff_opt            = 2,
  km_opt              = 4,
  diff_6th_opt        = 2*2,
  diff_6th_factor     = 0.06, 0.08, 0.08,
  damp_opt            = 3,
  zdamp               = 2*5000.,
  dampcoef            = 2*0.15,
  khdif               = 2*0,
  kvdif               = 2*0,
  non_hydrostatic     = 2*T,
  moist_adv_opt       = 2*1,
  scalar_adv_opt      = 2*1,
  gwd_opt             = 2*0,
/

&bdy_control
  spec_bdy_width      = 10,
  spec_zone           = 1,
  relax_zone          = 9,
  spec_exp            = 0.33,

```

```
specified          = T, F,  
nested            = F, T,  
/  
&grib2  
/  
&namelist_quilt  
  nio_tasks_per_group = 8,  
  nio_groups = 3,  
/
```



## Appendix B

### Google Earth images at each site

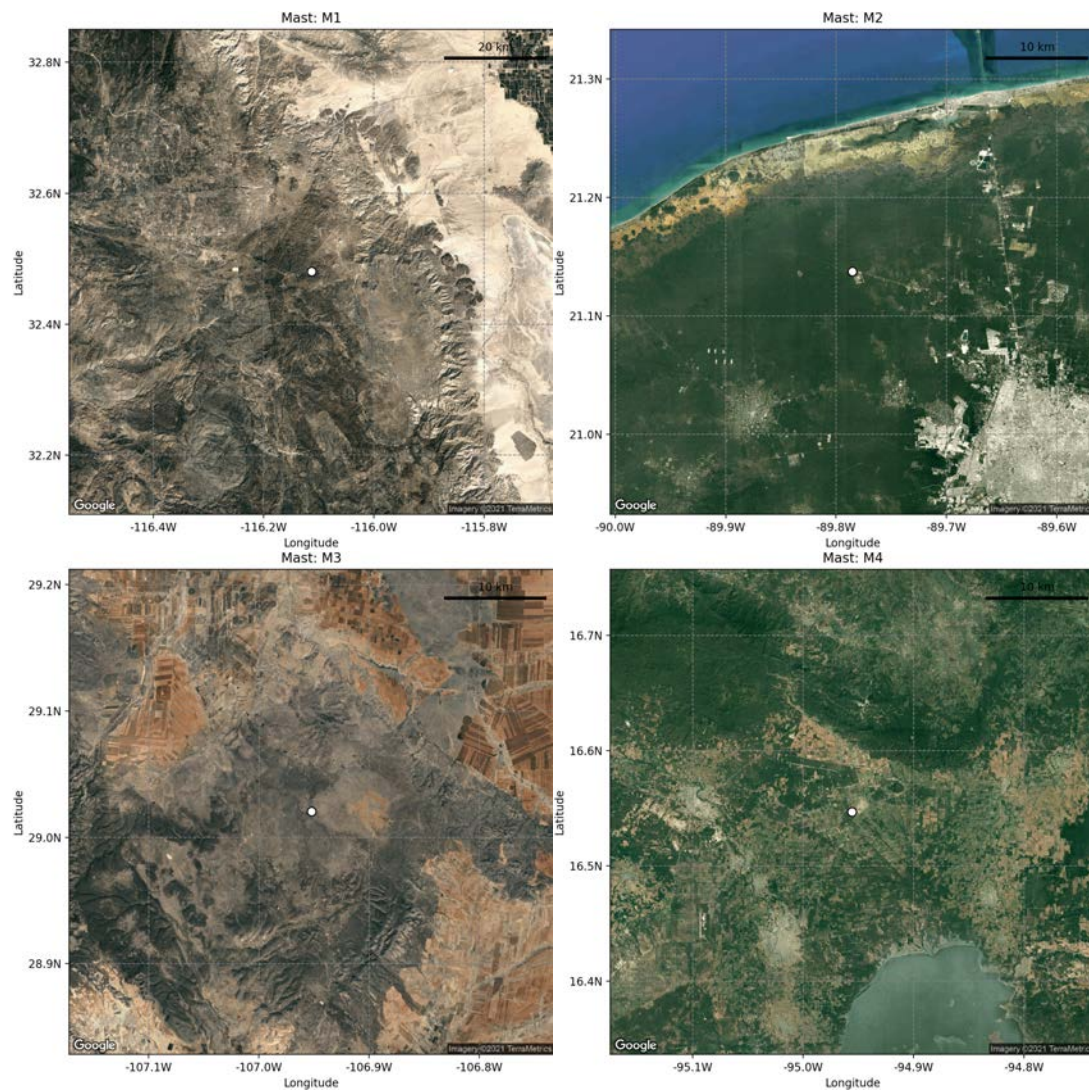


**Figure B.1** – Satellite figures obtained from Google Earth with the masts position indicated by a white dot. Top left: M1, top right: M2, bottom left: M3, bottom right: M4.

## APPENDIX B. GOOGLE EARTH IMAGES AT EACH SITE

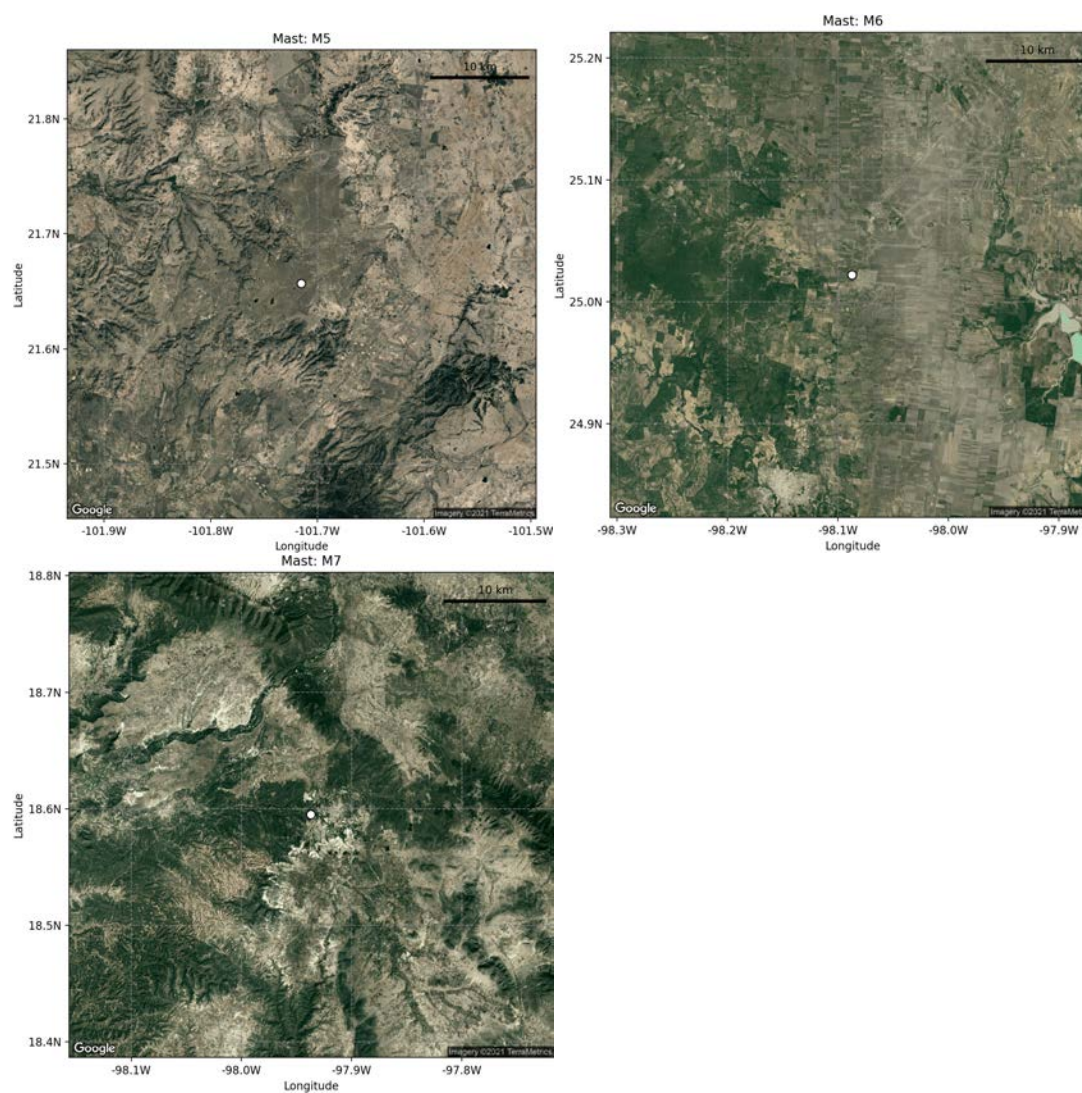


**Figure B.2** – Satellite figures obtained from Google Earth with the masts position indicated by a white dot. Top left: M5, top right: M6, bottom left: M7.

# Appendix C

## Lookup tables for roughness length

**Table C.1** – Surface roughness length as a function of land use class for the standard WRF (minimum and maximum) and the modified for the WAM WRF model simulations.

Min/Max stand roughness (m)	New roughness (m)	USGS land use class (class number)
0.05/0.15	0.10	dryland cropland and pasture (2)
0.02/0.10	0.10	irrigated cropland and pasture (3)
0.05/0.15	0.10	mixed dryland/irrigated cropland and pasture (4)
0.05/0.14	0.20	cropland/grassland mosaic (5)
0.10/0.12	0.10	grassland (7)
0.01/0.05	0.12	shrubland (8)
0.01/0.06	0.12	mixed shrubland/grassland (9)
0.50/0.50	0.90	deciduous broadleaf forest (11)
0.50/0.50	0.90	deciduous needleleaf forest (12)
0.50/0.50	0.90	evergreen broadleaf forest (13)
0.50/0.50	0.90	evergreen needleleaf forest (14)
0.20/0.50	0.50	mixed forest (15)
0.20/0.20	0.001	herbaceous wetland (new tidal zone) (17)

## APPENDIX C. LOOKUP TABLES FOR ROUGHNESS LENGTH

**Table C.2** – The roughness length that was assigned to each land cover class from the Globcover/ESA-CCI land cover database.

Code	DTU	EMD	WRF <sub>low</sub>	WRF <sub>high</sub>	desc
0	0.0001	0.0001	0.0001	0.0001	No data
10	0.1	0.1	0.05	0.1	Cropland, rainfed
11	0.1	0.1	0.05	0.1	Cropland rainfed, Herbaceous cover
12	0.2	0.2	0.3	0.5	Cropland rainfed, Tree or shrub cover
20	0.05	0.07	0.05	0.1	Cropland, irrigated or post-flooding
30	0.2	0.07	0.2	0.2	Mosaic cropland (>50%) / natural vegetation (t...
40	0.3	0.5	0.2	0.2	Mosaic natural vegetation (tree, shrub, herbac...
50	1.5	0.4	0.6	0.9	Tree cover, broadleaved, evergreen, closed to ...
60	1	0.4	0.6	0.9	Tree cover, broadleaved, deciduous, closed to ...
61	1	0.4	0.6	0.9	Tree cover, broadleaved, deciduous, closed (>40%)
62	0.8	0.4	0.6	0.9	Tree cover, broadleaved, deciduous, open (15–40%)
70	1.5	0.5	0.6	0.9	Tree cover, needleleaved, evergreen, closed to...
71	1.5	0.5	0.6	0.9	Tree cover, needleleaved, evergreen, closed (...)
72	1.5	0.5	0.6	0.9	Tree cover, needleleaved, evergreen, open (15–...
80	1.2	0.5	0.6	0.9	Tree cover, needleleaved, deciduous, closed to...
81	1.2	0.5	0.6	0.9	Tree cover, needleleaved, deciduous, closed (>...
82	1.2	0.5	0.6	0.9	Tree cover, needleleaved, deciduous, open (15–...
90	1.5	0.4	0.3	0.5	Tree cover, mixed leaf type (broadleaved and n...
100	0.2	0.4	0.05	0.12	Mosaic tree and shrub (>50%) / herbaceous cove...
110	0.1	0.07	0.05	0.12	Mosaic herbaceous cover (>50%) / tree and shru...
120	0.1	0.07	0.03	0.12	Shrubland
121	0.2	0.07	0.03	0.12	Shrubland evergreen
122	0.2	0.07	0.03	0.12	Shrubland deciduous
130	0.03	0.07	0.05	0.1	Grassland
140	0.01	0.05	0.05	0.05	Lichens and mosses
150	0.05	0.07	0.01	0.01	Sparse vegetation (tree, shrub, herbaceous cov...
151	0.05	0.07	0.01	0.01	Sparse tree (<15%)
152	0.05	0.07	0.01	0.01	Sparse shrub (<15%)
153	0.05	0.07	0.01	0.01	Sparse herbaceous cover (<15%)
160	0.8	0.1	0.4	0.4	Tree cover, flooded, fresh or brakish water
170	0.6	0.1	0.4	0.4	Tree cover, flooded, saline water
180	0.1	0.4	0.001	0.001	Shrub or herbaceous cover, flooded, fresh/sali...
190	1	0.4	0.5	0.5	Urban areas
200	0.005	0.02	0.01	0.01	Bare areas
201	0.005	0.02	0.01	0.01	Consolidated bare areas
202	0.005	0.02	0.01	0.01	Unconsolidated bare areas
210	0.0001	0.0001	0.0001	0.0001	Water bodies
220	0.003	0.001	0.001	0.001	Permanent snow and ice

DTU Wind Energy is a department of the Technical University of Denmark with a unique integration of research, education, innovation and public/private sector consulting in the field of wind energy. Our activities develop new opportunities and technology for the global and Danish exploitation of wind energy. Research focuses on key technical-scientific fields, which are central for the development, innovation and use of wind energy and provides the basis for advanced education at the university.

We have more than 250 staff members of which approximately 45 are PhD students. Research is conducted within three divisions: Wind Energy Materials & Components, Wind Turbine Design and Wind Energy Systems.

---

**Technical University of Denmark**

Department of Wind Energy  
Frederiksborgvej 399  
Building 118  
4000 Roskilde  
Denmark  
Telephone 46 77 50 85

[info@vindenergi.dtu.dk](mailto:info@vindenergi.dtu.dk)  
[www.vindenergi.dtu.dk](http://www.vindenergi.dtu.dk)